NASA CONTRACTOR REPORT

NASA CR-1219

EXPERIMENTAL INVESTIGATION IN AN ANNULAR CASCADE SECTOR OF HIGHLY LOADED TURBINE STATOR BLADING

Volume I. Analysis and Design

by James L. Bettner

Prepared by
GENERAL MOTORS
Indianapolis, Ind.
for Lewis Research Center

NATIONAL AERONAUTICS AND SPACE ADMINISTRATION • WASHINGTON, D. C. • DECEMBER 1968

NASA CR-1219

EXPERIMENTAL INVESTIGATION IN AN ANNULAR CASCADE SECTOR OF HIGHLY LOADED TURBINE STATOR BLADING

Volume I. Analysis and Design

By James L. Bettner

Prepared under Contract No. NAS 3-9404 by
GENERAL MOTORS
Indianapolis, Ind.

for Lewis Research Center

NATIONAL AERONAUTICS AND SPACE ADMINISTRATION

For sale by the Clearinghouse for Federal Scientific and Technical Information
Springfield, Virginia 22151 – CFSTI price $3.00

FOREWORD

The research described herein, which was conducted by the Allison Division of General Motors, was performed under NASA Contract NAS 3-9404. The work was done under the technical management of Mr. Edward L. Warren and Mr. Stanley M. Nosek, Airbreathing Engines Division and Fluid System Components Division, respectively, NASA-Lewis Research Center. The report was originally issued as Allison EDR 5315, July 1968.

ABSTRACT

An analytical and experimental program was initiated to investigate the application of boundary layer control concepts to highly loaded turbine stator blades in an annular cascade. A plain blade was designed which forms the performance base line for the program. Four boundary layer control concepts were investigated—vortex generators, tangential jet blowing, tandem airfoils, and jet flap. The stator blades were designed to a suction surface diffusion factor of 0.4.

TABLE OF CONTENTS

LIST OF TABLES

LIST OF ILLUSTRATIONS

EXPERIMENTAL INVESTIGATION IN AN ANNULAR CASCADE SECTOR OF HIGHLY LOADED TURBINE STATOR BLADING

by J. L. Bettner
Allison Division of General Motors

SUMMARY

This report presents the design and analysis of a six-blade annular cascade of highly loaded turbine stator blades incorporating boundary layer control concepts. The design and analysis of a plain stator blade is also presented. The plain blade design forms the program base line of performance against which the blades with boundary layer control were evaluated. The stator blades with boundary layer control (1) should not experience flow separation and (2) should function at the highly loaded level with improved performance over the plain blade. The boundary layer control concepts being investigated are vortex generators, tangential jet blowing, tandem airfoils, and the jet flap. The mechanical design, stress analysis, and instrumentation of the blade configurations and test rig are also included.

INTRODUCTION

Increasing interest in developing lightweight, highly loaded gas turbine engines confronts the designer with the problem of maintaining a high level of engine performance. To maintain a high level of engine performance flow separation from the blading surfaces must be prevented. When flow separation is experienced in a blade passage, there is a loss in available kinetic energy, mixing losses are increased, and the desired change in tangential momentum of the gas is not attained. The use of boundary layer control devices is one method of preventing flow separation and applies to both rotor and stator blading. The purpose of this investigation, therefore, is to examine four concepts of boundary layer control and determine their effects on highly loaded turbine stator blading. The four concepts being investigated are:

- Vortex generators
- Tangential jet blowing
- Jet flap blowing
- Tandem airfoils

A plain stator blade with high suction surface diffusion is being used as performance level base line for the program. Two different vortex generators were added to the plain blade suction surface and tested. Tangential jet blowing of secondary air was accomplished by using a blade shape identical to the plain blade except for modifications of the suction surface to accommodate the injection slot. Two axial positions of the tangential injection slot were investigated. For each slot position, three different slot heights covering the blade span were tested. The tandem airfoil and jet-flapped blade require entirely different airfoil shapes. Three different jet widths were tested at a constant jet efflux angle. In all configurations, the blades are designed to the same aerodynamic requirements.

This report covers the analysis and design phase of the overall program. This includes aerodynamic design of the plain stator blade, the analysis and design of four boundary layer control devices, the instrumentation plan, and the mechanical design and stress analysis of each blade configuration and the cascade rig. The aerodynamic performance of the plain and both vortex blade configurations is presented in Volume 2. The aerodynamic performance of the tandem, jet-flapped, and tangential jet blades is presented in Volumes 3, 4, and 5, respectively.

SYMBOLS

A	area, $in.^2$
Cv	velocity coefficient
Cj	jet momentum coefficient defined as ratio of jet to free stream momentum at point of jet injection
C_s	blade surface length
C	actual chord, in.
C_x	axial chord, in.
D	spacing or pitch between sets of vortex generators, in.
DS	region of gas turning from throat to trailing edge
Ds	suction surface diffusion parameter, $1 - \frac{\left(\frac{W}{W_{cr}}\right)_2}{\left(\frac{W}{W_{cr}}\right)_{max}}$
d	spacing or pitch between vortex generators making up one set, in.
F	Force
Fx	axial component of aerodynamic force on blade, lb
Fy	tangential component of aerodynamic force on blade, lb
g	acceleration due to gravity, ft/sec^2
H_i	boundary layer incompressible form factor defined as $\bar{\delta}_i/\theta_i$
h	vortex generator or plow height, in.
hb	injection slot height, in.
C_f	flow coefficient
ℓ	blade height, in.
M	Mach number or jet momentum, $lb_m/in.$
M_R	momentum ratio
$\dot{m}$	mass flow rate, lb/sec
no	length of potential line, in.
o	blade throat dimension, in.
P	pressure, psia
Rc	radius of curvature, in.
R	gas constant, $ft\text{-}lb/lb_m\text{-}°R$
r	radius, in.
S	surface length, in.

s	blade spacing or pitch, in.
T	temperature, °R
t	maximum thickness of blade or vane, in.
te	trailing edge radius, in.
tl	leading edge radius, in.
u	jet velocity, ft/sec
W	gas velocity, ft/sec
X	axial coordinate, in.
y	transverse jet stream coordinate normal to blade surface, in.
Y	tangential coordinate, in.
β	gas angle measured from tangential, degrees
γ	ratio of specific heats
Δ	incremental change of a variable
δ	boundary layer displacement thickness, in.
$\overline{\delta}$	boundary layer thickness, in.
δ_0	ratio of inlet air total pressure to standard sea level conditions
ζ	slot angle relative to engine centerline, degrees
Θ	jet deflection, degrees
Θ_{cr}	squared ratio of critical velocity at turbine inlet to critical velocity at standard sea level temperature
θ	boundary layer momentum thickness, in.
ρ	density of gas, lb/ft^3
σ	blade solidity, $\sigma = C_x/s$
τ	jet efflux angle, degrees
ψ	gas angle measured from axial, degrees

Subscripts

0	station at stator inlet
1	station at throat of stator passage
2	station at outlet of stator just upstream of trailing edge
3	station immediately downstream of trailing edge
4	station 2 in. (measured axially) downstream of trailing edge
a	actual
cr	conditions at Mach number of unity
f	force
h	hub radius

i	inside of blade cavity, incompressible
j	jet
m	mean radius and/or midchannel; mass
max	maximum
p	primary
pte	primary airfoil trailing edge
s	secondary, location of incipient separation
ss	suction surface
st	static condition
ste	secondary airfoil trailing edge
T	stagnation or total conditions
t	tip radius
te	surface distance from slot location to blade trailing edge
u	tangential component
VG	vortex generator
x	axial
Y	along radial potential line
wo/j	without jet-flap
w/j	with jet-flap

Superscripts

	ideal or isentropic condition

STATOR AERODYNAMIC DESIGN

OVERALL DESIGN SPECIFICATIONS

The objective of the design phase of the program was to design a series of highly loaded turbine stator blades that, with the incorporation of boundary layer control devices, has a high level of performance.

An annular cascade sector of six turbine stator blades was designed. The five passages of the cascade were subtended by an overall included angle of 27.631°. The blade tip diameter was 30 in. and the hub-tip radius ratio was constant at 0.7. The design point characteristics were as follows:

- Equivalent weight flow per passage, $\frac{\dot{m}_p\sqrt{\theta_{cr}}}{\delta_0}$: 1.05 lb/sec
- Equivalent change in tangential velocity: $\Delta W_u/\sqrt{\theta_{cr}}$
  - Hub: 1247.87 ft/sec
  - Mean: 1027.65 ft/sec
  - Tip: 873.71 ft/sec
- Suction surface diffusion factor, Ds: 0.4

PLAIN BLADE

The plain blade was designed to establish a base line of performance for evaluation of subsequent blade configurations; it was designed to experience flow separation. It was anticipated that the blade configurations incorporating boundary layer control devices would demonstrate marked performance improvements over the plain blade design.

Mechanical and Aerodynamic Design

The blade design procedure was similar to that described in reference 1 except that some of the hand constructions were analytically performed on the IBM 7094 computer. Station nomenclature and a flow path schematic are shown in Figure 1. It was assumed that a total pressure drop of 1% from the inlet to the blade passage throat and 3% from the throat to the trailing edge would realistically describe the stator in the test rig environment. Free vortex flow velocity diagrams, immediately downstream of the blade row were constructed using the required change in tangential velocity and the assumed 4% drop in total pressure across the blade row. These diagrams were calculated using Allison computer program G64 (which is described in Appendix A) and are shown as station 4 in Figure 2. Geometry of the blade throat region for a straight back blade was calulated with Allison computer

program D50 (which is discussed in Appendix B). This was accomplished by using the previously mentioned total pressure distribution through the blade row and consideration of blockage effects. Throat region velocity diagrams for the straight back blade are shown as stations 1 and 2 in Figure 2. Stations 1 and 2 are identical for a straight back blade since there is no further turning of the gas downstream of the throat.

In the interest of achieving a heavily loaded plain blade, particularly in region downstream of the throat, 13 degrees of downstream gas turning were incorporated in the plain blade design. Throat gas angles, with the inclusion of DS turning, are evaluated by the relation

$$\psi_1)_{\text{W/DS turning design}} = \psi_1)_{\text{straight back blade}} - \frac{\text{DS turning}}{2}$$

and are listed in Table I for the plain blade.

From the definition of the suction surface diffusion parameter, i.e.,

$$Ds = 1 - \frac{\left(\frac{W}{W_{cr}}\right)_2}{\left(\frac{W}{W_{cr}}\right)_{max}}$$

the maximum critical velocity ratio, $\left(\frac{W}{W_{cr}}\right)_{max}$, for Ds = 0.4, was calculated using $\left(\frac{W}{W_{cr}}\right)_2$ from Figure 2 and found to be 1.35, 1.189, and 1.082 for the hub, mean, and tip blade sections, respectively.

A compressible version of reference 2 provided design criteria to determine blade solidity in terms of a blade lift coefficient. Several preliminary designs were evaluated to investigate the effects of blade solidity and surface contour on blade loading distribution. The final design resulted in a blade that was reasonably heavily loaded, had a relatively low level of solidity, and yet was physically large enough to be adequately fitted with surface static pressure taps. Complete geometrical and aerodynamic design results for the plain blade are given in Table I.

Since the tangential jet blowing blades were developed from the plain blade profile, it was necessary to select a blade stacking axis location that would be satisfactory for both the plain and tangential jet blades. A stacking axis was selected for the plain blade that would result in the tangential slot being a straight line (hence, a straight jet slot machining tool) with the slot lip being of nearly uniform thickness.

Free-vortex flow in the blade passages is generated by contoured inlet guide walls leading up to the blade row. Stacking the plain and tangential jet blades identically permits these two blade configurations to use the same set of inlet guide walls.

Since experimental wake surveys were to be conducted, it was necessary to keep the trailing edge of the blade in a plane normal to the pseudo-axis of rotation. An elevation view of the plain blade is shown in Figure 3.

Appendix C describes the quasi three-dimensional stream filament calculation procedure of Allison computer program I87. This calculation procedure was employed to analyze the blade suction and pressure surface velocity distributions. The critical velocity ratio distributions for the hub, mean, and tip sections of the plain blade are shown in Figure 4, and the corresponding suction surface equivalent static pressure distribution is shown in Figure 5. The hub, mean, and tip blade contours are shown in Figure 6. The section coordinates are listed in Table II. Figure 7 illustrates the correspondence between axial and blade surface location.

Boundary Layer Analysis

The effect of the free stream static pressure distribution on the behavior of the blade surface turbulent boundary layer was investigated by using the calculation technique of Truckenbrodt (reference 3). This calculation procedure is discussed in Appendix D. Detailed information on the plain blade boundary layer behvaior was required in the design of subsequent blade configurations which incorporated boundary layer control devices. The axial variation of the computed boundary layer thickness, $\overline{\delta}$, and the incompressible boundary layer shape factor, H_i, are shown in Figures 8 and 9. Incipient flow separation was assumed to occur when H_i exceeded a value of 1.8. Figure 9 shows that separation occurs at axial distances of 0.595, 0.675, and 0.760 in. for the hub, mean, and tip sections, respectively. The calculated hub, mean, and tip momentum thicknesses, θ_s, at incipient separation were 0.00122, 0.00165, and 0.00197 in. These momentum thicknesses correspond to boundary layer thicknesses at separation of 0.010, 0.0125, and 0.0145 in. for the hub, mean, and tip sections, respectively.

BOUNDARY LAYER CONTROL DEVICES

The compressible, turbulent boundary layer analysis on the plain blade indicated that the flow would separate from the suction surface. Four additional stator blades were designed incorporating various concepts of boundary layer control to prevent this flow separation. The concepts investigated were vortex generators, tangential jet blowing, tandem airfoils, and jet flap. Two kinds of vortex generators and two tangential jet locations were investigated.

VORTEX GENERATORS

The existence of a retarding shear stress and/or an increasing pressure in the direction of flow brings about the phenomena of boundary layer thickening and possible subsequent flow separation. Thus, if the flow is to remain attached to a boundary, then the boundary layer must be energized by some external means. The objective of the present investigation is to use a mixing process as the mechanism of boundary layer reenergization.

The potential of the mixing process can be demonstrated by considering the location of separation of both a laminar and turbulent boundary layer in identical adverse pressure gradients. The laminar boundary layer will always separate before the turbulent boundary layer. It is the natural mixing process of the turbulent boundary layer that brings higher energy flow near the bounding surface; this allows the turbulent flow to proceed further into the region of rising pressure than could a similar laminar boundary layer. It is the purpose of the vortex generator blade configurations to augment the natural turbulent mixing process by using vortex generating devices in the flow field. The vortices shed from these devices will promote mixing of the high energy free stream flow with the retarded and low energy boundary layer flow.

Two types of vortex generators were selected for investigation—the two-dimensional co-rotating vane and the three-dimensional counter-rotating triangular plow. These devices are shown in Figure 10. Of the several types and arrangements of vortex generators that might have been chosen for this application, the ones selected were chosen on the basis of their designs being well documented and the availability of performance data. The selection of both two- and three-dimensional vortex generators was prompted by the mechanical scale of the application. The two-dimensional vane is simple to make and finds application in the prevention of shock-induced flow separation in regions of high free stream Mach number. In view of the small size that the generator must assume for the present application, it could degenerate from a two-dimensional thin vane to a three-dimensional rectangular block. Therefore, the triangular plow was chosen since it seemed advisable to also investigate a truly three-dimensional vortex generator. Both vortex generator configurations will be machined from a brass strip which will be laid in a shallow groove machined on the plain blade suction surface.

Two-Dimensional Co-Rotating Vane Vortex Generator

Lachmann (reference 4) has summarized a portion of the work on boundary layer control techniques performed at the National Physical Laboratory (NPL). In that work several modes of boundary layer control (including vortex generators) were investigated on one-half of a symmetrical airfoil with thickness-to-chord (t/C) ratios of 12 and 16%. Making the assumption that the suction surface length approximates the chord of a symmetrical airfoil results in t/C ratios of 17.35, 16.0, and 15.3% for the hub, mean, and tip sections, respectively, for the plain blade. Placing the generators at 30% of the surface length (as was done in the NPL investigations) results in the conditions given in Table III. A vane height of 0.015 in. (approximately 1% of the axial chord) was selected for this application. Ideally the generator height should penetrate slightly through the boundary layer. This gives the generator sufficient height to effect the necessary mixing while at the same time keeps the viscous drag penalty to a minimum. It can be seen from Figure 8 that if the vanes were positioned at 30% of the surface length, then the vane height should be about 0.010 in. The minimum vane thickness that can be tolerated from a mechanical viewpoint is 0.005 in. Thus, if the vane height were 0.010 in., the vane would degenerate from a two-dimensional vane to a three-dimensional block with a height equal to twice its width. Therefore, for the vane to be a two-dimensional body, it was necessary to select a vane height that was larger than the boundary layer thickness. The vane height of 0.015 in. was selected as being a satisfactory compromise between the mechanical and aerodynamic constraints of the application.

Schubauer and Spangenberg (reference 5) have investigated the effects of delaying separation by placing various kinds of vortex generators various distances from the observed point of uncontrolled separation. They also examined the effects of the shape of the pressure profile on preventing separation. These results are shown in Figure 11 and listed in Table IV. For the generators investigated, Table IV indicates that the ratio of distance to the point of separation to vane height, X/h, should be in the range of 3 to 15 in. to be the most effective in delaying separation. As given in Table III—i.e., generators placed at 0.300 C_s—it can be seen that for h = 0.015 in., X/h = 9.72, 8.65, and 10.86 for the hub, mean, and tip sections, respectively. These values of the distance parameter are probably large enough to ensure mixing; however, it is important not to locate the vortex generators on the surface where the free stream Mach number indicates that shock waves might be formed on the generator. Table III indicates a Mach number level at 0.30 C_s in excess of 1.0—i.e., shock waves with subsequent shock losses could be present on the generators at this location. To circumvent a potential shock loss problem, a hub, mean, and tip axial distance of 0.22 in. was selected for the location of the co-rotating vortex generators. Table V depicts the parameters describing this location of the vortex generators. The co-rotating vortex generators are shown in their respective hub, mean, and tip positions in Figures 12 and 13.

Three-Dimensional Counter-rotating Triangular Plow Vortex Generator

The triangular plow generator configuration is of rugged construction and should be readily adaptable to high temperature, corrosive or centrifugal field applications. Because the plow is truly a three-dimensional body, it avoids the performance variation of a two-dimensional body degenerating to a three-dimensional body.

Examination of the Schlieren photographs in reference 4 indicates that the co-rotating generator may have better performance than the counter-rotating generator at transonic and higher Mach numbers. Also, the results of reference 5 and Figure 11 show that at lower Mach numbers, the performance of the triangular plow is comparable to that of the co-rotating vane.

Of the three plows—E1, E2, and E3—discussed in reference 5, it can be shown that plow E1 has the greatest influence on reenergizing the boundary layer at the least expense. It is felt that this was because plows E2 and E3 were spaced much too close together. If counter-rotating vortex generators do not have sufficient spacing between them, the shed vortices damp one another out before they can significantly reenergize the boundary layer. If D is the pitch of a row of triangular plows and h is the plow height, plows E1, E2, and E3 had values of the parameter D/h of 8, 4 and 2, respectively.

It is recommended that sufficient plow spacing requires at least a D/h value of 8. The dimensions for the plow recommended for the present application are shown in Figure 14.

The considerations of required vortex mixing length, shock losses, etc, apply to the triangular plow in the same manner as they did to the co-rotating vane. Hence, the three-dimensional triangular plow generators were placed at the same axial position on the blade suction surface as the co-rotating two-dimensional vanes—$X_{VG} = 0.22$ in.

A generator height of 0.020 in. was selected for the plow. Reference 5 indicates that the height of the plow should be somewhat larger than that for a vane for comparable range and strength. At $X_{VG} = 0.22$ in., this height gives h/δ values of 8.86, 4.0, and 4.0, respectively, for the hub, mean, and tip sections. The resulting design parameters are listed in Table VI. The triangular plow generators are shown on the blade surface in Figures 15 and 16.

TANGENTIAL JET BLOWING BLADES

The cascade plain blade was modified to incorporate a tangential blowing jet to energize the boundary layer and thereby prevent flow separation.

Fluid flow parameters were calculated for three jet slot heights and two slot locations on the blade suction surface using isentropic flow equations. The choice of slot heights and locations was based largely on the results of experimental studies.

The equations used in determining the fluid flow parameters for the tangential jet were programmed for the IBM 1130 computer so that a number of variables could be investigated. Curves were constructed from these equations for the stator hub, mean, and tip sections for the two slot locations. The boundary layer data calculated for the plain blade configuration were used in determining the flow requirements of the tangential jet. For a particular value of boundary layer momentum thickness, θ, and free stream Mach number, there exists various combinations of jet slot heights and jet supply core pressures. These parameters will yield various jet mass flows and velocities and, if injected into the proper blade surface location, will prevent flow separation. Tables VII through X give the slot parameters for the two slot locations. Three slot heights of 0.020, 0.030, and 0.040 in. were chosen as being most likely to provide the best match of jet core supply pressure and jet mass flow for the two locations. To arrive at a unique supply pressure for each slot, a jet excess momentum ratio of 2.5 was assigned to the stator mean section. Values of supply total pressure to main stream total pressure ratios ranged from 1.71 to 1.18 for all slot configurations. The jet to main stream velocity ratios ranged from 1.246 to 1.054. The percentage of jet mass flow rate to main stream flow rate ranged from 2.590 to 6.20%.

Several investigations have been made to determine methods for preventing flow separation by injection to reenergize the boundary layer. Peake reviews several investigations in reference 6; these investigations involved injecting a fluid tangentially into the boundary layer. Peake mentioned the results of transonic speed tests performed at the National Physical Laboratory which showed that injection into the separated region caused by a shock-induced adverse pressure gradient produced a large effect on separation with small quantities of air. Other investigators found favorable results by injecting air upstream of the point of incipient separation using different magnitudes of airflow rate to overcome various magnitudes of pressure gradients. Peak's conclusions, based on his experimental investigation are as follows.

- The optimum position for injection appears to be about six original boundry layer thicknesses upstream of the point of incipient separation.

- Boundary layer control can be maintained up to static pressure ratios, P_2/P_1, of 3.0 provided the jet excess momentum is nearly equal to the momentum deficiency of the original boundary layer. (P_2 is the static pressure measured at a location downstream of the point where P_1 is measured.)
- The total pressure in the wake from the original boundary layer must be greater than the local value of static pressure. The decrease in the jet peak total pressure must not be so severe that the new wall boundary layer is in danger of separating.
- The flow quantities closely satisfy the momentum balance equation for small adverse pressure gradients, i.e., the momentum deficiency in the unblown, separating wall boundary layer equals the momentum excess in the jet, i.e.,

$$\rho_{ss} W_{ss}^2 \theta_s = \rho_j u_j hb (u_j - W_{ss})$$

- The jet to mainstream velocity rations, u_j/W_{ss}, were between 1.1 and 1.2 for control.

Peake also stated the following conclusions of Stradford (reference 7) with regard to his work on boundary layer control over airfoil shapes. Two and one-half times the ideal quantity of jet excess momentum must be supplied to negotiate large adverse pressure gradients. By defining momentum ratio, M_R, as the excess momentum in the jet divided by the momentum deficiency in the mainstream boundary layer,

$$M_R = \frac{\rho_j u_j hb (u_j - W_{ss})}{\rho_{ss} W_{ss}^2 \theta_s}$$

Figure 17 shows a correlation of adverse static pressure ratio with core to main stream total pressure ratio required to negotiate the adverse pressure ratio as interpreted from Peake's data. (One injection slot was used in Peake's experiments.) Also shown are the magnitudes of adverse pressure ratio existing on the cascade plain blade. The curve indicates that a core to mainstream total pressure ratio of approximately 1.3 is required to negotiate the maximum adverse pressure ratio existing at the hub section.

McGahan's investigations, reference 8, disclosed several items of interest.

- Injection into or too close to the normal separation region will often cause midstream stagnation to occur with a subsequent loss of jet effectiveness.
- The jet energy required to reach a given separation velocity decreases as the slot size increases up to some optimum slot size which has not yet been established.

- The internal design of the slot is critical due to the formation of vortices which cause a more rapid decay of the jet velocity and enhance wall separation.

Based primarily on the conclusions of Peake, Stradford, and McGahan, the following design criteria were established for the tangential jet slot.

- The ratio u_j/W_{ss} should fall in the range from 1.1 to 1.2.
- The jet excess momentum ratio, M_R, should be approximately 2.5 to negotiate a large adverse pressure gradient with one injection slot.
- The optimum location of the slot is approximately six initial boundary layer thicknesses upstream of the point of incipient separation using Truckenbrodt's incompressible shape factor of 1.8.

Introduction

The previously stated design criteria, together with the working curves in Appendix E, were used in choosing slot dimensions and locations for the basic stator blade. This provided the design information for the investigation of boundary layer control by tangential fluid injection. The slot was fabricated using a straight, constant width elox tool. The three slot heights chosen for the investigation—0.020, 0.030, and 0.040 in. — represent the best from mechanical and aerodynamic considerations.

Two slot locations were investigated. One was chosen at the optimum location given by Peake; the other location was arbitrarily chosen between the optimum location and the blade passage throat. It was felt that the second location would provide more useful information if it were located a significant distance from the first slot. If separation occurs as calculated, the second slot will be injecting fluid into the separated region. Figures 4 through 9 show plots of the boundary layer and flow data for the plain stator blade. The data from these curves provided the basic information used in the tangential jet analysis.

First Slot Location

The first slot location, based on Peake's criteria of $6\,\bar{\delta}_s$ upstream of the point of incipient separation, was found to be:

	Hub	Mean	Tip
First slot location (axial coordinate measured from the leading edge)	0.540 in.	0.610 in.	0.690 in.

The hub, mean, and tip slot locations lie very nearly on a straight line.

Following the recommendations of Peake, a momentum ratio, M_R, of 2.5 was selected for the mean section. This excess momentum in conjunction with available total pressure ratios should provide the necessary boundary layer control all the way to the blade trailing edge with only one tangential slot. Table VII summarizes the design parameters selected for the first slot location. The momentum ratio varies slightly from the hub to the tip sections for the three slot heights. Also, the jet to main stream velocity ratios are in the region recommended by Peake. Table VIII gives the values of $\bar{\delta}_s$, θ_s, X, S, and W_{ss}/W_{cr} used in the calculation of the jet flow parameters. Figures 18, 19, and 20 are plots of the flow parameters (slot to main stream total pressure ratio and mass flow ratio) for the 0.020-, 0.030-, and 0.040-in. slots. Figure 21 shows the jet to main stream velocity ratio as a function of total pressure ratio for the hub, mean, and tip sections applicable to all slot heights. Working curves used in plotting Figures 18, 19, 20, and 21 are presented in Figures 77, 78, and 79.

Second Slot Location

The first slot was located near the hub, mean, and tip positions of maximum velocity. Therefore, at a position upstream of the first slot location, the flow on the suction surface will be accelerating in a favorable pressure gradient. If the second slot were located upstream of the first slot, a portion of the jet momentum would be extracted by the wall viscous forces in the region of decreasing pressure even before the jet proceeded to the beginning of the pressure rise. Just how much momentum would be extracted is difficult to assess and there appears to be very little experimental data available on the subject. It was felt, therefore, that the second slot should be located between the first slot and the blade throat. An axial distance of 0.90 in. from the leading edge was selected for the mean section slot location. This placed the first and second slots a significant distance apart. The mean section unseparated flow pressure gradient was calculated (using Figure 5) and was found to be $\frac{\Delta P_{st}/\delta_0}{\Delta S} = 1.07$ psi/in. By assuming that this unseparated pressure gradient is constant from hub to tip and using the data of Figures 5 and 7, the hub and tip section slot positions were located. The axial location of the second slot was found to be:

	Hub	Mean	Tip
Second slot location, axial X	0.795 in.	0.900 in.	1.010 in.

These points lie very nearly on a straight line.

Table IX summarizes the design parameters selected for the second slot location and Table X gives the values of θ_s, X, S, W_{ss}/W_{cr}, and

$\frac{\Delta P_{st}/\delta_0}{\Delta S}$ used in the calculation of the jet flow parameters. The value of θ_s used in the calculation was the value existing at the point of incipient separation since any value downstream of that point is incalculable. It was assumed, however, that the velocity distributions of Figure 4 were still valid. From the standpoint of interpretation of experimental results, it was felt advisable to keep the slot heights the same for the two slot locations. This would eliminate any effects of slot geometry when assessing the merits of one slot position against the other. Further, it was also recommended that the momentum ratio of 2.5 be chosen for the mean section, as was the case for the first slot position, even though the pressure gradient appears to be less severe. If the flow does not separate, then the pressure gradient for the second slot will be less than that for the first slot. However, if separation does occur, as Truckenbrodt's method predicts it will, then the degree of adverse pressure gradient or pressure recovery required for the second slot location could be nearly equivalent to that required for the first slot location. Thus, it is felt that M_R should remain at 2.5.

Figures 22, 23, 24, and 25 were obtained from the working curves of Figures 80, 81, and 82 and are plots of the flow parameters for the selected slot heights of 0.020, 0.030, and 0.040 in. An elevation view of the tangential jet blade profile is shown in Figure 26 which illustrates the relative axial positions of the two tangential jets.

Suction Surface Geometry Downstream of Slot

To maintain the desired main stream velocity distribution downstream of the slot, the suction surface of the blade was "thinned out" to accommodate the additional mass flow rate from the jet. The procedure for the surface contour adjustment was determined based on the transverse growth of the jet stream as it traveled from the injection slot to the trailing edge. An analysis was made by assuming that no mixing of the jet stream and the main stream would take place and that the jet would retain its jet identity for the entire distance to the trailing edge.

By using the continuity equation, together with a correlation of jet velocity decay given by McGahan (reference 8), the transverse jet growth was obtained as follows.

$$y = \frac{\dot{m}_s}{(\rho_j u_a)_{X/B}}$$

where

$$(u_a)_{X/B} = \frac{(u_a)_{X/B}}{u_a} \times \frac{u_a}{W_{ss}} \times \frac{W_{ss}}{W_{cr}} \times W_{cr}$$

$$(\rho_j)_{X/B} = \frac{\rho_{jX/B}}{\rho_j} \times \frac{\rho_j}{\rho_0} \times \rho_0$$

and $\frac{(u_a)_{X/B}}{u_a}$ was obtained from reference 8.

The results of these calculations for the two slot locations are given in Table XI.

Core Geometry

Figure 27 illustrates scaled sections showing the exterior and interior blade contours for the hub, mean, and tip for slot location 1. Figure 28 shows similar data for slot location 2.

The interior of the blade was fixed by mechanical and fabrication requirements. A wall thickness of 0.050 in. (nominal) and a slot lip thickness of 0.020 in. (nominal) were used in the design. Radial average velocity calculations were made for the core of each blade at the hub section; these data are given in Table XII.

The core radial velocities should be kept as low as possible to allow for the energy loss associated with turning a high velocity gas from a radial to a tangential direction. The hub section radial velocities for the two slot locations are high, but it is felt that this is merely indicative of the severe secondary flow requirements when attempting to prevent flow separation in a very low solidity, highly loaded blade.

JET-FLAPPED BLADE

A jet-flapped blade employs a high velocity jet stream which emanates from the blade trailing edge lower surface to yield the following aerodynamic improvements.

- The interaction and exchange of momentum between the jet and mainstream effect a deflection of the mainstream flow from its undisturbed position.
- The static pressure and velocity distributions in the boundary layer on the blade surface are altered to such a degree by the jet that flow separation may be prevented. Thus, a blade incorporating a jet flap design should provide greater work capacity than conventional airfoils.

The basic design criterion of the jet-flapped blade was that it exhibit the same entrance velocity triangles and maximum suction surface velocity

as the plain blade configuration. The downstream velocity triangles are different because of the addition of secondary flow. The jet stream is obtained through a constant width slot covering the entire radial span of the blade. The slot will be fed from a cavity within the blade which receives air from an external source.

The required gas turning or change in tangential momentum was determined by the plain blade configuration. Thus, the blade design was based on distributing the required turning between the blade and the jet. By relieving the blade of a portion of the turning, the blade can be designed such that it will satisfy the turning and diffusion requirements and still exhibit no flow separation. The detailed procedure used in the design is described in the following paragraphs.

Blade Chord Determination

Since the blade was unloaded by the presence of the jet, it was necessary to reduce the chord so that a local loading approximately equivalent to that for the plain blade would be maintained. A chord reduction of about 10% was considered to be sufficient. This reduction (maintaining a leading edge slope equal to that for the plain blade) resulted in the following chords:

	Hub	Mean	Tip
C_x	1.2285 in.	1.4555 in.	1.6835 in.

This reduction in chord produced a jet-flapped blade solidity that was less than that for the plain blade, but still maintained a blade that was physically large enough to be adequately instrumented. For the jet-flapped blade design of reference 1, a 13.6% reduction in chord was used in conjunction with a 10% reduction in blade work. Therefore, the 10% chord reduction for the present investigation precipitated a reduction in the change of tangential momentum across the blade of between 6 and 7% less than that for the plain blade.

Mean Section Map of Jet Flow Conditions

The set of equations given in Appendix F was used to generate the data in Figure 29 which shows jet momentum as a function of slot width and total-to-static pressure ratio across the slot. Lines of constant jet mass flow rate are also shown and are expressed as a percentage of main stream flow.

Selection of slot width was almost arbitrary since a certain jet momentum applies for a variety of pressure ratios and jet mass flow rates. However, for the subject design, a maximum permissible source pressure for the jet was fixed at twice the inlet total pressure as follows:

$$\frac{P_{T_i}}{\delta_0} = 29.4 \text{ psia}$$

For the specified flow conditions at the mean section downstream,

$$\frac{P_{st_j}}{\delta_0} = 10.4 \text{ psia}$$

Hence,

$$(P_{T_i}/P_{st_j})_m = 2.83$$

To prevent the secondary boundary flow from choking inside the blade passage, the width of the passage was made to be equal to or greater than the slot width. The trailing edge diameter and minimum wall thickness were chosen to be 0.100 in. and 0.030 in., respectively. This resulted in the maximum slot width (0.040 in.) that could be tolerated.

With reference to Figure 29, a ratio $P_{T_i}/P_{st_j} = 1.5$ was chosen to represent the lowest pressure ratio where the jet would be effective. The intersection of $\frac{P_{T_i}}{P_{st_j}} = 1.5$ and hb = 0.040 in. defined a jet momentum of 0.31 lb_f/in. and the upper bound of the region of operation. For considerations of experimentally evaluating the jet size, it was desirable to keep the jet momentum constant, i.e., M = 0.31 lb_f/in. The intersection of the line M = 0.31 and the maximum pressure ratio, $(P_{T_i}/P_{st_j})_m = 2.83$ established the lower bound of the region of operation. This established the smallest slot to be 0.0217 in. The optimum design was chosen between these two extreme bounds. The optimum slot design data are as follows:

- Slot A

$$P_{T_i}/P_{st_j} = 1.85$$

$$M = 0.31 \text{ lb}_f/\text{in.}$$

$\frac{\dot{m}_j}{\dot{m}_p} = 4.4\%$

hb = 0.031 in.

It was required to investigate two additional slot widths—one larger and one smaller than the one selected for the design condition and both with the same jet momentum. The values for these additional slots are as follows:

- Slot B

  hb = 0.0217 in.
  $P_{T_i}/P_{st_j} = 2.83$
  M = 0.31 lb_f/in.
  $\dot{m}_j/\dot{m}_p = 3.5\%$

- Slot C

  hb = 0.040 in.
  $P_{T_i}/P_{st_j} = 1.5$
  M = 0.31 lb_f/in.
  $\dot{m}_j/\dot{m}_p = 5.3\%$

Velocity Triangles

Figure 30 shows the blade nomenclature used in the blade analysis. The inlet velocity triangles were the same for all blade configurations and are shown in Figure 2.

The downstream velocity triangles for the jet-flapped blade with 4.4% secondary flow were obtained by solving the equations of continuity of mass flow considering the addition of mass flow caused by the jet stream. The downstream tangential component of velocity was held equal to that of the plain blade. The resulting downstream velocity triangles are shown in Figure 31. The effect of a variation of percent jet flow to mainstream flow on the downstream gas angle was found to be only slight as shown in Figure 32.

Jet Deflection Characteristics

The downstream angle of deflection, Θ, was obtained by first extrapolating the cascade turning angle results of Clark and Ordway (reference 9) to zero angle of attack. These results were plotted against the jet momentum

coefficient, C_j, and are shown as the lower curve on Figure 33. Secondly, the cascade results of Kruger, March, and Horlock (reference 10) showed that the downstream angle of deflection varied approximately linearly with jet efflux angle, τ. On this basis, and with the experimental results of Lachmann (reference 11) which provided the upper curve on Figure 33, an interpolation was made to provide deflection curves for τ = 30, 45, 60, and 75 degrees. The cascades from which the experimental data were taken (references 9, 10, and 11) had solidities, σ, of approximately unity. Therefore, the use of Figure 33 should be restricted to applications where σ is about unity.

Simultaneous Solution of Passage Throat and Downstream Conditions

The mean section velocity triangle of the throat midchannel shown in Figure 34 was partially determined by removing 6% of the total tangential velocity component required. This method of unloading the jet-flapped blade was based on the assumption that with the jet on, total turning will be distributed between the blade and the jet to obtain the downstream velocity triangles shown in Figure 31. The design problem was that of satisfying the throat, jet, and downstream aerodynamic conditions simultaneously. To satisfy these aerodynamic conditions simultaneously, the following two sets of equations must be satisfied:

- Set 1

$$\Theta_1 = \psi_4 - \psi_1$$

$$W_{m_1} = W_{um_1}/\sin\psi_1$$

$$C_j = \rho_j u_a^2 \overline{hb}/1/2\ \rho_1 W_{m_1}^2\ o$$

- Set 2

$\Theta_2 = f(C_j, \tau)$ (obtained from Figure 33)

For an assumed value of jet efflux angle, τ, and throat dimension, o, a unique solution exists ($\Theta_1 = \Theta_2$) for a particular value of ψ_1 such that the jet deflection characteristics described empirically by $\Theta_2 = f(C_j, \tau)$ in Figure 33 are satisfied. The simultaneous solutions of Θ_1 and Θ_2 are obtained as shown graphically in Figure 35. The solution provides the midchannel throat conditions for the mean section. The hub and tip section midchannel throat conditions are determined as follows.

1. Because of manufacturing limitations, the slot width must be cut at a constant angle with respect to blade length, ζ, measured from the tangential direction.

2. For the most effective interaction of jet and mainstream momentum, the angle of jet efflux at the tip section must be 90 degrees. When all of the conditions mentioned previously have been satisfied and the midchannel throat velocities determined, the continuity of mass and simple radial equilibrium are checked. If they are not satisfied, then new assumptions of τ and o are made. These calculations are repeated until continuity of mass and simple radial equilibrium are satisfied. The final results of the calculation procedure for the jet-flapped blade design are as follows:

- Mean section midchannel throat
  Angle of jet efflux, τ = 84.7°
  Throat dimension, o = 0.736 in.
  Jet momentum coefficient, C_j = 0.141
  Midchannel throat velocity, W_{m_1} = 779 ft/sec (from Figure 35)
  Deflection angle, Θ = 9.2°

  Then,
  $\Theta = \psi_4 - \psi_1$
  $\psi_1 = \psi_4 - \Theta$
  ψ_4 = 48.54° (Figure 31)
  ψ_1 = 48.54° - Θ = 39.34°
  $\zeta = [90 - \{(90 - \psi_1) + (90 - \tau)\}]$
  For τ = 84.7°, ψ_1 = 39.34°, and ζ = 34.04°

- Tip section midchannel throat
  Since ζ = 34.04° (constant radially) and $\tau = 90° - (\psi_1 - \zeta)$,
  $\psi_1 = \psi_4 - \Theta$
  ψ_4 = 43.89° (Figure 31)
  $\tau = 90° - (43.89° - \zeta) + \Theta$
  $\tau = 80.15° + \Theta$

  Simultaneous solution of the equation $\tau = 80.15° + \Theta$ with Figure 33 gives C_j = 0.128 for τ = 90° and Θ = 9.8°. The condition of τ = 90° at the tip section is satisfied. Construction of Figure 36 made it convenient to obtain values of C_j for certain values of W_{m_1} at the hub and tip sections during the iteration procedure. The throat dimension used for generating Figure 35 was obtained by assuming a radial distribution of throat dimension to blade spacing ratio equal to that of the plain blade as shown in Figure 37. From Figure 35,

  W_{m_1} = 735 ft/sec

- Hub section midchannel throat

  The calculation technique employed at the tip section was applied at the hub, i.e.,

  $\tau = 90° - (\psi_1 - \zeta)$

  $\psi_1 = \psi_4 - \Theta$

  $\psi_4 = 53.96°$ (Figure 31)

  $\tau = 90° - (53.96° - \Theta - \zeta)$

  Since $\zeta = 34.04°$

  $\tau = 70.08° + \Theta$

  The simultaneous solution of the equation $\tau = 70.08° + \Theta$ with Figure 33 yielded

  $C_j = 0.156$

  $\tau = 80.0°$

  $\Theta = 8.8°$

  Hence, $\psi_1 = \psi_4 - \Theta = 53.96° - 8.8° = 45.16°$.

  From Figure 36, $W_{m_1} = 852$ ft/sec.

- Now using the calculated hub, mean, and tip midchannel velocities and throat gas angles, the conditions of radial equilibrium and continuity were checked. These results are given in Table XIII. The error between the calculated and required quantities was less than 1%.

  Table XIV is a complete list of the final calculated quantities.

Development of Blade Sections

The development of blade surfaces consisted of spline-curve-fitting the hub, mean, and tip sections using (1) the throat dimensions and angles from Table XIV, (2) the required inlet gas angles, and (3) the curvatures estimated from the data of Hubbert and MacGregor (reference 12). The flow passages at the hub, mean, and tip sections within the confines of covered turning (from about the pressure surface tangency point to the throat) were divided into segments bounded by flow orthogonals. The flow within the bounded region was analyzed using the compressible, quasi three-dimensional computer program I87. The suction surface coordinates were obtained by solving

the curvature ordinary differential equation using a curvature distribution made up of polynomial expressions. The pressure surface curvatures were obtained using the second derivative of a least squares curve fit of the coordinates. An attempt was made to use an analytical surface for the pressure surface; however, it was not successful because of the combinations of curvatures and the orthogonal length required. Several blade surfaces were constructed before all of the design constraints were satisfied. The axial distribution of surface relative critical velocity ratio for the hub, mean, and tip sections is shown in Figure 38.

Boundary Layer Analysis Without Jet Flap

The boundary layer on the suction surface of the jet-flapped blade without the jet was analyzed using the compressible, turbulent boundary layer calculation from Truckenbrodt (reference 3). Figure 39 shows the axial variation of the incompressible turbulent boundary layer shape factor, H_i, on the suction surfaces of the hub, mean, and tip sections without the jet flap. Figure 39 shows that separation is incipient very near the throat for the hub and mean section. Although the tip section value of H_i has not attained the value of 1.8 at the throat, any extrapolation beyond the throat would indicate separation.

Static Pressure and Velocity Distributions With Jet Flap

The jet stream contours (described in Appendix G and shown in Figure 40) were added to the trailing edge of the pressure surface. It was coincidental that the hub, mean, and tip contours were nearly identical. The jet was given the thickness of the slot width (0.031 in.) and was extended beyond the blade trailing edge until it assumed the downstream gas angle. An analysis of the surface velocity distribution around the jet-flapped blade and the jet was performed using the relaxation solution of the Laplace equation which is incompressible and two dimensional. This analysis is discussed in Appendix H and was applied to the hub, mean, and tip sections of the jet-flapped blade with and without the jet for purposes of comparison. A similar analysis was performed on the plain blade so that the velocity and static pressure distributions determined would provide a basis for comparison with the jet-flapped blade. The suction surface "incompressible" critical velocity ratio distributions are shown for the hub, mean, and tip sections of the jet-flapped blade with and without the jet in Figures 41, 42, and 43, respectively.

Boundary Layer Analysis With Jet Flap

To analyze the compressible turbulent boundary layer on the jet-flapped blade with the jet, it was necessary to transform the incompressible velocity distributions to a pseudo-compressible velocity distribution. The compressible velocity calculation permitted analysis only to the blade throat. It was assumed that a reasonable extrapolation of the compressible velocity distribution without the jet could be made from the throat to the trailing edge. Since the incompressible

solution was available in this region, a ratio of the compressible to incompressible velocity distribution was taken at each axial distance along the suction surface and multiplied times the incompressible velocity distribution with the jet expressed as follows:

$$\left[\frac{W}{W_{cr}}(x)\right]_{\text{Comp w/j}} = \left[\frac{W}{W_{cr}}(x)\right]_{\text{Incomp w/j}} \left\{ \frac{\frac{W}{W_{cr}}(x)_{\text{Comp wo/j}}}{\frac{W}{W_{cr}}(x)_{\text{Incomp wo/j}}} \right\}$$

The result of this transformation appears as a pseudo-compressible velocity distribution for the hub, mean, and tip sections in Figures 44, 45, and 46, respectively.

The results of performing the boundary layer analysis on the jet-flapped blade with the jet are shown in Figure 47. It can be seen that the incompressible shape factor, H_i, reaches a maximum value of 1.73 at the hub section and then decreases, indicating that separation has been prevented by the effect of the jet on the suction surface velocity distribution. A similar situation exists at the mean and tip sections.

Results of Surface Static Pressure Distribution Analysis

The variation of surface static pressure with axial distance was calculated for the plain blade, the jet-flapped blade without the jet, and the jet-flapped blade with the jet. For the calculation, the incompressible, two-dimensional velocity distribution obtained from the boundary layer analysis without jet flap was used. These static pressure distributions are shown for the hub, mean, and tip sections in Figures 48 through 53. The change in tangential momentum of the gas passing through the blade row can be represented by the expression

$$\int_0^{C_x} \frac{P_{st}}{\delta_0}\, dx$$

for the region bounded by the suction and pressure surfaces. Theoretically, if the jet-flapped blade (with the jet on) was to do the same amount of turning or work on the gas as the plain blade, then this integral should have the same value for the two blades. Each of the curves of Figures 48 through 53 was graphically integrated and the results are given in Table XV.

Two methods were used to evaluate the effect of the jet on the tangential momentum change for each blade. The first method was based on comparing

the product of ΔW_{u_1} and A_3/A_2 for the jet-flapped blade with the assumption of no change in tangential momentum downstream from the throat. The second method was obtained by forming the product of ΔW_{u_4} for the jet-flapped blade and A_3/A_1. The results of the comparisons are given in Table XV as a percent difference between the adjusted ΔW_u values for the jet-flapped blade and the plain blade values. The agreement appears to be reasonably good considering that a two-dimensional, incompressible velocity analysis was used in determining the static pressure distributions.

Blade Interior Design

The interior design of the blade was fixed by structure considerations and the flow passage area near the jet discharge. A nominal wall thickness of 0.050 in. was maintained around most of the blade contour except in the region of the jet discharge where the wall thickness was tapered to a minimum of 0.030 in. The interior and exterior blade section contours are shown in Figure 54. Core areas were determined from Figure 54 and radial flow velocities at the hub section were calculated. A tabulation of these values is given in Table XVI. The velocities were compatible with previous designs and were considered acceptable.

Summary

- The maximum suction surface velocity requirements were satisfied.
- With the jet on, flow separation was prevented all the way to the trailing edge of the blade.
- The work capacity of the jet-flapped blade with the jet on was very nearly equal to that of the plain blade.
- The mechanical characteristics of the jet-flapped blade were satisfactory as far as structural integrity and secondary flow velocity were concerned.

Pertinent design data for the annular cascade jet-flapped blade configuration are given in Table XVII. Blade section coordinates are given in Table XVIII.

TANDEM AIRFOIL BLADE

The design philosophy of the tandem blade was to distribute the overall gas turning between two airfoils. Further, from the boundary layer analysis on the plain blade design, it was apparent that the static pressure rise from the axial position of maximum suction surface velocity to the blade trailing edge could not be negotiated without experiencing flow separation. From this it was concluded that the secondary airfoil could not satisfy Ds = 0.4 without having a region of separated flow. Therefore, the tandem blade was to be

designed such that the maximum suction surface velocity, equivalent to that of the plain blade, occurred on the primary airfoil suction surface. It was felt that this decision was in keeping with the context of having all blade configurations designed to the same loading level.

Figure 55 is a schematic drawing of a tandem blade configuration defining the geometric terms of the vane. The blade-to-blade aerodynamic analysis was performed independently in the four regions shown in Figure 55 using the quasi three-dimensional stream filament calculation procedure described in Appendix C. For an assumed primary and secondary airfoil arrangement and assumed flow split between the main and slot channels, the aerodynamic analysis was performed using the total mass flow in regions 1 and 4, whereas regions 2 and 3 were analyzed using only the slot flow in regions 2 and the total flow minus the slot flow in region 3.

It was required that the solidity of the tandem blade be less than that of the plain blade. This reduction in solidity was obtained by decreasing hub, mean, and tip sections by an amount equal to 10% of the plain blade hub section axial chord. The amount of downstream gas turning was increased from 13 degrees (which existed on the plain blade) to 15 degrees. This design change was to effect a more heavily loaded secondary blade by requiring it to do more of the necessary gas turning.

The velocity level at the secondary airfoil suction surface throat is a function of the total mass flow rate, midchannel gas angle, suction and pressure surface curvature, and the throat dimension. The suction surface curvature and velocity level, resulting from a downstream gas turning angle of 15 degrees, was very nearly the maximum that could be tolerated and still prevent flow separation all the way to the trailing edge. Thus, the secondary airfoil was defined from the throat to the trailing edge.

A study was performed to determine the location of the trailing edge of the primary airfoil with respect to the secondary airfoil. This study was to provide information about the maximum velocity level that could exist at the primary airfoil trailing edge. It turned out, however, that the velocity level that should exist at the primary airfoil trailing edge was very nearly independent of its location relative to the secondary blade. Figure 56 shows the simultaneous solution for the primary airfoil trailing edge suction and pressure surface critical velocity ratios as a function of circumferential position and flow split. In all cases the maximum critical velocity ratio that could exist at the primary airfoil trailing edge was approximately $W/W_{cr} \sim 0.70$ to 0.80.

Boundary layer behavior studies were made using the method of Truckenbrodt described in Appendix D for several tentative primary airfoils. These airfoil studies demonstrated that flow could not decelerate

from the primary airfoil location of maximum suction surface velocity level corresponding to Ds = 0.4 down to the level shown in Figure 56 which exists at the primary airfoil trailing edge without the flow experiencing separation. This circumstance necessitated relaxing the diffusion factor, Ds, value of 0.4. The tandem blade was designed so that the flow closely approached a separated condition on both the primary and secondary airfoils.

A tentative flow split and position for the primary airfoil trailing edge were selected and the primary airfoil pressure surface was constructed. The suction surface on the secondary blade was constructed so that it had low incidence on its leading edge and blended smoothly to the previously established suction surface at the throat. The velocity distribution and boundary layer characteristics were then calculated on the secondary airfoil suction surface. If the flow separated (i.e., $H_i \geq 1.8$), then new combinations of primary pressure surface and secondary suction surface were investigated. If it was determined that reasonable combinations of surfaces could not be found, then a new circumferential position of the primary airfoil trailing edge was assumed and the process repeated. This was continued until there were no flow separations on the secondary blade.

Once the secondary airfoil and the pressure surface of the primary airfoil were defined, preliminary primary blade suction surfaces were constructed to have zero incidence on their leading edges and were made tangent to the trailing edge circle. These surfaces were analyzed for velocity distribution and boundary layer behavior. The surfaces were altered until the boundary layer shape factor had a satisfactory distribution (i.e., H_i approached but did not exceed 1.8). An attempt was made to divide the required gas turning evenly between the two airfoils. This approach was abandoned, however, as it resulted in an unsatisfactory amount of incidence on the secondary blade and a very lightly loaded primary blade.

The tandem blade hub, mean, and tip velocity distributions are shown in Figures 57, 58, and 59, respectively. The primary and secondary blade boundary layer plots are shown in Figures 60 and 61. The design flow split was 26.4% in the slot channel and 73.6% in the main channel. Figures 60 and 61 show that theoretically the flow has approached but not attained a separated condition on either the primary or secondary suction surface.

The diffusion parameter level is significantly below the original value of Ds = 0.4. The diffusion parameters, based on their respective trailing edge velocity levels, are given in Table XIX. Hub, mean, and tip sections of the tandem blade are shown in Figure 62. Design data and tandem blade section coordinates are listed in Tables XX and XXI, respectively.

MECHANICAL DESIGN

CASCADE RIG

The arrangement of the test rig and plenum chamber and the assembly of the cascade test rig are shown in Figures 63 and 64, respectively. The plenum chamber section adapts the test rig to the test cell facility. The chamber contains pressure and temperature instrumentation and a series of flow straightening screens. A mahogany bell mouth is located in the plenum chamber and blends into a set of inlet flow guide walls. These guide walls are contoured to generate the proper free-vortex flow in a plane immediately upstream of the blade leading edge.

The cascade test rig is made of low carbon steel sections that stack together to form an annulus sector. Six brass blades, cantilevered from a common platform at their hub sections, form the blade cascade. The two center blades are instrumented with static pressure taps to define the flow conditions in the center flow passage of the cascade. Removal of upstream boundary layer build up on the upstream hub and tip walls is accomplished by pulling off the low energy boundary layer flow through a porous 2.00 × 0.014-in. strip of 316 SS. The strip is mounted upstream of and perpendicular to the blade row leading edge on both the hub and tip walls. Fabrication of the porous metal strips was accomplished by photo-etching 0.015-in. diameter holes on 0.031-in. centers through the 0.014-in. thick stainless sheet. Secondary air, which is supplied to the hollow blade configurations, is admitted through the 3-in. line connected to the chamber beneath the blade platform. An O-ring seal around the platform prevents leakage between the primary and secondary flows.

Static pressure taps are located on the plain blade extended midchannel lines on the hub and tip casing walls. These taps are 0.125 in. upstream and 0.125 and 2 in. downstream of the blade row. The proper distance relationship even though the blade axial chords vary from one configuration to the next, is maintained by using spacer plate sections with each configuration. One spacer plate is used with the plain and tangential jet blades since they have the same axial chord length. Another spacer plate, of thinner cross section, is used with the tandem and jet-flapped blade configurations.

The tip casing is slotted to permit radial and circumferential surveys of the gas conditions in planes immediately behind the blade row and 2 in. in the axial direction downstream of the blade row. The slot immediately behind the blade row is plugged and the tip wall contour is restored when surveys are conducted at the 2-in. axial station. The gas is guided out of the cascade by a set of contoured exit guide walls. These walls are designed to satisfy free-vortex flow constraints. The effects of these walls

on the plain blade performance was investigated during the experimental portion of the investigation.

BLADE STRESS ANALYSIS

The magnitude, direction, and location of the surface forces are obtained from the analytical static pressure distributions around the hub, mean, and tip airfoil sections. Similarly, surface forces are determined at 25% and 75% blade length sections from interpolated data. These results are presented in Table XXII. It is assumed that the tangential jet blades experience the same surface loading as the plain blade configuration.

The stress analysis of the blades assumes rig inlet conditions of 540°R temperature and 1.44-atmospheres pressure. The blade material is AMS-4610 brass. These rig conditions and the blade load data in Table XXII are used to find the maximum bending stress, first natural frequency, and blade tip deflection for all of the blades in cantilevered condition. Also, similar information is determined for the tandem blade with both the hub and tip ends fixed. These results are listed in Tables XXIII and XXIV. The stress analysis indicated that all but the tandem blade configuration are satisfactory in a cantilevered condition. The tandem blade was tested with both hub and tip sections fixed to the rig casing.

INSTRUMENTATION

The stator blade element performance instrumentation plan consists of the details of measuring the following:

Stator inlet	Stator exit
Total temperature	Total temperature
Total pressure	Total pressure
Static pressure—hub and tip	Static pressure—hub and tip
Gas flow angle	Gas flow angle

Overall

Primary airflow rate
Secondary airflow rate
Boundary layer bleed airflow rate

AIRFLOW MEASUREMENT

Primary Airflow

The primary airflow is measured by a 5-in. diameter Serial Number 2 Hamer orifice which is installed in the 16-in. diameter pipe immediately upstream of the test rig plenum chamber. The static pressure differential across and the absolute static pressure upstream of the orifice are indicated on vertical mercury manometers which can be read to 0.05 in. Gas temperature is measured by thermocouples which are located immediately downstream of the orifice and connected to a Brown indicating potentiometer. The Hamer orifice is calibrated to ASME standards.

Secondary and Boundary Layer Bleed Airflow

The secondary airflow is provided by the shop air facility and is measured by a 0.353-in. diameter thin plate, sharp edged orifice. This orifice is calibrated to ASME standards. Flow is measured by recording gas temperature, static pressure differential (in inches of water), and the upstream absolute static pressure (in inches of mercury).

The boundary layer bleed airflow is measured by a 3.019-in. thin plate, sharp edged orifice which is calibrated to ASME standards. The required vacuum is provided by a steam jet air ejector system. The amount of boundary layer bleed is determined by the establishment of a uniform total pressure profile along the elements of the total pressure rakes mounted at the extreme ends of the hub and tip sections of the cascade. The design of these rakes is shown in Figure 65.

STATOR INLET INSTRUMENTATION

The plenum chamber total pressure was measured by four 0.188-in. ID probes bent at right angles to the gas flow. The opening in each probe is chamfered to have a 20-degree capture cone. The probes were mounted at 90-degree increments around the plenum chamber. Three of the probes were connected to vertical mercury manometers. The fourth probe was connected to a 0- to 25-psi Schaevitz-Bytrex (0.1% accuracy) pressure transducer. The pressure transducer output was recorded by the Systems Engineering Laboratory (SEL) data acquisition system. Three iron-constantine thermocouples were used to record the plenum chamber total temperature.

A radial survey of total pressure and gas angle was performed in a radial-circumferential plane slightly upstream of the blade row. The prism probe was located approximately 0.75 in. upstream of the blade mean section on the mean section extended midchanel line. The probe stem is 0.25 in. in diameter except for the 1.5-in. stem segment above the pressure sensing ports. In the region of the sensing ports the stem is 0.125 in. in diameter. The pressure sensing ports are made of 0.030 × 0.003-in. wall tubing. The probe was inserted through the tip casing wall and located at various radial positions in the gas stream. The probe was yawed manually to locate the direction of the gas stream and to determine the magnitude of the total pressure. It was necessary that, when the probe is retracted from the gas stream, the tip wall contour be restored. This probe is shown in Figure 66.

Five 0.030-in. diameter static pressure taps are located in the hub and tip casing 0.125-in. upstream of the blade leading edge. The static pressures were recorded manually from mercury manometers.

BLADE SURFACE INSTRUMENTATION

The two center blades of the cascade for each configuration are instrumented with 50 static pressure taps. One blade is instrumented primarily on the suction surface while the other is instrumented primarily on the pressure surface. In this manner, the center flow passage flow conditions were defined. The blade instrumentation was accomplished by (1) laying 0.010-in. ID tube in grooves on the blade surface opposite that surface being instrumented and (2) restoring the grooved surface contour. For the hollow blade configurations, the two blade halves were parted and the instrumentation lines were laid in the blade wall. One of the instrumented plain blades is shown in Figure 67. The location of the static pressure taps for all of the blade configurations is illustrated in Figures 68 through 72. Tables XXV through XXIX list the axial coordinates of the static pressure taps. The two center blades of each hollow blade set contained total temperature instrumentation in the blade cavity at the mean section.

STATOR EXIT INSTRUMENTATION

Static pressure taps are located in the hub and tip casing at axial distances of 0.125 and 2 in. downstream of the blade trailing edge on the plain blade midchannel line.

A radial and circumferential total pressure survey was made in a plane approximately 0.030 in. downstream of the blade trailing edge using the bifurcated probe shown in Figure 73. The probe stem was 0.25 in. in diameter and necks down to 0.042 in. in the neighborhood of the pressure sensing element. The probe was mounted at a fixed angle in an L.C. Smith "saddle" type probe actuating mechanism. Surveys of total pressure were performed through 12 circumferential degrees at ten radial depths. The sweep rate of the traverse mechanism was 0.2 circumferential degree per second. The use of the two probe elements permitted data acquisition very near the hub and tip walls. Each probe element had an opening of 0.008 in. This small probe size permitted adequate definition of the blade wake boundary layer characteristics.

Radial and circumferential surveys of total pressure, total temperature, and gas flow angle were performed with the prism probe shown in Figure 74. The probe was mounted in the same saddle actuating mechanism as the bifurcated probe. The surveys were performed through approximately 26 circumferential degrees at ten radial depths. The circumferential sweep rate of the actuating mechanism was the same for this prism probe as it was for the bifurcated probe. The 0.25-in. diameter probe stem housed the three 0.028 OD × 0.003-in. wall tubing pressure sensing ports. A conventional iron-constantine thermocouple was mounted immediately below the pressure sensing ports. This survey was performed in a plane 2 in. downstream of the blade row.

The survey data from both the bifurcated and prism probes were obtained from a 0- to 25-psi Shaevitz-Bytrex pressure transducer and recorded on the Systems Engineering Laboratory system.

In addition to the aforementioned aerodynamic measurements, a flow visualization study of boundary layer separation was performed. A mixture of lamp black and mineral oil was applied to the trailing edge suction surface region, and photographs of the resulting separated flow regions were taken.

REFERENCES

1. Lueders, H. G.: Experimental Investigation of Advanced Concepts To Increase Turbine Blade Loading. I. Analysis and Design. NASA CR-735, 1967.

2. Zweifel, O.: Optimum Blade Pitch for Turbomachines with Special Reference to Blades of Great Curvature. The Engineering Digest, vol. 7, No. 11 (November 1946) pp. 568-570; continued, vol. 7, No. 12 (December 1946) pp. 601-603.

3. Truckenbrodt, E.: A Method of Quadrature for Calculation of Laminar and Turbulent Boundary Layer in Case of Plane and Rotationally Symmetric Flow. NACA TM 1379, 1955.

4. Lachmann, G. V.: Boundary Layer and Flow Control, Its Principles and Applications. vol. II, Part IV, Pergamon Press, 1961, pp. 1260-1332.

5. Schubauer, G. B.; and Spangenberg, W. G.: Forced Mixing in Boundary Layers. Journal of Fluid Mechanics, vol. 8. 1960, pp. 10-32.

6. Peake, D. J.: The Use of Air Injection to Prevent Separation of the Turbulent Boundary Layer in Supersonic Flow. N.G.T.E., Report R256, November 1963.

7. Stradford, B. S.: Boundary Layer Control by Injection from Aircraft Gas Turbine Engines. A.R.C. 16137, FM 1949, July 1953.

8. McGahan, W. A.: The Incompressible Turbulent Wall Jet in an Adverse Pressure Gradient. Ph.D. Thesis, Massachusetts Institute of Technology, September 1965.

9. Clark, E. L. and Ordway, D. E.: An Experimental Study of Jet-Flap Compressor Blades. Journal of the Aero/Space Sciences, November 1959, pp. 698-702.

10. Kruger, R. A.; Marsh, H.; and Horlock, J. H.: The Performance of a Cascade Fitted with Blown Flap. Aeronautical Research Council, C.P. No. 526, 1961.

11. Lachmann, G. V.: Boundary Layer and Flow Control. vol. 1, Part II, Pergamon Press, 1961, pp. 362.

12. Hubbert, M. C. and Mac Gregor, C.: Comparison Between Predicted and Observed Performance of Gas-Turbine Stator Blade Designed for Free-Vortex Flow. NACA-TM-1810, April 1949.

13. Culick, F. E. C. and Hill, J. A. F.: A Turbulent Analog of the Stewartson-Illingworth Transformation. Journal of Aeronautical Sciences, vol. 25, No. 4, April 1958, pp. 259-262.

14. Stewartson, K.: Correlated Compressible and Incompressible Boundary Layers. Proceedings of the Royal Society. Series A, vol. 200, No. A1060, December 1949, pp. 84-100.

15. Englert, G. W.: Estimation of Compressible Boundary Layer Growth Over Insulated Surfaces with Pressure Gradient. NACA-TM 4022, 1957.

16. Rubesin, M. W.; Maydew, R. C.; and Vargo, S. A.: An Analytical and Experimental Investigation of the Skin Friction of the Turbulent Boundary Layer on a Flat Plate at Supersonic Speeds. NACA-TM 2305, 1951.

17. Higgins, C. C. and Wainwright, T. W.: Dynamic Pressure and Thrust Characteristics of Cold Jets Discharging from Several Exhaust Nozzles Designed for VTOL Downwash Suppression. NASA TN D-2263, April 1964

18. Neprud, T. S.: Pneumatic Flow through Narrow Slots. Machine Design, 27 February 1964, p 163.

19. Spence, D. A.: The Two-Dimensional Jet Flap—An Exact Solution in Closed Form for Small C_j, and an Interpolation Formula Up to $C_j = 10$. Royal Aircraft Establishment Gt. Brit. Report No. Aero 2568, 1956.

APPENDIX A

DOWNSTREAM VELOCITY TRIANGLE CALCULATION PROCEDURE

The downstream velocity triangle requirements were calculated using Allison computer program G64. The calculation satisfies the required hub, mean, and tip section change in tangential momentum across the blade row based on the conditions of free-vortex flow. Also, the axial velocity component is held constant radially at a given axial station. Information concerning the upstream and downstream gas total temperature and total temperature, mass flow rate, and flow path geometry permits completion of the calculation.

APPENDIX B

BLADE THROAT DIMENSION CALCULATION PROCEDURE

The blade throat dimension, throat midchannel gas angle, and velocity triangle were determined at the hub, mean, and tip sections using Allison computer program D50. This program requires an assumption on the total pressure gradient from the throat to the exit plane. Further, the program assumes that there is no change in the tangential momentum from the throat to the exit plane. By knowing the total pressure and velocity diagram at the exit plane and the total pressure at the throat, the geometry and flow properties at the throat can be determined by an iteration on continuity, including blockage effects of the blade trailing edge. The calculations are performed radially in ten equal increments.

APPENDIX C

BLADE SURFACE VELOCITY CALCULATION PROCEDURE

This procedure calculates the blade surface velocity of inviscid flow through both a rotating and nonrotating axial blade row. The procedure is accomplished using Allison computer program I87. The procedure satisfies radial equilibrium at the blade midchannel, assuming all radial section midchannel points lie on a radial line. A schematic of the flow model is illustrated in Figure 75. Channel flow theory is used to determine the velocity distribution across the channel at each radial section. Mass flow rate is obtained by numerical integration across the flow orthogonal surface at each axial station. The calculation procedure, as programmed for a digital computer, can be run in either of two modes. Mode 1 iterates on an estimated hub section midchannel velocity to satisfy continuity. Mode 2 calculates what mass flow rate satisfies continuity for a specified hub midchannel velocity. The latter mode is most useful to gain a good insight into the blade shape modifications necessary to obtain a desired velocity distribution. The calculation procedure is restricted to a given axial station and is independent of conditions upstream or downstream of the given axial stations.

The calculation procedure begins by determining the value of midchannel velocities relative to the blade at the mean and tip, $(W_m)_m$ and $(W_m)_t$, which satisfy radial equilibrium for a specified $(W_m)_h$. (Unless otherwise specified, all velocities will be relative to the blade row.) The following equation expresses the relationship between the midchannel velocity at the hub (which has been estimated and is input data) and the midchannel velocity at any other point (Y) along the potential line from hub to tip.

$$(W_m)_Y = \left\{ \exp\left[\int_h^Y a \, dY \right] \right\} \times \left\{ (W_m)_h - \int_h^Y b \exp\left[- \int_h^Y a \, dY \right] dY \right\}$$

where

$$a = - \frac{1}{r} \sin^2 \psi$$

$$b = 2 \omega \sin \psi$$

The preceding equation assumes isentropic flows and constant absolute total (or stagnation) enthalpy, neglects the (Y) component of force exerted by

the blade on the gas, and assumes that the radial potential lines are radial straight lines perpendicular to the axis of rotation. Since straight radial potential lines are assumed, the calculation is limited to flow paths of little or no divergence.

Next, the velocity at evenly spaced increments across the hub, mean, and tip circumferential potential lines is calculated using the method presented in reference 12. The following equation is used to calculate the velocity at various points across the circumferential potential lines.

$$W = (W_m)_Y \left\{ \exp - \left[\frac{no}{2\ \Delta Rc} \left(Rc^2 - Rc_m^2 \right) \right] \right\}$$

The streamline curvature (Rc) is assumed to vary linearly with (no). The (ΔRc) is the change in (Rc) from the reference point (midchannel) to the point where the velocity (W) is to be calculated. Also,

$$Rc_m = \frac{1}{2} \left(Rc_{ps} + Rc_{ss} \right)$$

By assuming (P_{rel}) and (T_{rel}) constant across a given circumferential potential line, the flow rate per unit area (ρW) can be calculated. The flow rate is determined by integrating (ρW) over the plane defined by the hub, mean, and tip circumferential potential lines. For Mode 1 operation, the calculated flow rate is compared to the desired flow rate. If these two values do not agree within a certain iteration tolerance, $(W_m)_h$ is adjusted and the entire calculation is repeated. For Mode 2, the flow rate check is not made. The calculation is completed at this point; therefore, the resulting output is for the original input estimate of $(W_m)_h$.

APPENDIX D

BOUNDARY LAYER ANALYSIS

A prediction of the rate of growth of the blade surface boundary layer was required for determining the location of incipient flow separation. Also, the design of the secondary flow systems of the hollow blades required a fundamental understanding of the boundary layer characteristics of flow on the blade surfaces.

The momentum integral equations for the compressible, turbulent boundary layer along a two-dimensional or axisymmetric surface have been integrated and programmed for the computer. The designation is Allison computer program L42. The integral approach used was that of Culick and Hill (reference 13) which uses the Stewartson-Illingworth (reference 14) transformation to transform the compressible form of the momentum integral equation to a corresponding incompressible form. The turbulent boundary layer calculation procedure of Truckenbrodt (reference 3) was applied to this incompressible form of the equations. The results of the boundary layer calculation procedure were than transformed back to the compressible flow field. Input data for this program consist of free stream total pressure, free stream total temperature, Mach number distribution, and surface geometry. The boundary layer calculation may begin at any point along the surface if initial values of momentum thickness and shape factor are known. Flow separation is said to occur when the incompressible boundary layer shape factor, H_i, exceeds a value of 1.8.

The boundary layer calculation procedure yields the blade surface variation of the momentum thickness, shape factor, displacement thickness, and Reynolds and Mach numbers. It does not, however, render explicitly the actual boundary layer thickness. The boundary layer thickness is determined using the results of an unpublished paper by H. H. Korst who expresses the boundary layer thickness in terms of shape factor, momentum thickness, and Mach number.

Several previous investigations of boundary layer growth under adverse pressure gradients and within the Mach number range of interest (references 15 and 16) were compared to the L42 calculations under the same experimental conditions. Comparison with Englert's data (reference 15) showed agreement within 5 to 10% for calculations of $\overline{\delta}$, θ, and H_i and indicated that separation would occur at or before H_i equals 1.8 under a high adverse pressure gradient. Rubesin's (reference 16) data, which were at a Mach number of from 2.4 to 2.5, indicated very good agreement for $\overline{\delta}$ and θ. Comparisons of H_i showed agreement within 5 to 10%.

It was concluded that the results of program L42 were slightly conservative but sufficiently accurate for the range of Mach numbers encountered in this investigation.

APPENDIX E

TANGENTIAL JET BLOWING BLADE ANALYSIS

The tangential jet blowing blade analysis was made using the equations given in this appendix. Nomenclature for the tangential jet are given in the following sketch. The working curves for the analysis are given in Figures 76 through 82.

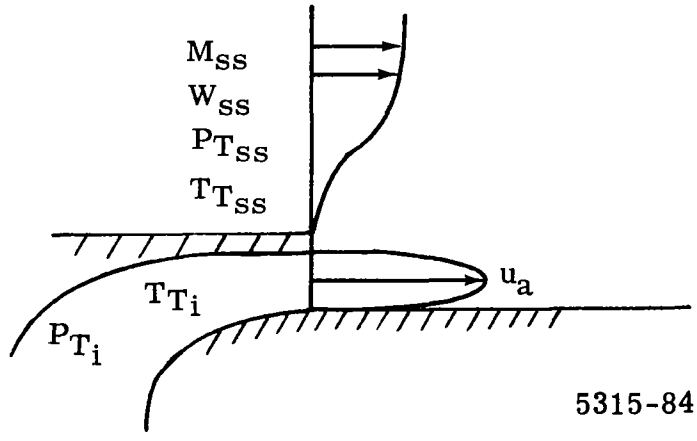

1. $$P_{st_{SS}}/P_{T_{SS}} = 1/\left(1 + \frac{\gamma-1}{2} M_{SS}^2\right)^{\gamma/(\gamma-1)}$$

2. $$P_{st_{SS}} = P_{T_{SS}} \left(P_{st}/P_T\right)_{SS}$$

3. $$P_{st_{SS}} = P_{st_j}$$

4. For a certain P_T

$$M_j = \sqrt{2/(\gamma-1)\left[\left(P_{T_i}/P_{st_j}\right)^{(\gamma-1)/\gamma} - 1\right]}$$

5. $$\frac{u_j'}{u_{j_{cr}}} = \sqrt{\frac{(\gamma+1) M_j^2}{2\left(1 + \frac{\gamma-1}{2} M_j\right)^2}}$$

6. $$u_j' = \frac{u_j'}{u_j'_{cr}} \sqrt{\frac{2\,\gamma\, g\, R\, T_{T_{ss}}}{\gamma + 1}}$$

7. The ratio of total pressure inside the blade to main stream static pressure indicated that the velocity would be supersonic and, therefore, the tangential slot should be a converging-diverging nozzle. However, due to the difficulties in manufacturing a small converging-diverging slot in the blades, it was decided to make the slot a straight-walled passage. Sonic conditions would exist at the throat, and it was assumed that the jet stream would expand isentropically to supersonic conditions just downstream of the nozzle exit. The deviation of the actual jet expansion was corrected for by using a velocity coefficient given by Higgins and Wainwright (reference 17). The velocity coefficient was defined as

$$Cv = \frac{u_a}{u_j'}$$

and was nearly independent of the nozzle expansion ratio. A conservative value of 0.97 was selected for Cv for the analysis so that

$$u_{ja} = 0.97\, u_j'$$

8. $$\rho_{st_j}/\rho_{T_i} = 1/\left(1 + \frac{\gamma-1}{2} M_j^2\right)^{1/\gamma-1}$$

9. $$\rho_{T_i} = \frac{P_{T_i}}{R\, T_{T_{ss}}}$$

10. $$\rho_{st_j} = (\rho_{st_j}/\rho_{T_i})\, \rho_{T_i}$$

11. $$\rho_{st_{ss}}/\rho_{T_{ss}} = 1/\left(1 + \frac{\gamma-1}{2} M_{ss}^2\right)^{1/(\gamma-1)}$$

12. $$\rho_{T_{ss}} = \frac{P_{T_{ss}}}{R\, T_{T_{ss}}}$$

13. $$\rho_{st_{ss}} = \left(\frac{\rho_{st_{ss}}}{\rho_{T_{ss}}}\right) \rho_{T_{ss}}$$

14. $$\frac{W_{ss}}{W_{cr_{ss}}} = \sqrt{\frac{(\gamma + 1)\, M_{ss}^{2}}{2\left(1 + \frac{\gamma - 1}{2} M_{ss}^{2}\right)}}$$

15. $$W_{cr_{ss}} = \sqrt{\frac{2\, \gamma\, g\, R\, T T_{ss}}{\gamma + 1}}$$

16. $$W_{ss} = W_{cr_{ss}} \left(\frac{W_{ss}}{W_{cr_{ss}}}\right)$$

17. For a certain slot height hb,

$$\frac{\dot{m}_j}{\ell} = u_a\, \rho_{st_j}\, hb$$

18. Experimental evidence from Neprud, reference 18, indicates that the actual flow rate through a narrow slot is less than the calculated value by a factor, C_f, of 0.94 (Figure 76) for a slot width of 0.010 in. No data were given above a slot width of 0.010 in. so that the value of $C_f = 0.94$ was applied to the mass flow rate calculations of all slots above 0.010 in.

19. Momentum deficiency, $\rho_{st_{ss}}\, W_{ss}^{2}\, \theta_s$

20. Momentum excess in jet, $\rho_{st_{ss}}\, u_a\, hb\, (u_a - W_{ss})$

21. Jet momentum excess ratio, $$M_R = \frac{\rho_{st_j}\, u_a\, hb\, (u_a - W_{ss})}{\rho_{st_{ss}}\, W_{ss}^{2}\, \theta_s}$$

APPENDIX F

EQUATIONS FOR GENERATION OF JET FLAPPED BLADE FLOW CONDITIONS

The equations used for generating the jet flapped blade flow conditions are given in the following paragraphs. Nomenclature for this blade is shown on the following sketch.

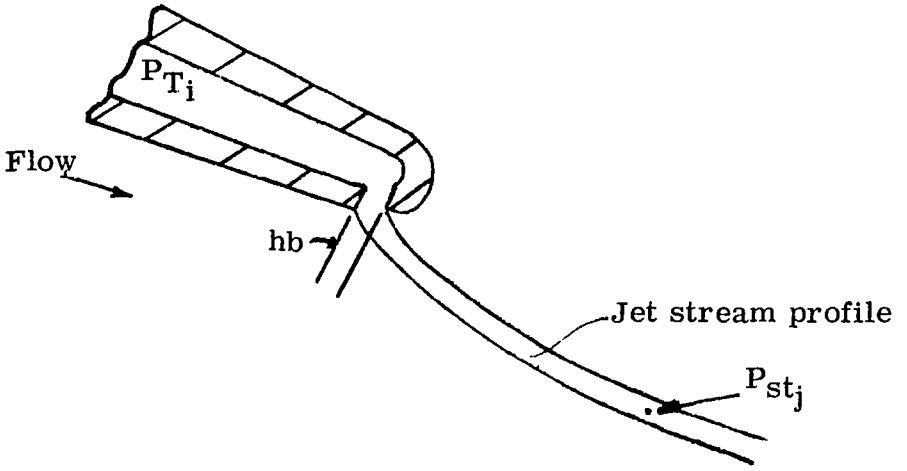

1. Average jet slot width, hb, is a function of jet momentum, M, total inlet to static jet pressure ratio, P_{T_i}/P_{st_j}, and mass flow rate of $\dot{m}_j$.

$$hb = f(M, P_{T_i}/P_{st_j}, \dot{m}_j)$$

2. Average jet momentum,

$$M = \rho_j u_a hb/g \ lb_m/in.$$

3. Mass flow rate,

$$\dot{m}_j = hb \ell \rho_j u_a C_f/144 \ lb_m/sec$$

4. For a certain P_{T_i}/P_{st_j}

$$u_j'/u_{cr} = f(P_{T_i}/P_{st_j}); \ \gamma = 1.4$$

$$u_{cr} = 1019.5 \text{ ft/sec (standard air)}$$

$$u_a = Cv \ u_j'$$

where Cv is 0.97 to account for jet expansion as given by Higgins and Wainwright (reference 17).

5. Values of hb were chosen for certain P_{T_i}/P_{st_j} ratios and jet momentum ratios were calculated. Figure 29 shows a plot of these parameters. A mainstream flow rate of 1.05 lb/sec per passage was used to nondimensionalize $\dot{m}_j$ as a percentage of passage flow rate.

APPENDIX G

DETERMINATION OF THE JET FLAP CONTOUR

Following the method as given by Spence (reference 19), an expression was derived which describes the geometric characteristics of a jet emanating from the trailing edge of an isolated blade. The analysis is based on thin airfoil theory which replaces the blade with a straight line of one unit chord length. Further, the flow model is restricted to two-dimensional, incompressible, irrotational flow. The downwash of the jet is expressed in terms of the second derivative of the jet vertical coordinate. This expression, which is put in terms of the jet momentum coefficient (Cj) and the jet efflux angle (τ), is then integrated twice to determine the jet stream contour. The result is

$$y(x) = \tau \left[2\left(1 - \frac{1}{\sqrt{x}}\right) + 2 A_0 \left\{ \frac{1 + \tan\left(\frac{1}{2}\cos^{-1}\frac{1}{\sqrt{x}}\right)}{1 - \tan\left(\frac{1}{2}\cos^{-1}\frac{1}{\sqrt{x}}\right)} - \sin\left(\cos^{-1}\frac{1}{\sqrt{x}}\right) \right\} \right.$$

$$+ \sum_{n=1}^{N-1} \frac{A_n}{(4_n^2 - 1)} \left\{ \frac{2}{\sqrt{x}} \sin n\left(2\cos^{-1}\frac{1}{\sqrt{x}}\right) \right.$$

$$\left. \left. - 4_n \sin\left(\cos^{-1}\frac{1}{\sqrt{x}}\right) \cos n\left(2\cos^{-1}\frac{1}{\sqrt{x}}\right) \right\} \right]$$

where

y is the jet deflection at a given value of x

A_n (n = 0, 1, ... N-1) are Fourier coefficients and are functions of the jet momentum coefficient (Cj)

n is the number of terms retained in the truncated Fourier series

For the analysis of a jet-flap blade, the unit chord length was taken as the straight-line distance from the intersection of the suction surface and trailing edge flow orthogonal to the suction surface trailing edge. The orientation of the linear airfoil was taken as parallel to $(\psi_4)_m$. The jet contour was terminated when the angle of the contour tangency became equal to (β_3).

APPENDIX H

SOLUTION OF THE LAPLACE EQUATION

Allison computer program P49 is a relaxation solution for the stream function, ψ, of the two-dimensional Laplace equation for flow in a cascade, i.e.,

$$\frac{\partial^2 \psi}{\partial X^2} + \frac{\partial^2 \psi}{\partial Y^2} = 0$$

The value of the stream function is evaluated at up to 2500 nodal points between two blades of a cascade. The stream function is then differentiated with respect to the axial and tangential directions to obtain the corresponding velocity components. That is,

$$u = \frac{\partial \psi}{\partial Y}$$

$$v = - \frac{\partial \psi}{\partial X}$$

These components are then used to calculate the magnitude and direction of the velocity at all of the interior and blade surface nodal points. By using this velocity distribution, an incompressible static pressure distribution can be obtained around the entire blade.

Table I.

Plain blade geometrical and aerodynamic design data.

	Units	Hub	Mean	Tip
C_x	in.	1.365	1.5925	1.820
s	in.	1.01267	1.22967	1.44678
σ		1.348	1.293	1.258
o	in.	0.555	0.763	0.984
β_0	degrees	36.08	41.66	46.37
ψ_0	degrees	53.92	48.34	43.63
$\psi_1)$ straight back	degrees	54.35	49.52	45.23
$*\psi_1)$ W/DS turning	degrees	47.85	43.02	38.73
DS turning	degrees	13.0	13.0	13.0
$\left(\frac{W}{W_{cr}}\right)_0$		0.703	0.623	0.572
$\left(\frac{W_{ss}}{W_{cr}}\right)_{max}$		1.350	1.189	1.082
$\left(\frac{W}{W_{cr}}\right)_2$		0.810	0.713	0.649
$\left(\frac{W}{W_{cr}}\right)_4$		0.799	0.707	0.647
tl	in.	0.0546	0.0637	0.0728
te	in.	0.0175	0.0175	0.0175

$$* \psi_1)_{\text{W/DS turning}} = \psi_1)_{\text{straight back}} - \frac{\text{DS turning}}{2}$$

Table II.

Plain blade section coordinates.

X	Hub		Mean		Tip	
	Suction Y	Pressure Y	Suction Y	Pressure Y	Suction Y	Pressure Y
Min X = 0.0	0.659	—	0.771	—	0.804	—
0.006*	0.685	—	—	—	—	—
0.075*	—	0.609	—	—	—	—
0.021*	—	—	0.818	—	—	—
0.093*	—	—	—	0.714	—	—
0.020*	—	—	—	—	0.853	—
0.093*	—	—	—	—	—	0.734
0.117	0.871	0.629	0.906	0.724	0.946	0.742
0.233	0.969	0.665	0.986	0.757	1.013	0.766
0.350	1.013	0.686	1.037	0.766	1.054	0.774
0.467	1.026	0.687	1.064	0.757	1.076	0.763
0.584	1.005	0.671	1.061	0.731	1.079	0.740
0.700	0.949	0.638	1.020	0.693	1.056	0.706
0.817	0.855	0.584	0.957	0.643	1.014	0.666
0.934	0.736	0.508	0.872	0.584	0.953	0.623
1.050	0.596	0.408	0.768	0.513	0.879	0.571
1.167	0.435	0.288	0.652	0.436	0.790	0.513
1.284	0.254	0.161	0.526	0.350	0.692	0.448
1.362**	0.130	—	—	—	—	—
1.334**	—	0.104	—	—	—	—
1.400	—	—	0.383	0.251	0.586	0.380
1.517	—	—	0.229	0.151	0.469	0.307
1.588**	—	—	0.131	—	—	—
1.563**	—	—	—	0.103	—	—
1.634	—	—	—	—	0.345	0.223
1.750	—	—	—	—	0.208	0.137
1.812**	—	—	—	—	0.132	—
1.788**	—	—	—	—	—	0.106
Max X = 1.365	0.117	—	—	—	—	—
Max X = 1.593	—	—	0.117	—	—	—
Max X = 1.820	—	—	—	—	0.121	—

*Points tangent to leading edge radius: tl_h = 0.0546 in., tl_m = 0.0637 in., tl_t = 0.0728 in.

**Points tangent to trailing edge radius: te_h = 0.0175 in., te_m = 0.0175 in., te_t = 0.0175 in.

Table III.

Design results for placing vortex generators at 30% of surface length.

	Units	Hub	Mean	Tip
C_x	in.	1.365	1.592	1.820
C_s (Figure 7)	in.	1.930	2.030	2.190
S_{VG} at 30% of C_s	in.	0.579	0.610	0.657
X_{VG} (corresponding axial position of S_{VG})	in.	0.440	0.540	0.600
X_s (axial position of incipient separation)	in.	0.595	0.675	0.760
S_s (corresponding surface position of incipient separation)	in.	0.725	0.740	0.820
X (surface distance from general location to point of incipient separation (S_s - S_{VG})	in.	0.146	0.130	0.163
M_{VG} (Mach No. at S_{VG})		1.320	1.240	1.125

Table IV.

Effect of type and position of vortex generators on delaying flow separation (reference 5)
(Separation at S_s = 58.0 in.)

Type of vortex generator	Vortex generator height, h (in.)	Distance between generator location and uncontrolled separation, X (in.)	$\frac{X}{h}$	Location of separation under influence of vortex generators, S_{VG} (in.)	$S_s - S_{VG}$ (in.)	Percent increase in moving point of controlled separation downstream, $\frac{S_s - S_{VG}}{S_s} \times 100\%$
Corotating vane, D/h = 5	0.25	58.0	232.0	76.8	18.8	32.4
Corotating vane, D/h = 3	1.25	53.2	42.5	72.0	14.0	24.1
Triangular plow E1	0.75	46.0	61.2	76.8	18.8	32.4
Triangular plow E2	1.50	23.2	15.4	81.1	23.1	39.8
Counter-rotating vane D/h = 4 d/h = 1	1.75	16.0	9.15	82.9	24.9	42.9
Triangular plow E3	3.0	9.0	3.0	94.8	36.8	63.4

Table V.

Design results for placing co-rotating vortex generators at X_{VG} = 0.22 in.

	Units	Hub	Mean	Tip
X_{VG} (axial distance to vortex generator)	in.	0.22	0.22	0.22
S_{VG} (corresponding surface distance to vortex generator)	in.	0.34	0.275	0.275
S_S (surface position of incipient separation)	in.	0.725	0.740	0.820
X (distance from generator location to point of incipient separation, $S_S - S_{VG}$)	in.	0.385	0.465	0.545
h	in.	0.015	0.015	0.015
$\frac{X}{h}$		25.7	31.0	36.4
$\bar{\delta}$	in.	0.007	0.005	0.005
$\frac{h}{\bar{\delta}}$		2.14	3.00	3.00
D	in.	0.100	0.100	0.100
$\frac{D}{h}$		6.66	6.66	6.66
ℓ	in.	0.06	0.06	0.06
$\frac{\ell}{h}$		4.0	4.0	4.0
t	in.	0.005	0.005	0.005
$\frac{h}{t}$		3.0	3.0	3.0
$W_{ss}/W_{cr_{VG}}$		0.910	1.000	0.980
M_{VG}		0.895	1.000	0.977

Table VI.

Design results for placing counter-rotating vortex generators at X_{VG} = 0.22 in.

	Units	Hub	Mean	Tip
X_{VG}	in.	0.22	0.22	0.22
S_{VG}	in.	0.340	0.275	0.275
S_s	in.	0.725	0.740	0.820
X	in.	0.385	0.465	0.545
h	in.	0.020	0.020	0.020
$\frac{X}{h}$		19.25	23.2	27.3
$\bar{\delta}$	in.	0.007	0.005	0.005
$\frac{h}{\bar{\delta}}$		2.86	4.00	4.00
$\frac{D}{h}$		10.0	10.0	10.0
D	in.	0.20	0.20	0.20
$W/W_{cr_{VG}}$		0.910	1.000	0.980
M_{VG}		0.895	1.000	0.977

Table VII.

Summary of slot parameters for tangential jet slot location No. 1.

1. Slot height = 0.020 in. 2. Slot height = 0.030 in. 3. Slot height = 0.040 in.			
	Hub	Mean	Tip
Jet momentum excess ratio, M_R	1. 2.22 2. 2.12 3. 1.92	2.50 2.50 2.50	2.45 2.47 2.42
Core to main stream total pressure ratio, P_{Ti}/P_{Tss}	1. 1.71 2. 1.40 3. 1.27	1.71 1.40 1.27	1.71 1.40 1.27
Jet to main stream velocity ratio, u_a/W_{ss}	1. 1.145 2. 1.087 3. 1.054	1.195 1.122 1.081	1.244 1.152 1.104
Jet to main stream mass flow rate ratio, $\% \dot{m}_s/\dot{m}_p$	1. 2.32 2. 3.80 3. 5.23	2.60 4.13 5.72	2.72 4.37 5.96
Integrated mass flow ratio, $\% \dot{m}_s/\dot{m}_p$	1. 2.590 2. 4.167 3. 5.717	2.590 4.167 5.717	2.590 4.167 5.717
Axial slot position, in.	0.540	0.610	0.690

Table VIII.

Boundary layer and aerodynamic data for tangential jet slot location No. 1.

	Units	Hub	Mean	Tip
X_s	in.	0.595	0.675	0.760
$\bar{\delta}_s$	in.	0.010	0.0125	0.0145
$\Delta S = 6\,\bar{\delta}_s$	in.	0.060	0.075	0.087
S_s	in.	0.725	0.745	0.825
$S = S_s - \Delta S$	in.	0.665	0.670	0.738
X	in.	0.540	0.610	0.690
W_{ss}/W_{cr}		1.350	1.180	1.040
θ_s	in.	0.00122	0.00165	0.00197
$\frac{\Delta P_s/\delta_0}{\Delta S_{te}}$	psi/in.	4.10	3.16	2.63

Table IX.

Summary of slot parameters for tangential jet slot location No. 2.

1. Slot height = 0.020 in.
2. Slot height = 0.030 in.
3. Slot height = 0.040 in.

		Hub	Mean	Tip
Jet momentum excess ratio, M_R	1.	2.70	2.50	2.25
	2.	2.75	2.50	2.25
	3.	2.70	2.50	2.30
Core to main stream total pressure ratio, $P_{T_i}/P_{T_{ss}}$	1.	1.38	1.38	1.38
	2.	1.28	1.28	1.28
	3.	1.18	1.18	1.18
Jet to main stream velocity ratio, u_a/W_{ss}	1.	1.188	1.230	1.246
	2.	1.121	1.150	1.162
	3.	1.090	1.107	1.119
Jet to main stream mass flow rate ratio, $\% \dot{m}_s/\dot{m}_p$	1.	3.05	3.05	3.05
	2.	4.62	4.62	4.62
	3.	6.20	6.20	6.20
Integrated mass flow ratio, $\% \dot{m}_s/\dot{m}_p$	1.	3.05	3.05	3.05
	2.	4.62	4.62	4.62
	3.	6.20	6.20	6.20
Axial position of slot, in.		0.795	0.900	1.010

Table X.

Boundary layer and aerodynamic data for tangential jet slot location No. 2.

	Units	Hub	Mean	Tip
X	in.	0.795	0.900	1.010
S for constant $\frac{\Delta P_{st}/\delta_0}{\Delta S_{te}}$	in.	0.965	1.02	1.10
$\frac{\Delta P_{st}}{\delta_0} \Big/ \Delta S_{te}$	psi/in.	1.07	1.07	1.07
W_{ss}/W_{cr}		0.94	0.86	0.835
θ_s	in.	0.00122	0.00165	0.00197

Table XI.

Jet flow characteristics downstream of slot locations 1 and 2.

Slot location 1			
	Hub	Mean	Tip
Transverse jet growth at throat, in.	0.0347	0.0452	0.0529
Transverse jet velocity at throat, ft/sec	716	686	633
Slot location 2			
	Hub	Mean	Tip
Transverse jet growth at throat, in.	0.039	0.0425	0.0458
Transverse jet velocity at throat, ft/sec	1012	997	913

Table XII.

Blade core flow characteristics for slot locations 1 and 2.

	hb (in.)	Mass flow rate (lb/sec)	Flow area ($in.^2$)	Radial velocity (ft/sec)
Slot location No. 1	0.020	0.0272	0.157	194
	0.030	0.0438	0.157	383
	0.040	0.0601	0.157	579
Slot location No. 2	0.020	0.0320	0.152	293
	0.030	0.0485	0.152	498
	0.040	0.0651	0.152	697

Table XIII.

Results of final check on continuity and simple radial equilibrium for jet flapped blade design.

	Units	Hub	Mean	Tip
Velocity from iteration results, $W_{m_1}/\sqrt{\Theta}_{cr}$	ft/sec	852.0	779.0	735.0
Velocity required for radial equilibrium, $W_{m_1}/\sqrt{\Theta}_{cr}$	ft/sec	852.0	780.03	736.13
Mass flow rate calculated from throat conditions, $(\dot{m}_p \sqrt{\Theta}_{cr})/\delta_0$	lb/sec	67.81		
Mass flow rate required, $(\dot{m}_p \sqrt{\Theta}_{cr})/\delta_0$	lb/sec	68.4		

Table XIV.

Iteration results at the midchannel throat for jet flapped blade design.

	Units	Hub	Mean	Tip
Jet efflux angle, τ	degrees	80.0	84.7	90.0
Slot tool angle, ζ	degrees	34.04	34.04	34.04
Throat angle, ψ_1	degrees	45.16	39.34	34.09
Deflection angle, Θ	degrees	8.8	9.2	9.8
Jet momentum coefficient, C_j		0.156	0.141	0.127
Throat dimension, o	in.	0.535	0.736	0.953
Midchannel velocity, W_{m_1}	ft/sec	852.0	779.0	735.0

Table XV.

Evaluation of the jet effect on tangential momentum for jet flapped blade design.

(Section momentum proportional to area, A, under static pressure blade chord curve)

	Hub	Mean	Tip
1. $A = \int_0^{C_x} \frac{\Delta P_{st}}{\delta_0} dx$, in.^{2}			
Plain blade, A_1	16.17	17.02	17.63
Jet flap w/o jet, A_2	15.43	15.16	16.67
Jet flap w/jet, A_3	17.78	17.18	18.99
2. ΔW_u, ft/sec			
Plain blade			
Throat	1192	972	819
Downstream	1251	1027	873
Jet flap			
Throat	1179	965	813
Downstream	1251	1027	873
Method 1, throat jet flap $\Delta W_1 \times A_3/A_2$	1356	1095	927
Method 2, downstream jet flap $\Delta W_{u_4} \times A_3/A_1$	1377	1040	938
3. Percent deviation from plain blade, ΔW_u			
Method 1	8.2	6.3	6.1
Method 2	10.0	1.0	7.6

Table XVI.

Summary of jet-flapped blade interior parameters.

	Units	Hub	Mean	Tip
Core area	$in.^2$	0.1626	0.207	0.266
Core velocity at the hub with 4.4% flow	ft/sec		389	

Table XVII.

NASA annular cascade jet-flapped blade design data.

	Units	Hub	Mean	Tip
C_x	in.	1.2285	1.4555	1.6835
s	in.	1.01267	1.22967	1.44678
σ		1.213	1.185	1.164
tl	in.	0.04	0.04	0.04
te	in.	0.05	0.05	0.05
β_0	degrees	36.08	41.66	46.37
ψ_1	degrees	45.16	39.34	34.09
$W/W_{cr})_0$		0.703	0.623	0.572
$\left(\frac{W_{ss}}{W_{cr}}\right)_{max}$, w/o jet		1.380	1.210	1.095
$W/W_{cr})_4$		0.812	0.721	0.662

Table XVIII.

Jet flapped blade section coordinates.

X	Hub		Mean		Tip	
	Suction	Pressure	Suction	Pressure	Suction	Pressure
	Y	Y	Y	Y	Y	Y
Min X = 0.0	0.410	—	0.444	—	0.475	—
0.005*	0.430	—	—	—	—	—
0.060*	—	0.376	—	—	—	—
0.006*	—	—	0.463	—	—	—
0.050*	—	—	—	0.407	—	—
0.009*	—	—	—	—	0.500	—
0.054*	—	—	—	—	—	0.438
0.100	0.591	0.396	0.587	0.425	0.607	0.454
0.200	0.699	0.439	0.688	0.461	0.696	0.483
0.300	0.768	0.472	0.758	0.489	0.754	0.505
0.400	0.804	0.490	0.801	0.507	0.797	0.517
0.500	0.812	0.495	0.824	0.517	0.827	0.522
0.600	0.797	0.486	0.829	0.518	0.842	0.517
0.700	0.750	0.461	0.814	0.505	0.845	0.509
0.800	0.674	0.416	0.780	0.474	0.833	0.491
0.900	0.576	0.348	0.725	0.429	0.805	0.465
1.000	0.455	0.250	0.648	0.370	0.760	0.434
1.100	0.316	0.126	0.555	0.299	0.701	0.394
1.200	0.162	—	0.451	0.217	0.624	0.344
1.222**	0.127	—	—	—	—	—
1.143**	—	0.067	—	—	—	—
1.300	—	—	0.332	0.130	0.534	0.285
1.400	—	—	0.195	—	0.435	0.218
1.447**	—	—	0.128	—	—	—
1.370**	—	—	—	0.064	—	—
1.500	—	—	—	—	0.328	0.145
1.600	—	—	—	—	0.217	—
1.673**	—	—	—	—	0.131	—
1.601**	—	—	—	—	—	0.064
Max X = 1.228	0.100	—	—	—	—	—
Max X = 1.456	—	—	0.100	—	—	—
Max X = 1.684	—	—	—	—	0.100	—

*Points tangent to leading edge radius: tl_h = 0.040 in., tl_m = 0.040 in., tl_t = 0.040 in.

**Points tangent to trailing edge radius: te_h = 0.050 in., te_m = 0.050 in., te_t = 0.050 in.

Table XIX.

Suction surface diffusion parameters for tandem blade.

	Primary blade			Secondary blade		
	$\left(\frac{W}{W_{cr}}\right)_{pte}$	$\left(\frac{W}{W_{cr}}\right)_{max}$	Ds_p	$\left(\frac{W}{W_{cr}}\right)_{ste}$	$\left(\frac{W}{W_{cr}}\right)_{max}$	Ds_s
Hub	0.835	0.942	0.114	0.81	1.047	0.226
Mean	0.725	0.853	0.150	0.713	0.915	0.221
Tip	0.720	0.883	0.185	0.649	0.845	0.232

Table XX.

Tandem blade design data.

	Units	Hub	Mean	Tip
C_x	in.	1.2290	1.4555	1.6835
s	in.	1.01267	1.22967	1.44678
σ		1.213	1.185	1.164
tl_p	in.	0.030	0.030	0.030
te_p	in.	0.0175	0.0175	0.0175
tl_s	in.	0.05	0.05	0.05
te_s	in.	0.0175	0.0175	0.0175
β_0	degrees	36.08	41.66	46.37
ψ_1	degrees	46.85	42.05	37.80
DS turning	degrees	15.0	15.0	15.0
$\left(\frac{W}{W_{cr}}\right)_0$		0.703	0.623	0.572
$\left(\frac{W}{W_{cr}}\right)_{max}$		1.047	0.915	0.883
$\left(\frac{W}{W_{cr}}\right)_4$		0.799	0.707	0.647

Table XXI.

Tandem blade section coordinates.

X	Hub		Mean		Tip	
	Suction Y	Pressure Y	Suction Y	Pressure Y	Suction Y	Pressure Y
Min X = 0.0	0.878	—	1.057	—	1.158	—
0.002*	0.892	—	—	—	—	—
0.052*	—	0.858	—	—	—	—
0.005*	—	—	1.074	—	—	—
0.050*	—	—	—	1.033	—	—
0.010*	—	—	—	—	1.180	—
0.045*	—	—	—	—	—	1.132
0.10	1.032	0.914	1.175	1.069	1.197	1.098
0.20	1.106	0.994	1.224	1.124	1.271	1.162
0.30	1.141	1.037	1.250	1.158	1.310	1.207
0.40	1.147	1.053	1.259	1.175	1.326	1.234
0.50	1.126	1.044	1.251	1.172	1.326	1.243
0.60	1.079	1.012	1.223	1.150	1.310	1.237
0.70	1.004	0.961	1.173	1.110	1.280	1.218
0.727**	0.980	—	—	—	—	—
0.707**	—	0.955	—	—	—	—
0.80	—	—	1.100	—	1.237	1.187
0.815**	—	—	1.087	—	—	—
0.792**	—	—	—	1.056	—	—
0.90	—	—	—	—	1.185	—
0.905**	—	—	—	—	1.184	—
0.888**	—	—	—	—	—	1.153
Max X = 0.731	0.970	—	—	—	—	—
Max X = 0.82	—	—	1.078	—	—	—
Max X = 0.912	—	—	—	—	1.169	—
Min X = 0.30	0.774	—	—	—	—	—
Min X = 0.35	—	—	0.829	—	—	—
Min X = 0.407	—	—	—	—	0.912	—
0.316†	0.811	—	—	—	—	—
0.354†	—	0.723	—	—	—	—
0.362†	—	—	0.862	—	—	—
0.401†	—	—	—	0.779	—	—
0.435†	—	—	—	—	0.958	—
0.45†	—	—	—	—	—	0.863
0.40	0.857	0.725	0.898	—	—	—

Table XXI. (cont)

X	Hub		Mean		Tip	
	Suction Y	Pressure Y	Suction Y	Pressure Y	Suction Y	Pressure Y
0.50	0.867	0.716	0.938	0.773	0.975	0.858
0.60	0.843	0.678	0.934	0.749	0.975	0.840
0.70	0.793	0.615	0.896	0.708	0.949	0.807
0.80	0.712	0.529	0.838	0.650	0.907	0.757
0.90	0.596	0.431	0.762	0.578	0.853	0.697
1.00	0.467	0.321	0.670	0.495	0.790	0.627
1.10	0.322	0.206	0.566	0.405	0.714	0.552
1.20	0.156	—	0.452	0.310	0.629	0.473
1.227††	0.108	—	—	—	—	—
1.198††	—	0.089	—	—	—	—
1.30	—	—	0.327	0.214	0.536	0.390
1.40	—	—	0.188	0.115	0.434	0.306
1.453††	—	—	0.111	—	—	—
1.425††	—	—	—	0.088	—	—
1.50	—	—	—	—	0.328	0.220
1.60	—	—	—	—	0.211	0.134
1.68††	—	—	—	—	0.109	—
1.653††	—	—	—	—	—	0.088
Max X = 1.229	0.100	—	—	—	—	—
Max X = 1.456	—	—	0.100	—	—	—
Max X = 1.684	—	—	—	—	0.100	—

*Points tangent to leading edge radius: tl_{ph} = 0.030 in., tl_{pm} = 0.030 in., tl_{pt} = 0.030 in.

**Points tangent to trailing edge radius: te_{ph} = 0.0175 in., te_{pm} = 0.0175 in., te_{pt} = 0.0175 in.

† Points tangent to leading edge radius: tl_{sh} = 0.050 in., tl_{sm} = 0.050 in., tl_{st} = 0.050 in.

†† Points tangent to trailing edge radius: te_{sh} = 0.0175 in., te_{sm} = 0.0175 in., te_{st} = 0.0175 in.

Table XXII.

Blade force analysis.

Section	Unit force, $F/\delta_0/\ell$	X coord of load point	Y coord of load point	Axial force, Fx/δ_0	Tangential force, Fy/δ_0	Total force, F/δ_0	Angle of action (degrees)
Plain blade							
Hub 0	6.541	0.588	0.645	0.974	3.548	3.679	105.4
$\ell/4$	6.805	0.560	Press. surface	1.436	7.520	7.656	100.4
Mean $\ell/2$	6.777	0.542	0.632	0.997	7.559	7.624	97.5
$3\ell/4$	6.740	0.538	Press. surface	0.584	7.560	7.583	94.4
Tip ℓ	6.462	0.532	0.728	0.094	3.634	3.635	91.5
Jet flap without jet							
Hub 0	6.274	0.577	0.492	0.661	3.467	3.529	100.8
$\ell/4$	6.400	0.622	Press. surface	1.492	7.040	7.190	102.1
Mean $\ell/2$	6.622	0.667	0.516	1.713	7.250	7.450	103.3
$3\ell/4$	7.020	0.713	Press. surface	1.988	7.650	7.900	104.6
Tip ℓ	7.770	0.759	0.463	1.202	4.200	4.370	106.0
Jet flap with jet							
Hub 0	8.636	0.711	0.460	2.001	4.426	4.857	114.3
$\ell/4$	8.774	0.705	Press. surface	3.940	9.050	9.870	113.5
Mean $\ell/2$	9.044	0.812	0.469	3.940	9.381	10.175	112.8
$3\ell/4$	9.339	0.858	Press. surface	3.980	9.723	10.506	112.2
Tip ℓ	9.675	0.902	0.462	2.025	5.051	5.442	111.9
Tandem primary							
Hub 0	2.227	0.292	1.045	-0.1882	1.239	1.253	89.1
$\ell/4$	2.261	0.324	Press. surface	-0.025	2.537	2.537	90.4
Mean $\ell/2$	2.273	0.338	1.170	0.0164	2.557	2.557	90.6
$3\ell/4$	2.276	0.343	Press. surface	-0.070	2.556	2.557	90.2
Tip ℓ	2.271	0.342	1.217	-0.1343	1.270	1.277	89.4
Tandem secondary							
Hub 0	4.312	0.723	0.596	1.529	1.882	2.426	129.1
$\ell/4$	4.02	0.704	Press. surface	2.455	3.700	4.440	123.1
Mean $\ell/2$	3.798	0.712	0.700	2.186	3.672	4.273	120.8
$3\ell/4$	3.685	0.774	Press. surface	2.120	3.657	4.227	120.1
Tip ℓ	3.778	0.922	0.679	1.084	1.828	2.125	120.7

Table XXIII.

Stress analysis results for blades in a cantilevered condition.

Type	Max bending stress at hub (psi)	First mode frequency (cps)	Tip deflection (in.)	
			Axial	Tangential
Plain	4,387	399.5	0.0017	0.0049
Tangential jet 1	8,419	447.1	0.0039	0.0091
Tangential jet 2	7,956	464.3	0.0035	0.0083
Jet flap	12,799	514.0	0.0016	0.0100
Tandem (cantilevered)				
Primary	20,386	193.3	0.0047	0.0513
Secondary	5,384	201.8	0.0063	0.0098

Table XXIV.

Stress analysis results for tandem blade configuration in fixed end condition.

Type	Max bending stress at hub (psi)	First mode frequency (cps)	Max deflection normal to I_{min} axis (in.)
Tandem (fixed end)			
Primary	3931	1240	0.00126
Secondary	2860	1307	0.0007

Table XXV.

Plain and vortex generator blades—static pressure tap locations.

Lower blade				Upper blade			
Tap No.	Axial location (in.)	Section	Surface	Tap No.	Axial location (in.)	Section	Surface
1	0.150	Hub	Suction	32	0.150	Hub	Pressure
2	0.540	↓	↓	33	0.400	↓	↓
3	0.710	↓	↓	34	0.790	↓	↓
4	0.850	↓	↓	35	1.110	↓	↓
5	0.980	↓	↓	36	0.530	Mean	Suction
6	1.090	↓	↓	37	0.720	↓	↓
7	1.200	↓	↓	38	1.020	↓	↓
8	1.300	↓	↓	39	0.015	↓	Pressure
9	0.100	Mean	↓	40	0.150	↓	↓
10	0.180	↓	↓	41	0.370	↓	↓
11	0.290	↓	↓	42	0.590	↓	↓
12	0.400	↓	↓	43	0.800	↓	↓
13	0.530	↓	↓	44	0.990	↓	↓
14	0.620	↓	↓	45	1.175	↓	↓
15	0.720	↓	↓	46	1.350	↓	↓
16	0.875	↓	↓	47	0.300	Tip	↓
17	1.020	↓	↓	48	0.660	↓	↓
18	1.160	↓	↓	49	1.005	↓	↓
19	1.295	↓	↓	50	1.330	↓	↓
20	1.420	↓	↓				
21	1.540	↓	↓				
22	0.150	↓	Pressure				
23	1.350	↓	↓				
24	0.150	Tip	Suction				
25	0.450	↓	↓				
26	0.680	↓	↓				
27	0.890	↓	↓				
28	1.090	↓	↓				
29	1.270	↓	↓				
30	1.445	↓	↓				
31	1.610	↓	↓				

Table XXVI.

Tangential jet slot location No. 1—static pressure tap locations.

Lower blade				Upper blade			
Tap No.	Axial location (in.)	Section	Surface	Tap No.	Axial location (in.)	Section	Surface
1	0.150	Hub	Suction	32	0.150	Hub	Pressure
2	0.420	↓	↓	33	0.400	↓	↓
3	0.685	↓	↓	34	0.790	↓	↓
4	0.830	↓	↓	35	1.110	↓	↓
5	0.965	↓	↓	36	0.510	Mean	Suction
6	1.080	↓	↓	37	1.080	↓	↓
7	1.195	↓	↓	38	0.25 (int)	↓	Pressure
8	1.300	↓	↓			↓	↓
9	0.100	Mean	↓	39	0.015	↓	↓
10	0.180	↓	↓	40	0.150	↓	↓
11	0.290	↓	↓	41	0.370	↓	↓
12	0.400	↓	↓	42	0.590	↓	↓
13	0.510	↓	↓	43	0.800	↓	↓
14	0.800	↓	↓	44	0.990	↓	↓
15	0.945	↓	↓	45	1.175	↓	↓
16	1.080	↓	↓	46	1.350	↓	↓
17	1.205	↓	↓	47	0.300	Tip	↓
18	1.320	↓	↓	48	0.660	↓	↓
19	1.430	↓	↓	49	1.005	↓	↓
20	1.540	↓	↓	50	1.330	↓	↓
21	1.25 (int)	↓	Pressure				
22	0.150	↓	↓				
23	1.350	↓	↓				
24	0.150	Tip	Suction				
25	0.450	↓	↓				
26	0.570	↓	↓				
27	0.860	↓	↓				
28	1.055	↓	↓				
29	1.240	↓	↓				
30	1.420	↓	↓				
31	1.590	↓	↓				

Table XXVII.

Tangential jet slot location No. 2—static pressure tap locations.

Lower blade				Upper blade			
Tap No.	Axial location (in.)	Section	Surface	Tap No.	Axial location (in.)	Section	Surface
1	0.150	Hub	Suction	31	0.150	Hub	Pressure
2	0.270	↓	↓	32	0.400	↓	↓
3	0.400	↓	↓	33	0.790	↓	↓
4	0.540	↓	↓	34	1.110	↓	↓
5	0.710	↓	↓	35	0.530	Mean	Suction
6	1.065	↓	↓	36	0.675	↓	↓
7	1.180	↓	↓	37	1.070	↓	↓
8	1.295	↓	↓	38	0.3 (int)	↓	Pressure
9	0.100	Mean	↓			↓	↓
10	0.180	↓	↓	39	0.015	↓	↓
11	0.290	↓	↓	40	0.150	↓	↓
12	0.400	↓	↓	41	0.370	↓	↓
13	0.530	↓	↓	42	0.590	↓	↓
14	0.675	↓	↓	43	0.800	↓	↓
15	0.810	↓	↓	44	0.990	↓	↓
16	1.070	↓	↓	45	1.175	↓	↓
17	1.190	↓	↓	46	1.350	↓	↓
18	1.305	↓	↓	47	0.300	Tip	↓
19	1.425	↓	↓	48	0.660	↓	↓
20	1.540	↓	↓	49	1.005	↓	↓
21	0.3 (int)	↓	Pressure	50	1.330	↓	↓
22	0.150	↓	↓			↓	↓
23	1.350	↓	↓			↓	↓
24	0.150	Tip	Suction			↓	↓
25	0.450	↓	↓			↓	↓
26	0.680	↓	↓			↓	↓
27	0.890	↓	↓			↓	↓
28	1.320	↓	↓			↓	↓
29	1.470	↓	↓			↓	↓
30	1.610	↓	↓			↓	↓

Table XXVIII.

Jet flapped blade—static pressure tap locations.

Lower blade				Upper blade			
Tap No.	Axial location (in.)	Section	Surface	Tap No.	Axial location (in.)	Section	Surface
1	0.185	Hub	Suction	30	0.255	Hub	Pressure
2	0.470	↓	↓	31	0.575	↓	↓
3	0.625			32	0.875		
4	0.765			33	1.100		
5	0.880			34	0.350	Mean	Suction
6	0.980			35	0.675	↓	↓
7	1.080			36	0.975		
8	1.170			37	1.215		
9	0.090	Mean		38	1.420		
10	0.170	↓		39	0.015		Pressure
11	0.265			40	0.017		↓
12	0.350			41	0.380		
13	0.510			42	0.600		
14	0.675			43	0.810		
15	0.830			44	1.000		
16	0.975			45	1.180		
17	1.100			46	1.340		
18	1.215			47	0.3 (int)		
19	1.325						
20	1.420			48	0.420	Tip	
21	0.3 (int)		Pressure	49	0.790	↓	
				50	1.130		
22	0.320	Tip	Suction				
23	0.655	↓	↓				
24	0.825						
25	0.985						
26	1.130						
27	1.270						
28	1.390						
29	1.510						

Table XXIX.

Tandem blade static pressure tap locations.

Lower blade				Upper blade			
Tap No.	Axial location (in.)	Section	Surface	Tap No.	Axial location (in.)	Section	Surface
1	0.050	Hub	Primary suction	33	0.230	Hub	Primary pressure
2	0.220			34	0.550		
3	0.444			35	0.480		Secondary pressure
4	0.650		Secondary suction	36	0.900		
5	0.380			37	0.050	Mean	Primary pressure
6	0.637			38	0.214		
7	0.842			39	0.396		
8	1.010			40	0.580		
9	1.160			41	0.750		
10	0.050	Mean	Primary suction	42	0.400		Secondary pressure
11	0.220			43	0.623		
12	0.415			44	0.820		
13	0.610			45	1.000		
14	0.780			46	1.170		
15	0.358			47	1.330		
16	0.400			48	0.300	Tip	Primary pressure
17	0.577			49	0.550		Secondary pressure
18	0.752			50	1.250		
19	0.910		Secondary suction				
20	1.050						
21	1.180						
22	1.298						
23	1.410						
24	0.050	Tip	Primary suction				
25	0.270						
26	0.540						
27	0.800						
28	0.500		Secondary suction				
29	0.810						
30	1.090						
31	1.330						
32	1.555						

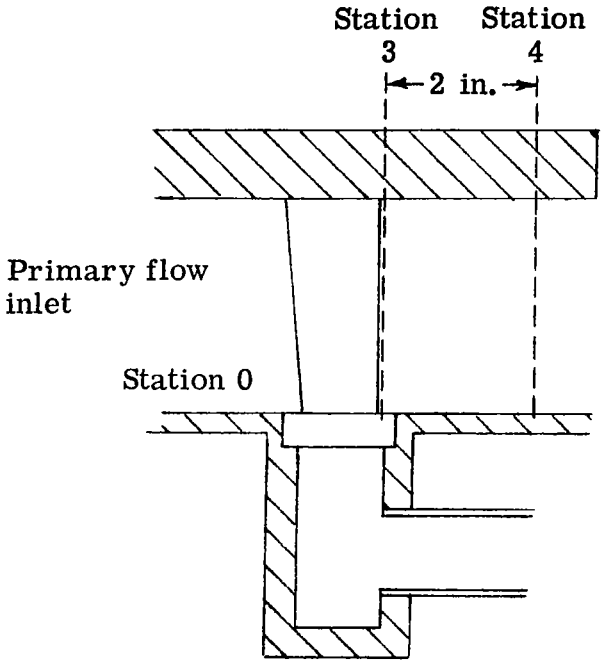

(a) Flow path schematic

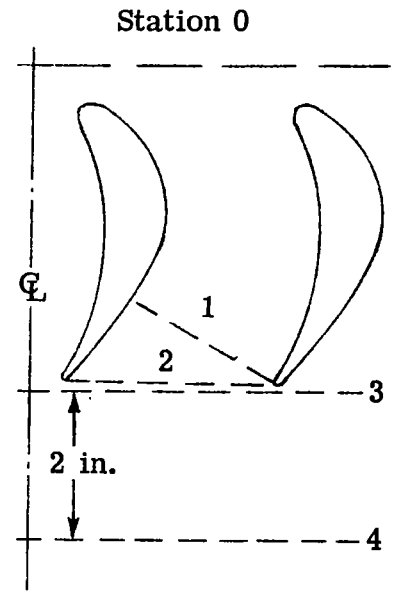

(b) Axial station nomenclature

5315-56

Figure 1. Flow path schematic and axial station nomenclature.

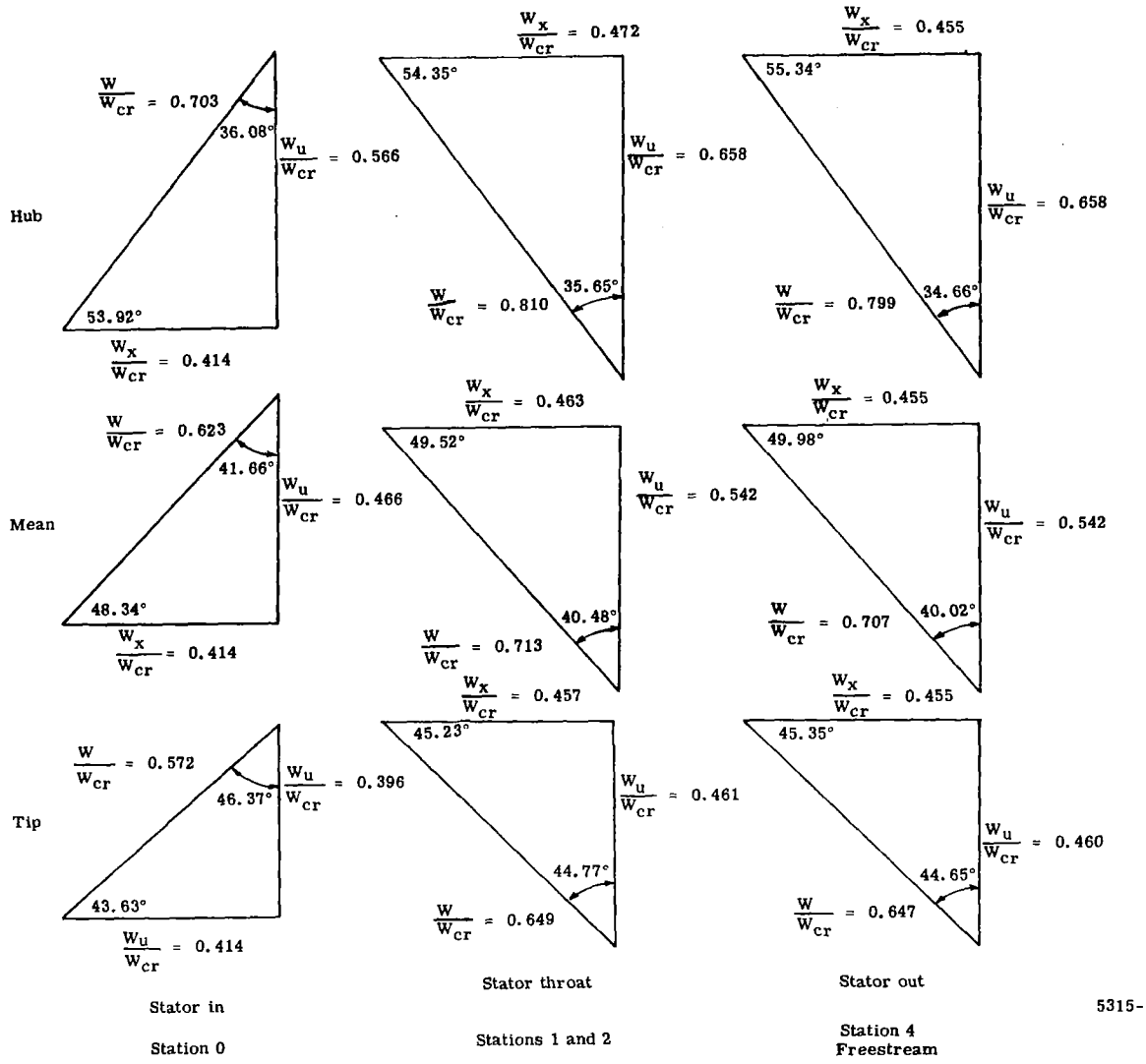

Figure 2. Stator velocity diagrams for zero secondary flow. (See Table I)

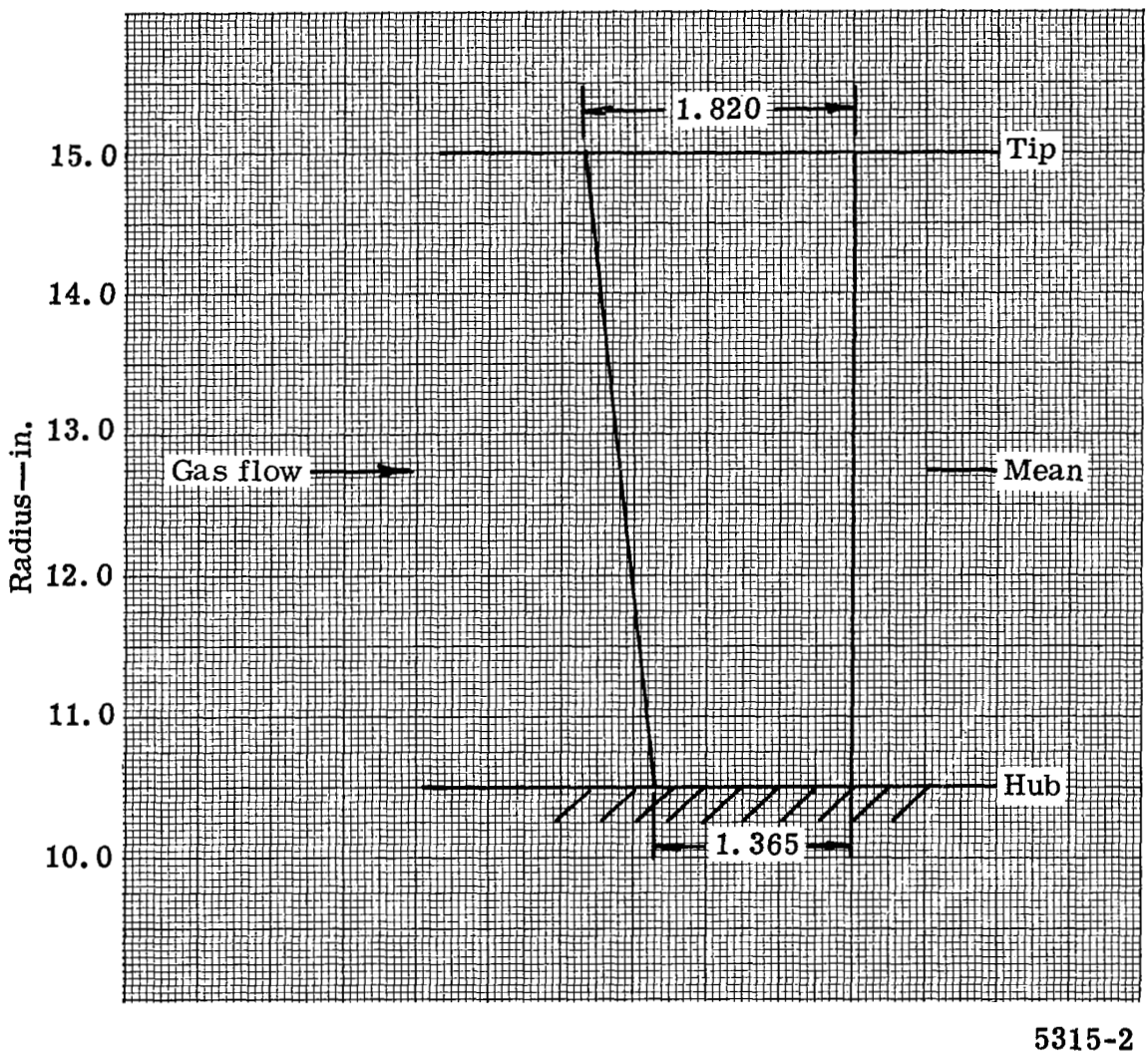

Figure 3. Elevation view of plain blade configuration.

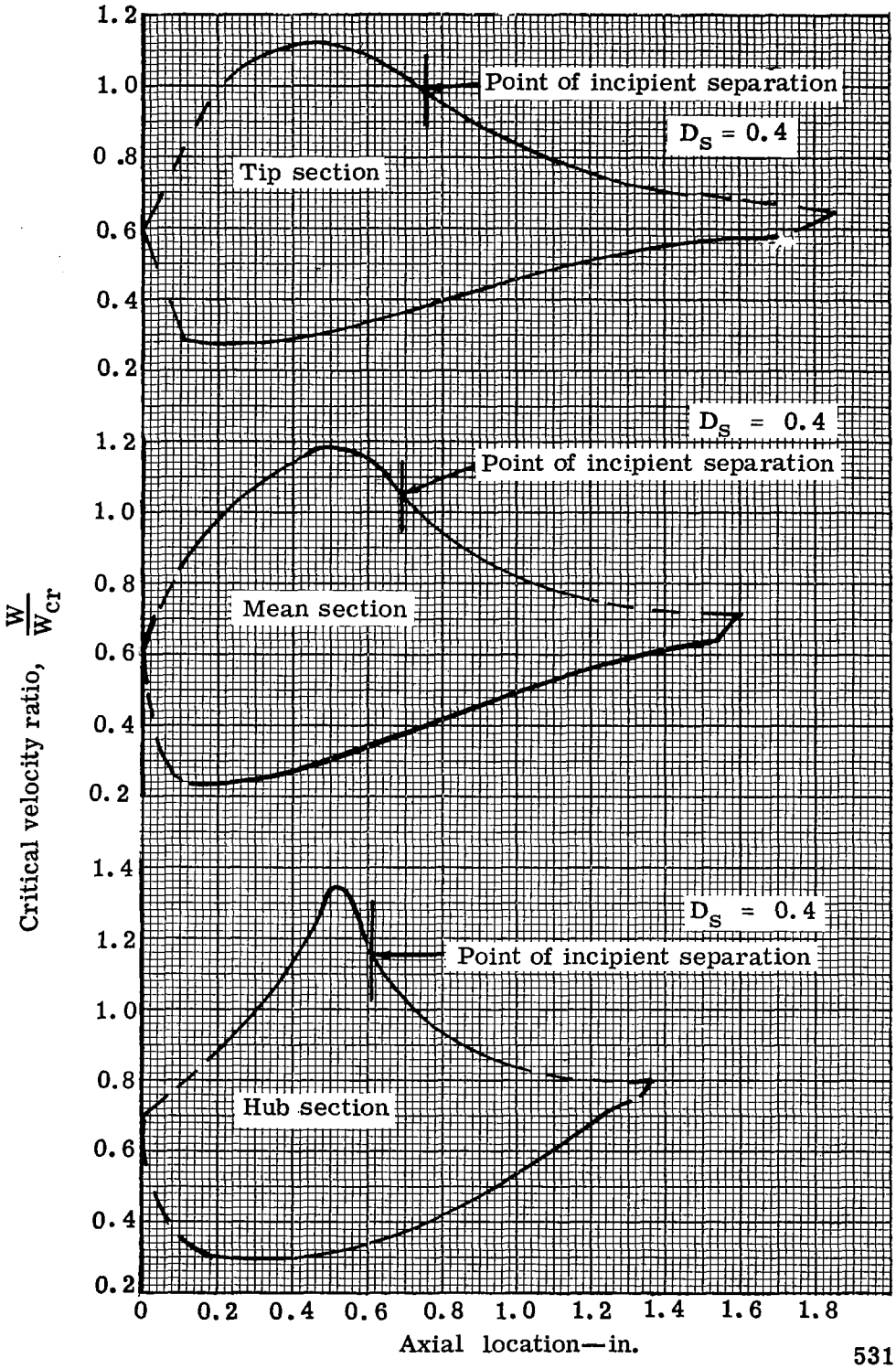

Figure 4. Plain blade surface velocity distribution.

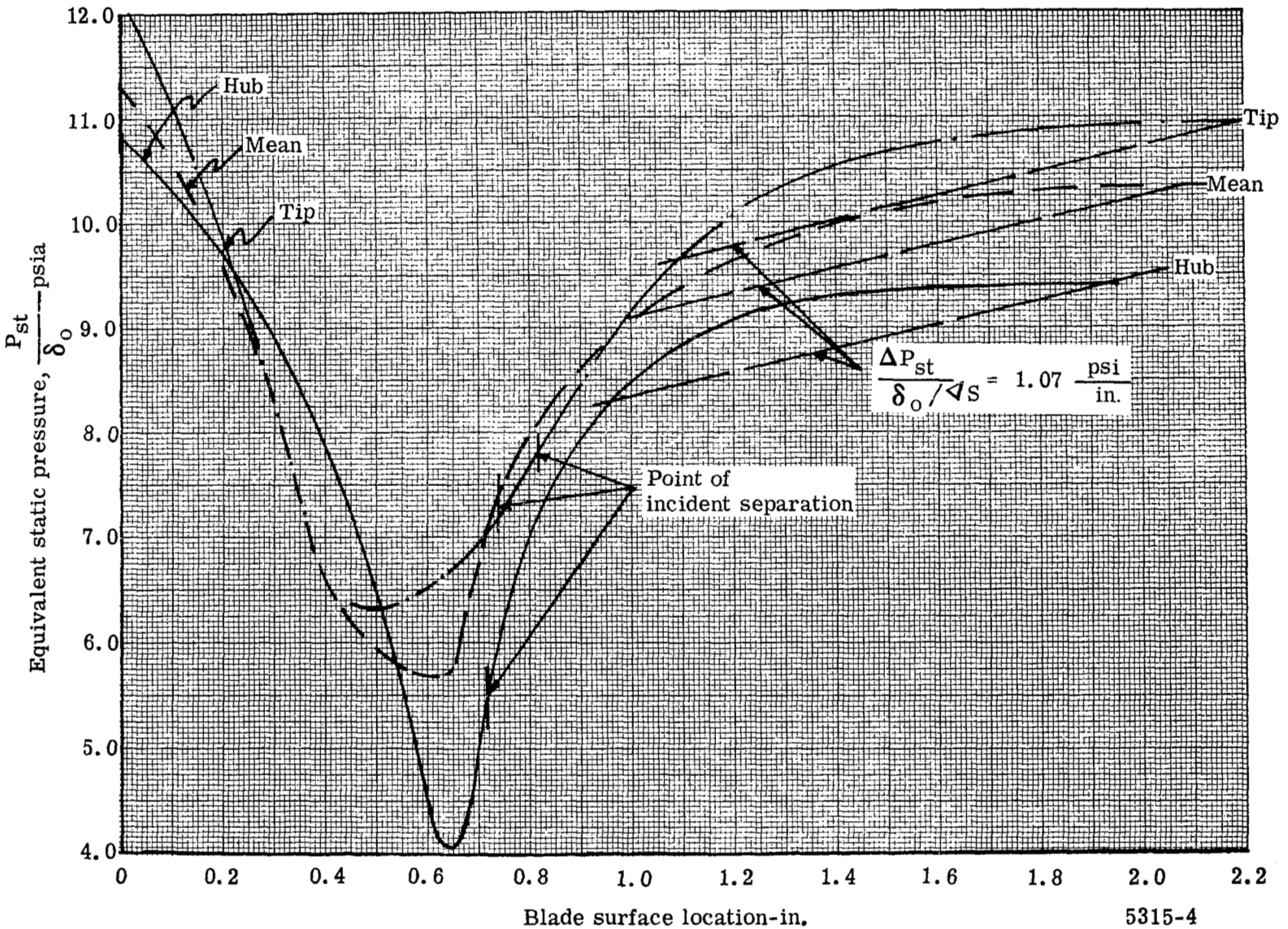

Figure 5. Plain blade suction surface static pressure distribution.

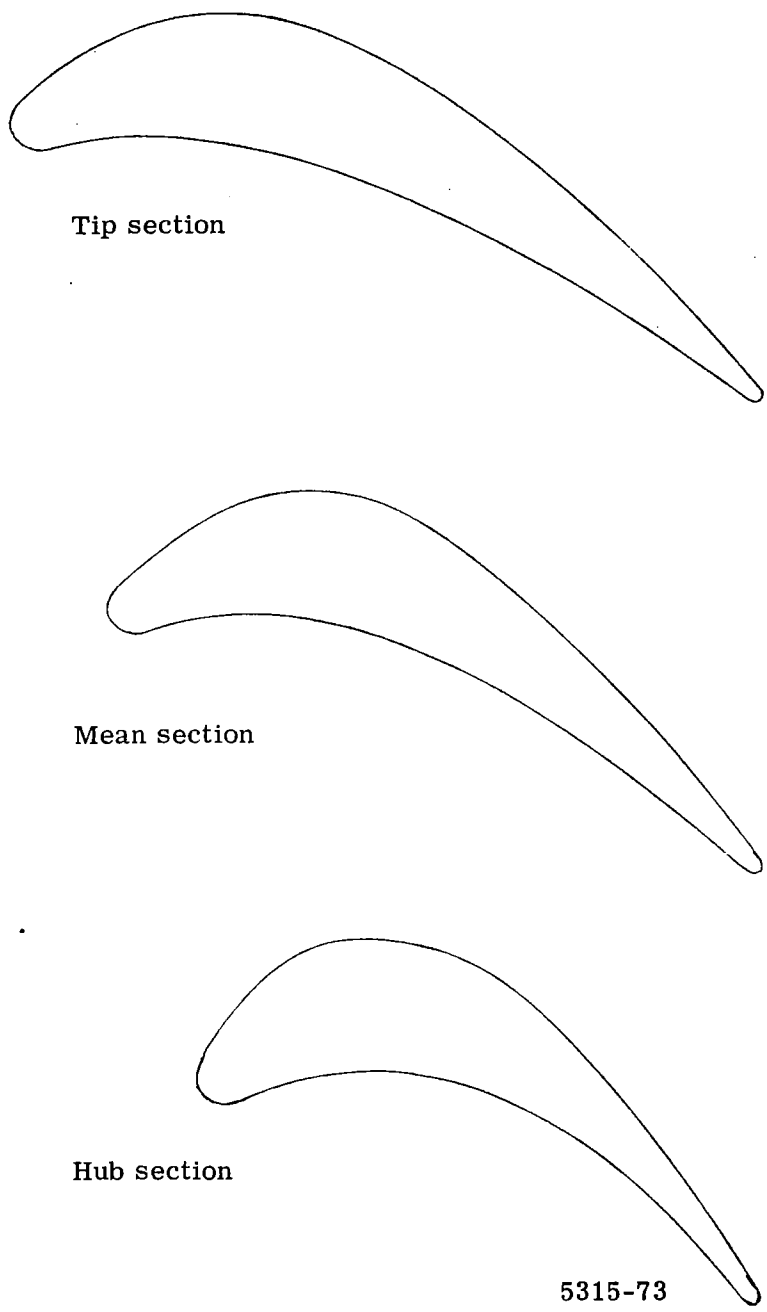

Figure 6. Plain stator blade profiles.
See Table II.

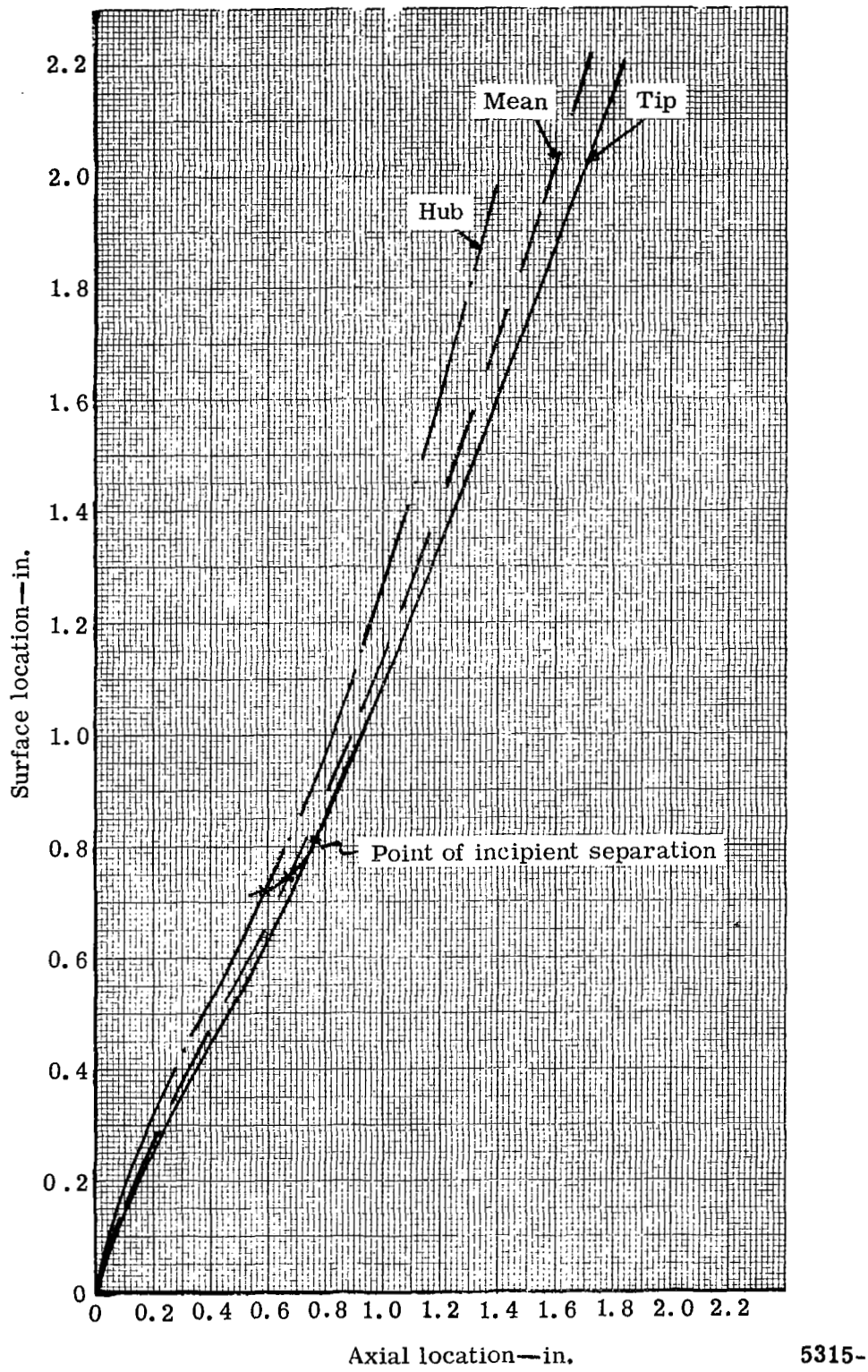

Figure 7. Axial versus surface location for plain blade.

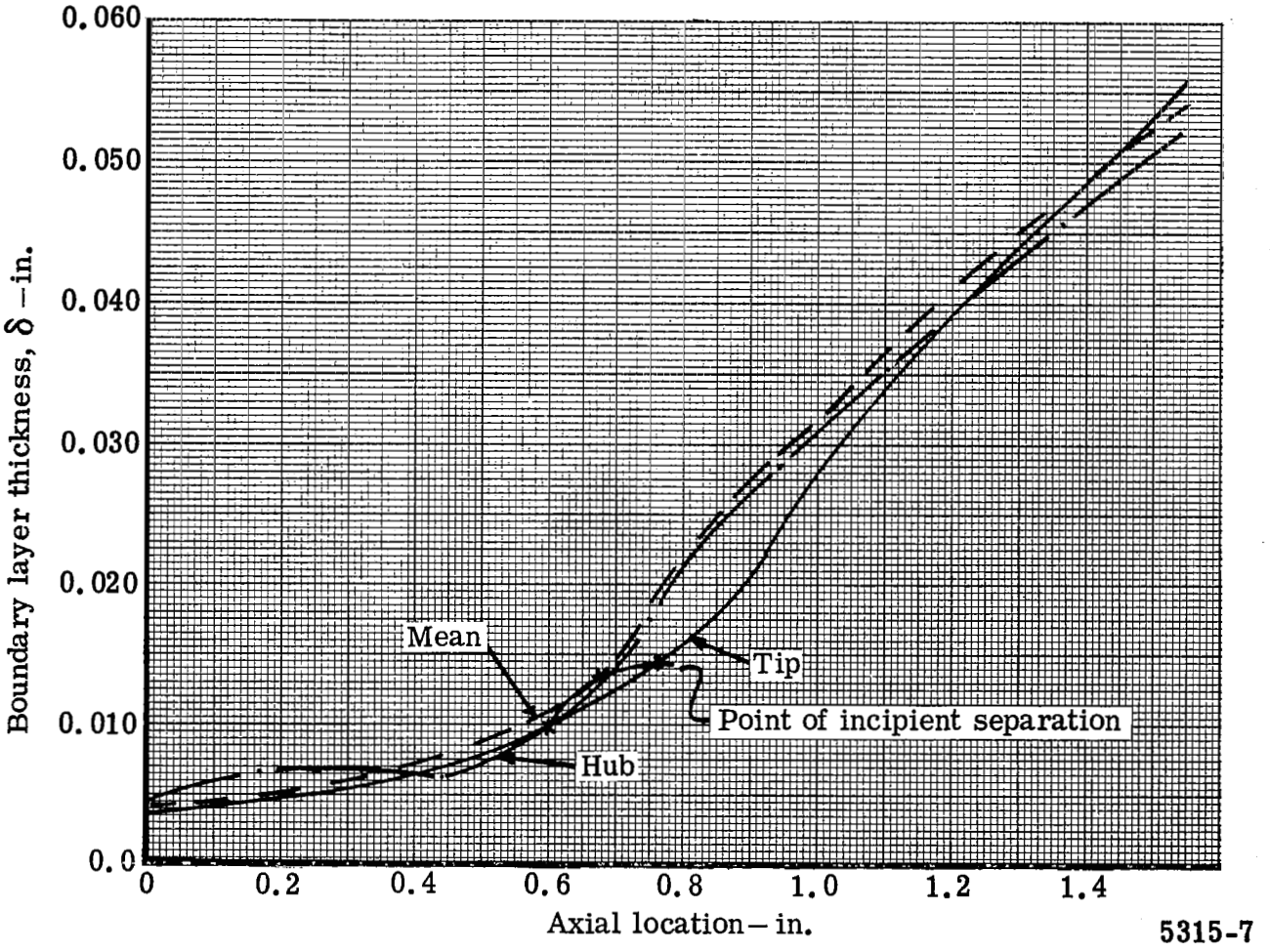

Figure 8. Axial variation of boundary layer thickness on plain blade.

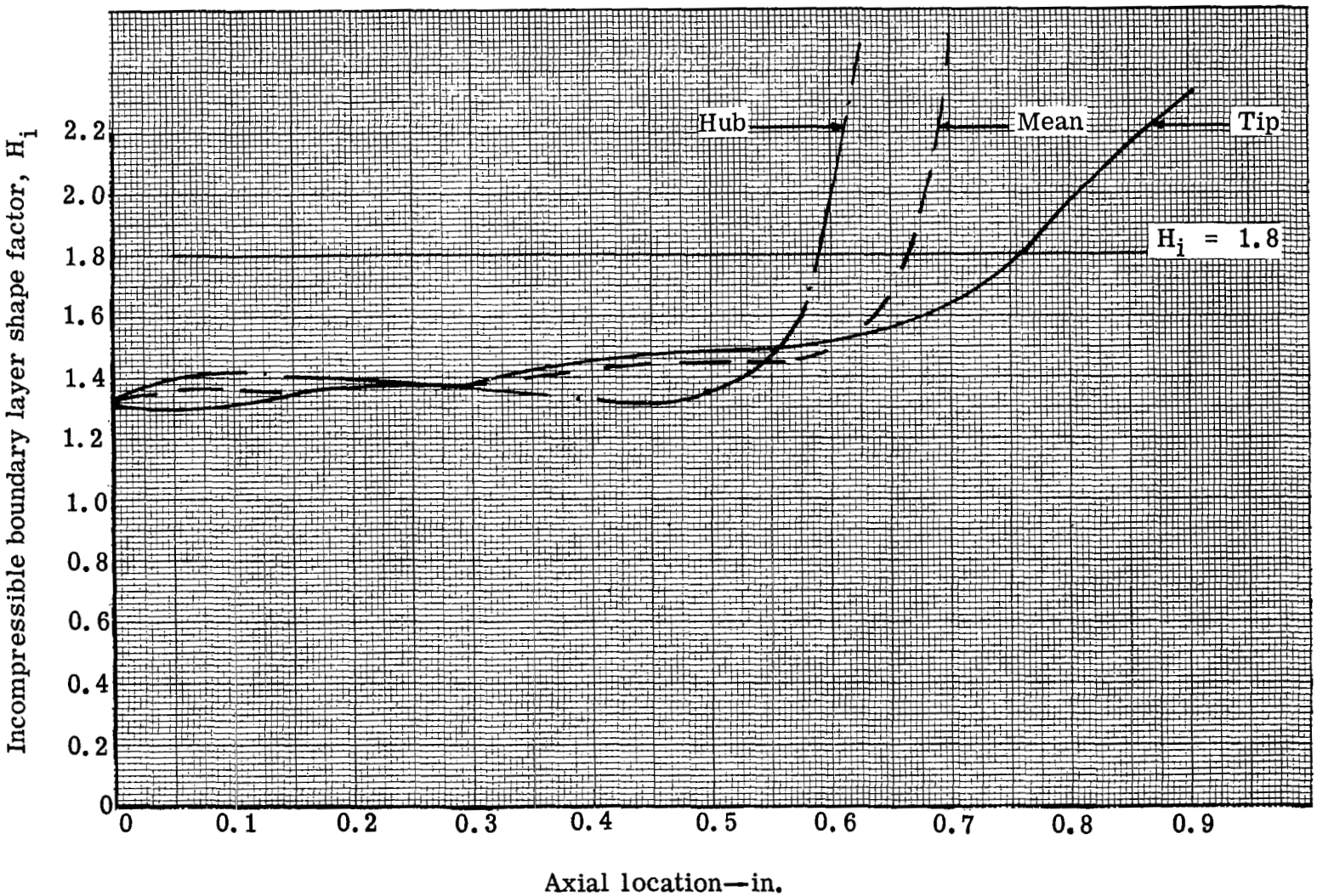

Figure 9. Plain blade suction surface incompressible boundary layer shape factor.

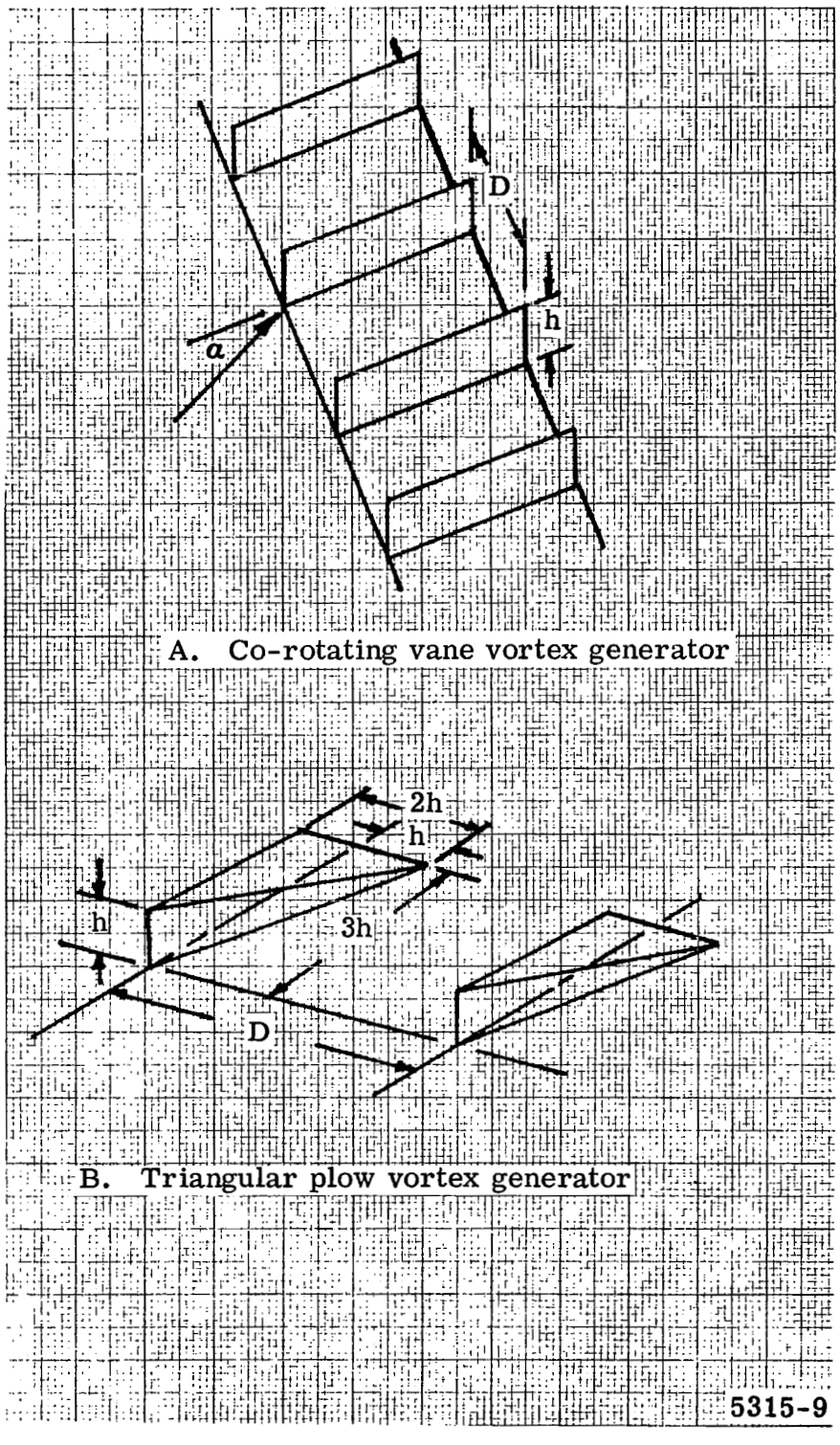

Figure 10. Types of vortex generators mounted on plain blade configuration.

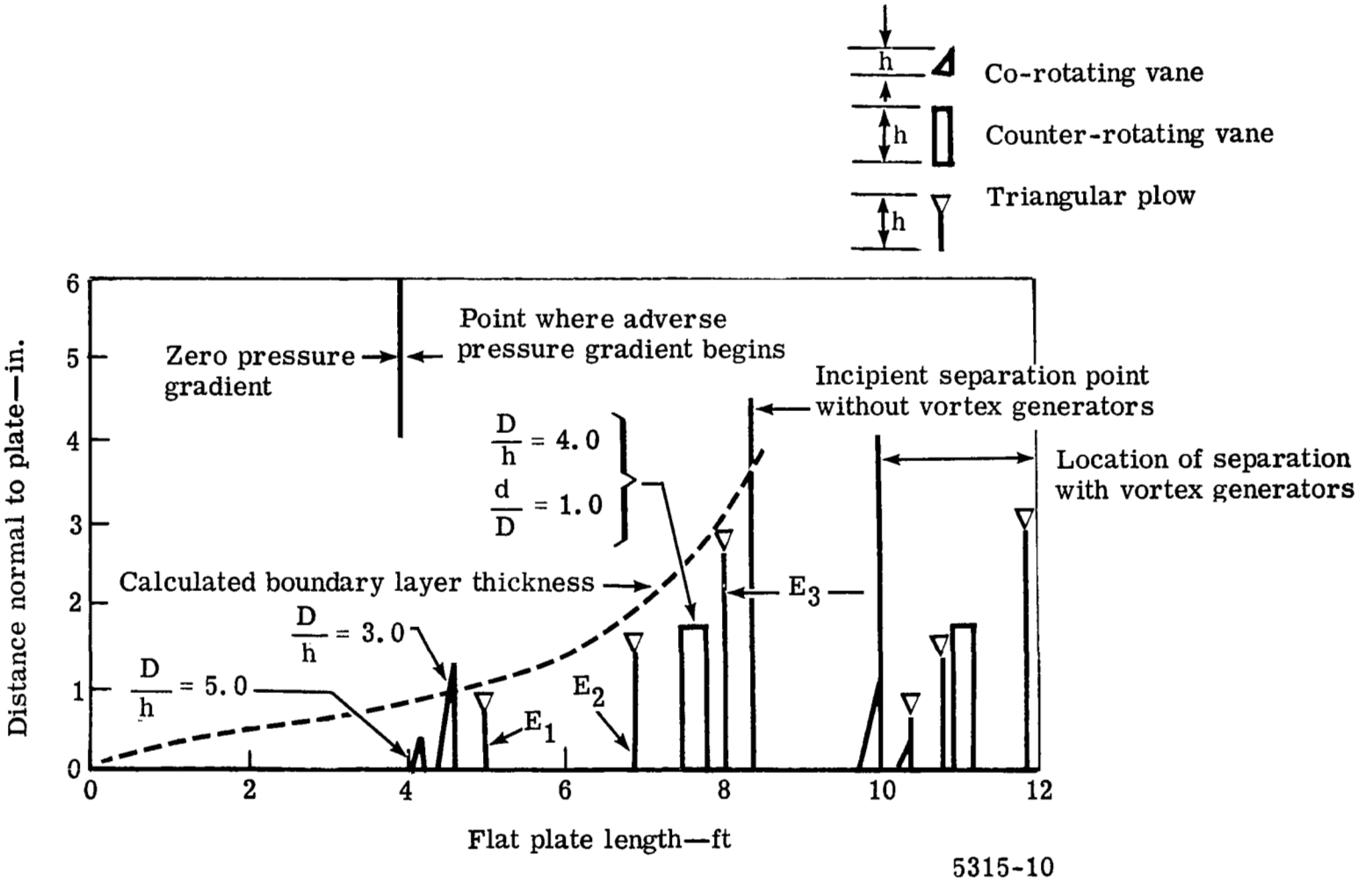

Figure 11. Comparison of vortex generator range (from reference 5). (See Table X)

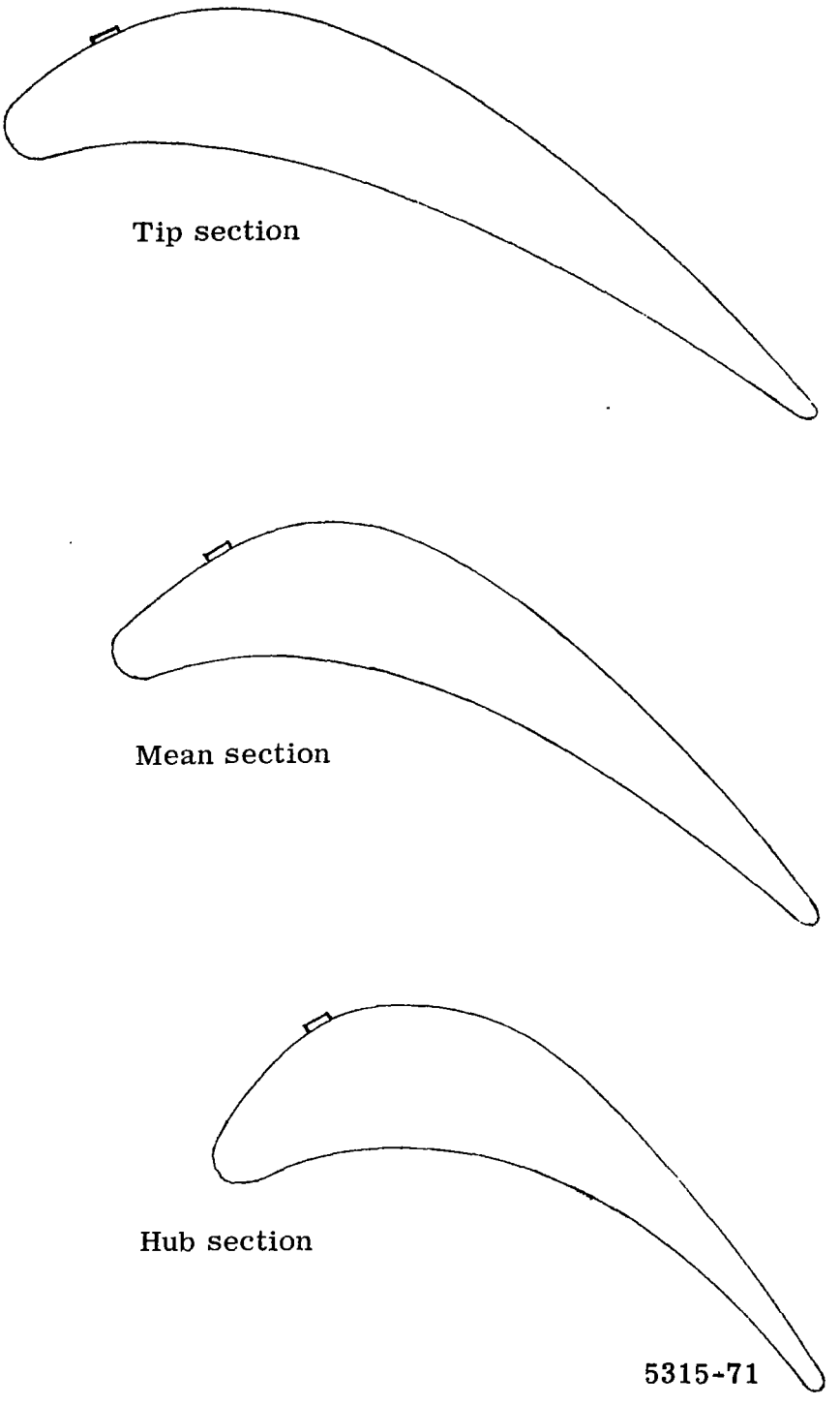

Figure 12. Plain blade configuration fitted with co-rotating vane vortex generator. See Table V.

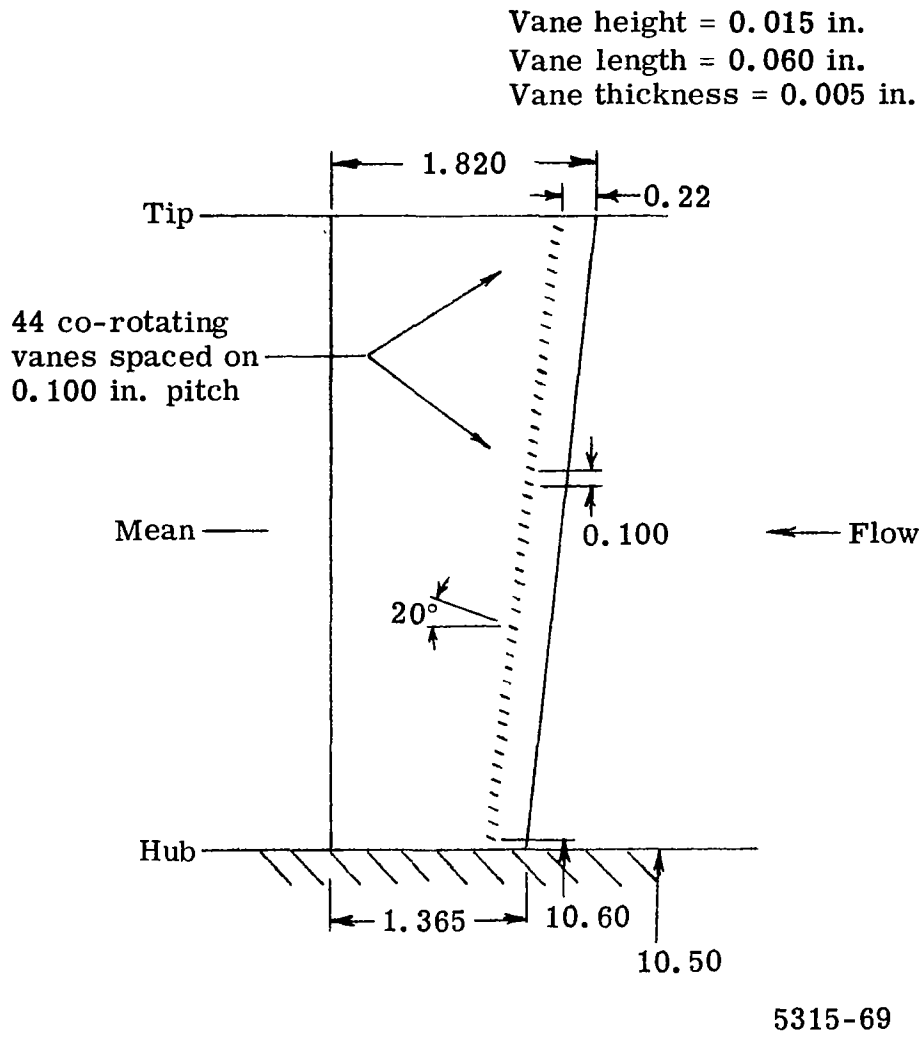

Figure 13. Plain blade configuration fitted with co-rotating vane vortex generator.

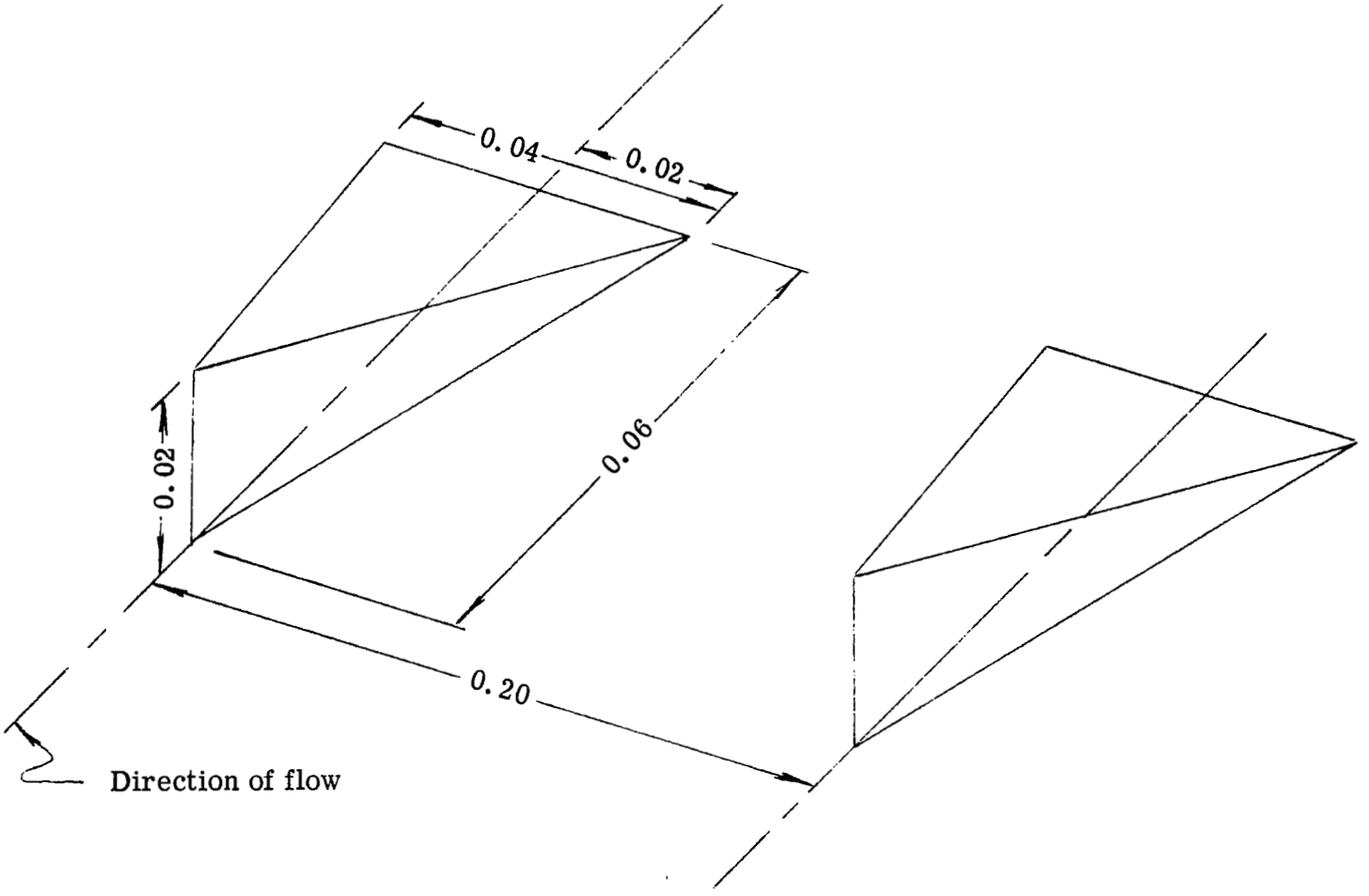

Figure 14. Triangular plow configuration.

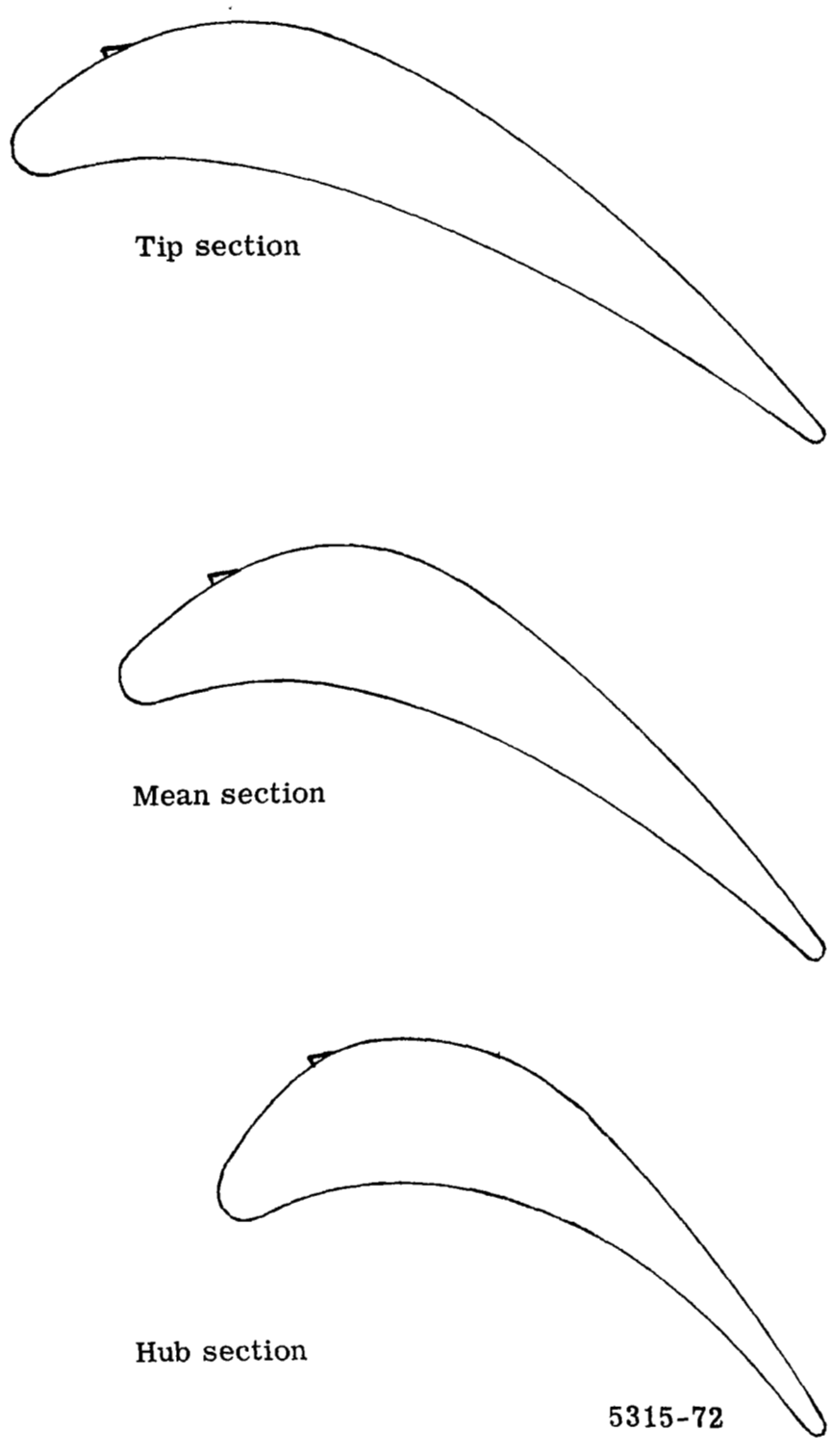

Figure 15. Plain blade configuration fitted with triangular plow vortex generator. See Table VI.

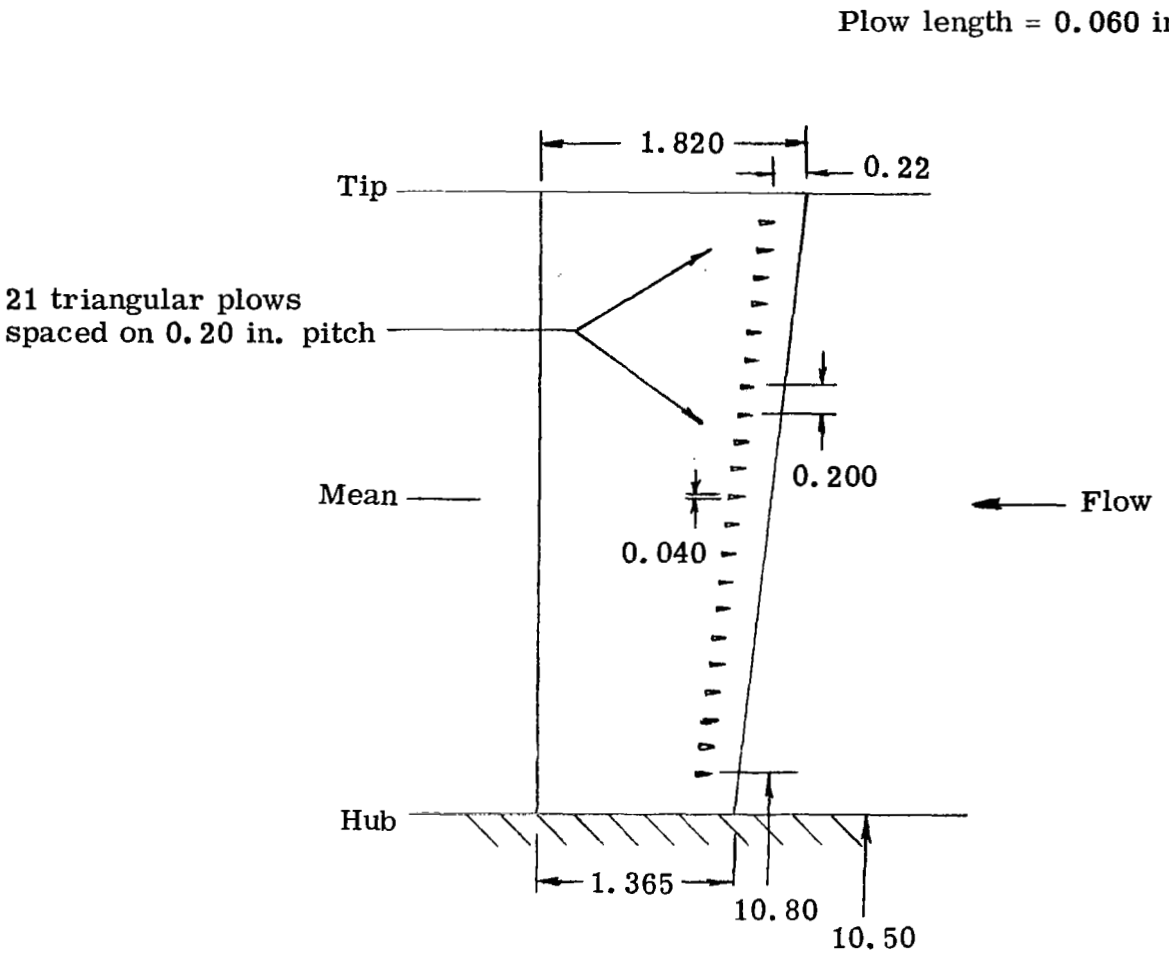

Figure 16. Plain blade configuration fitted with counter-rotating triangular plow vortex generator.

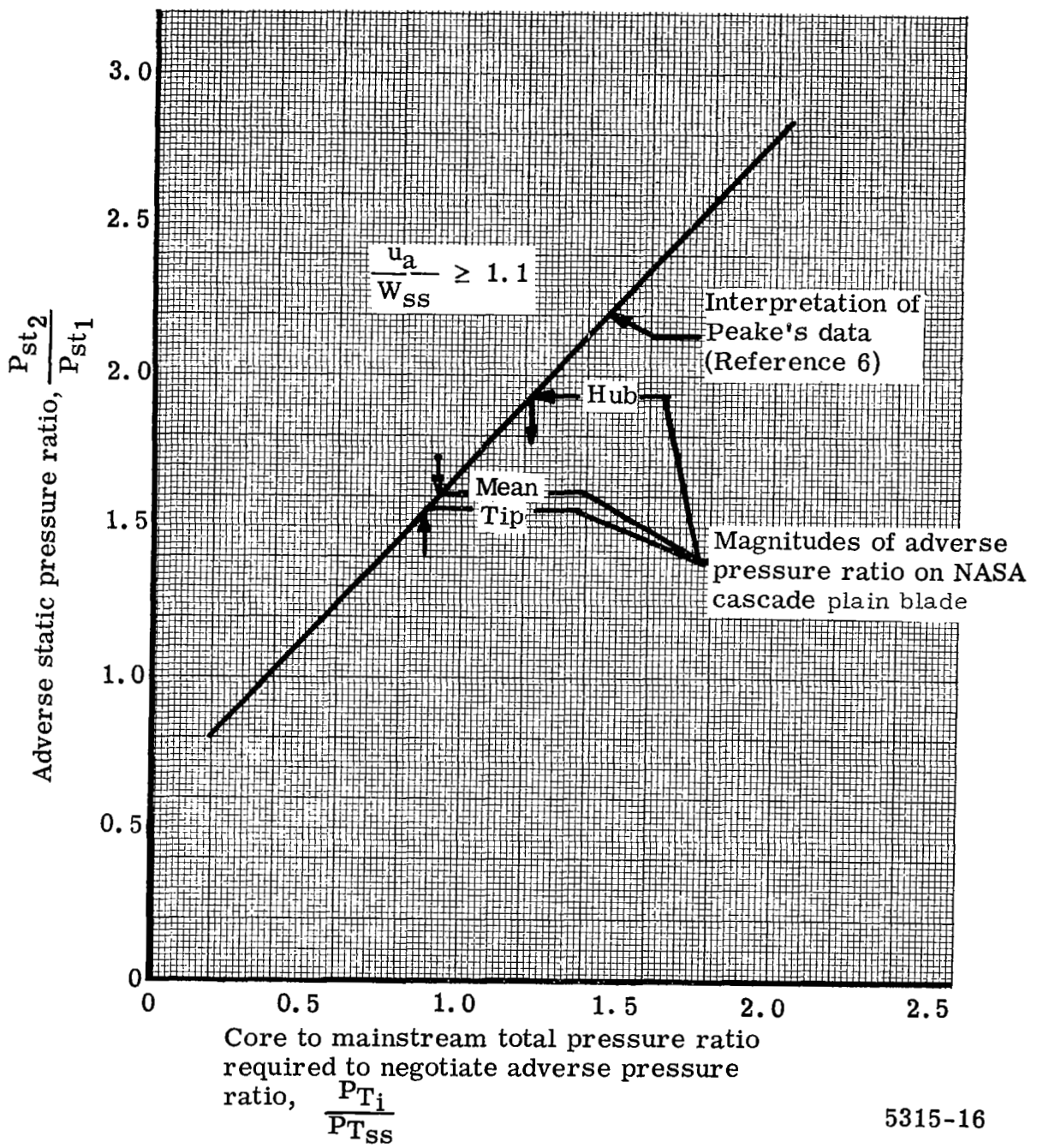

Figure 17. Adverse static pressure ratio correlation for one injection slot, interpreted from D. J. Peake's (reference 6) data.

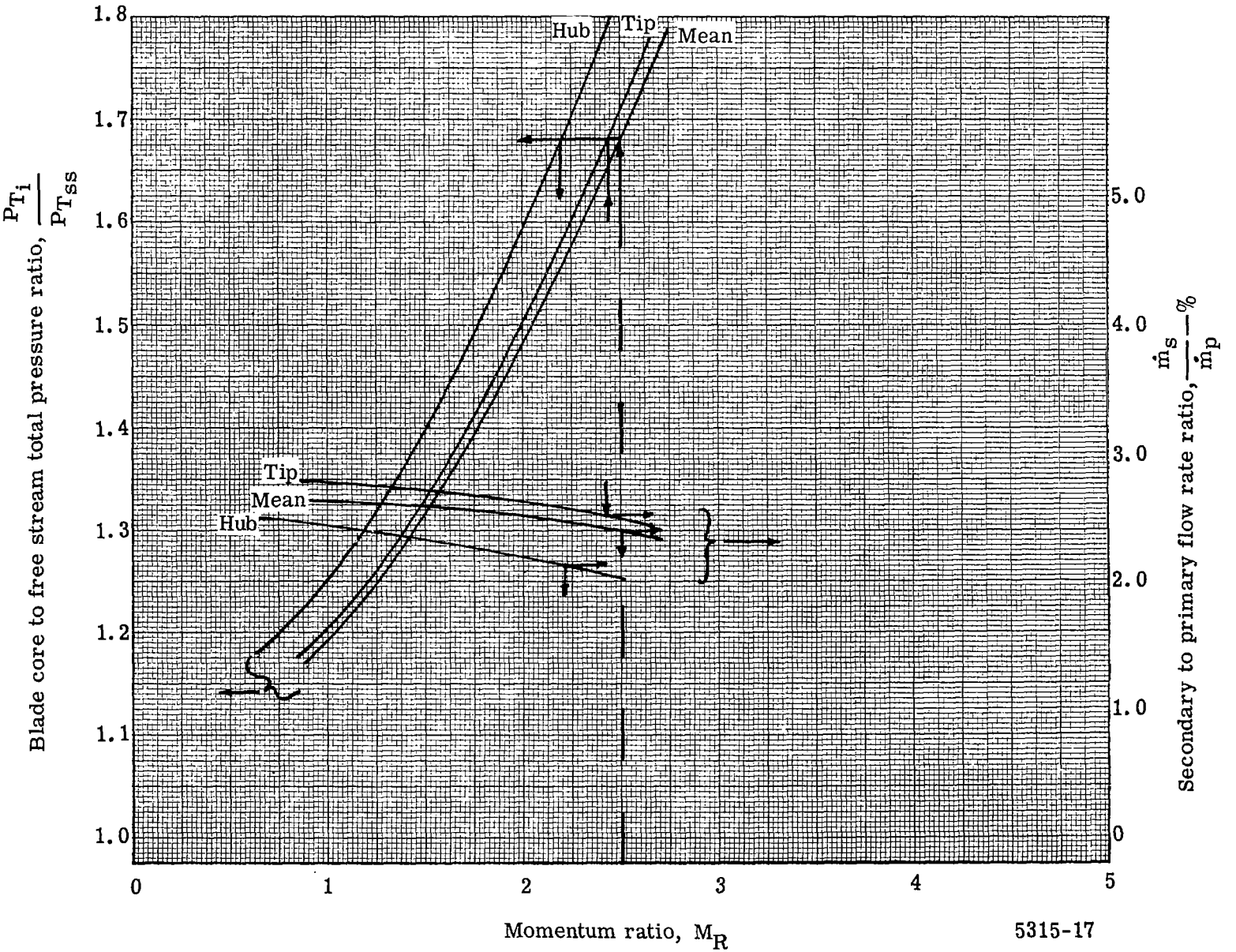

Figure 18. Tangential jet slot No. 1 parameters for hb = 0.020 in.

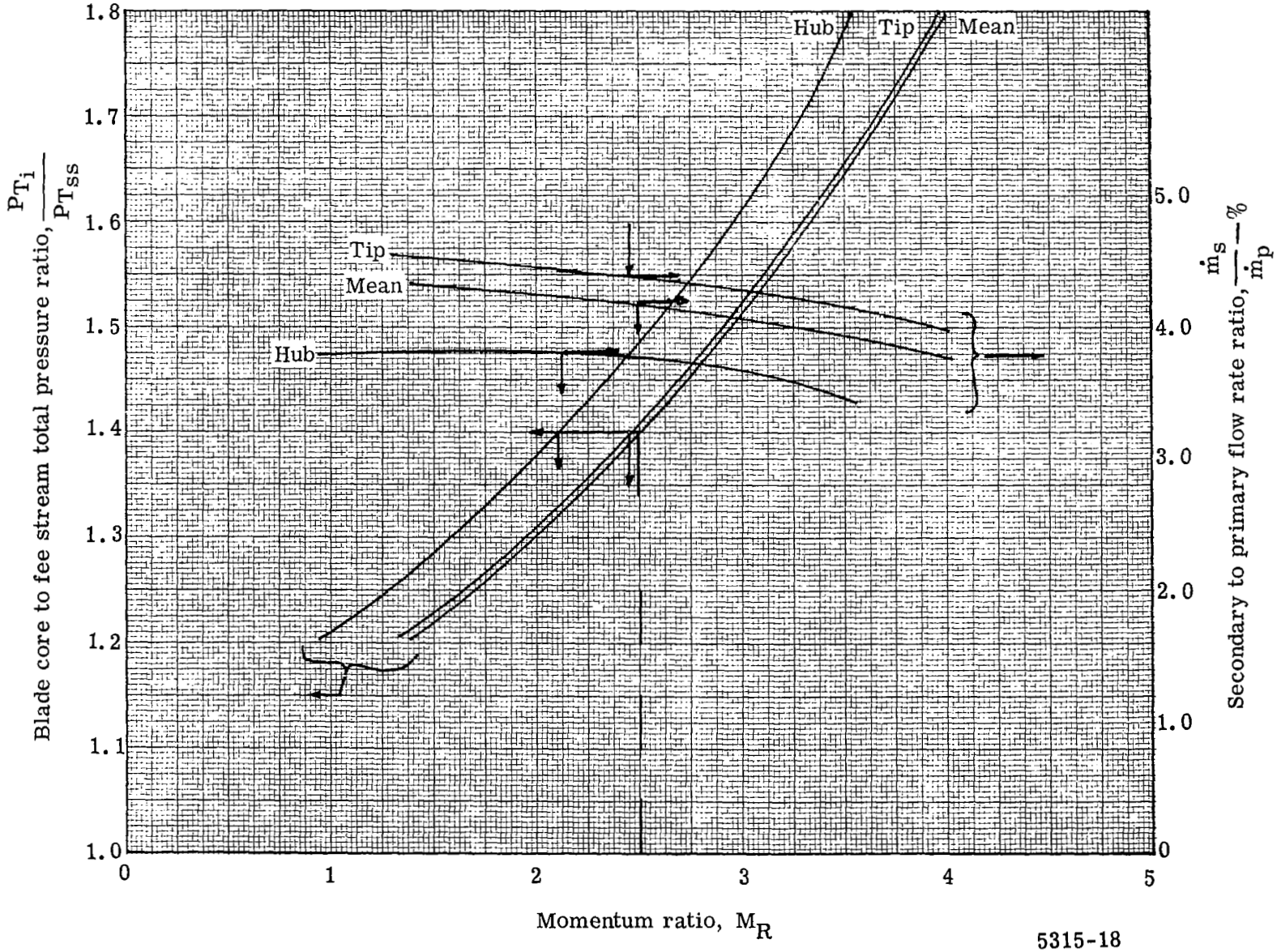

Figure 19. Tangential jet slot No. 1 parameters for hb = 0.030 in.

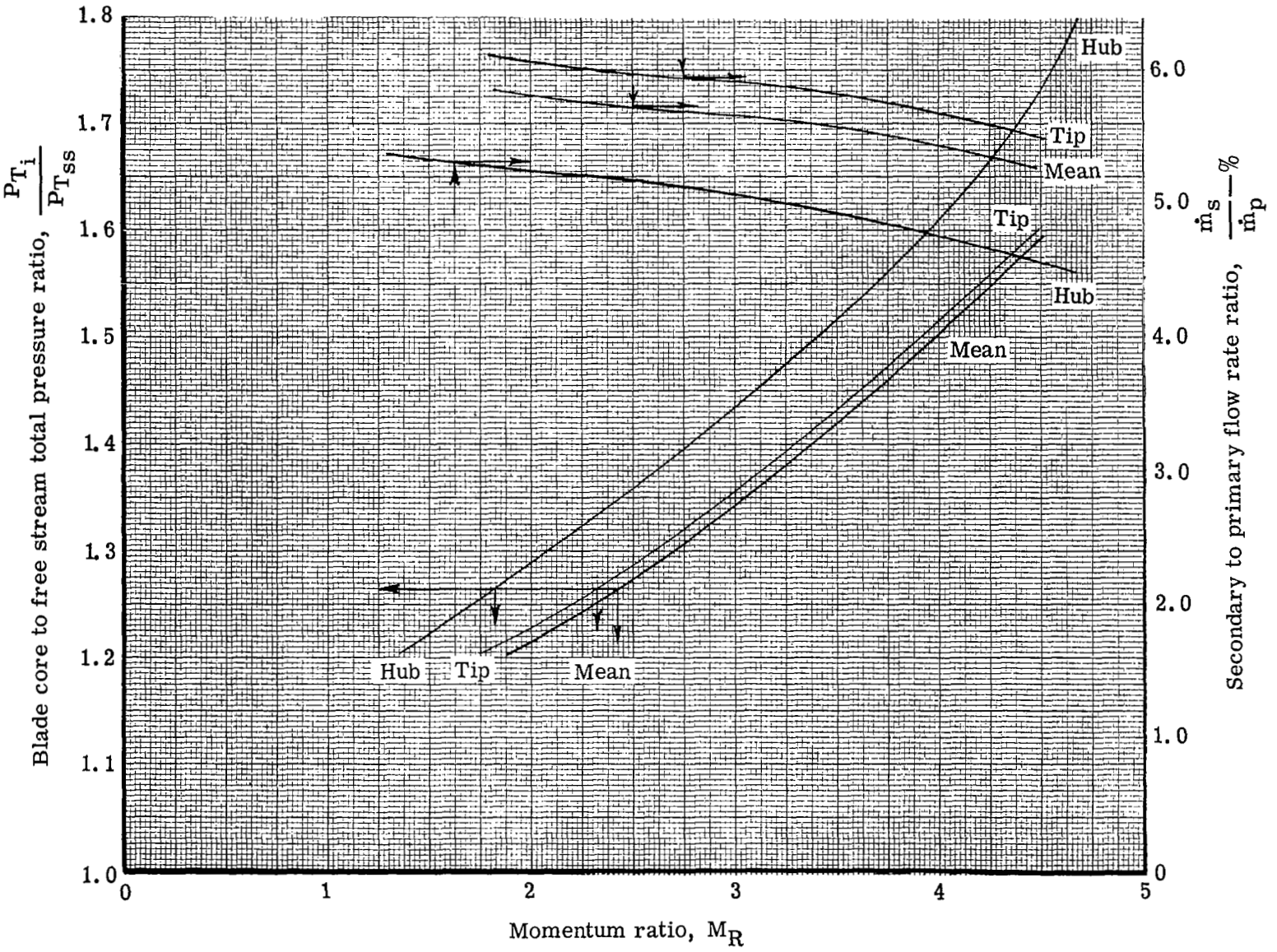

Figure 20. Tangential jet slot No. 1 parameters for hb = 0.040 in.

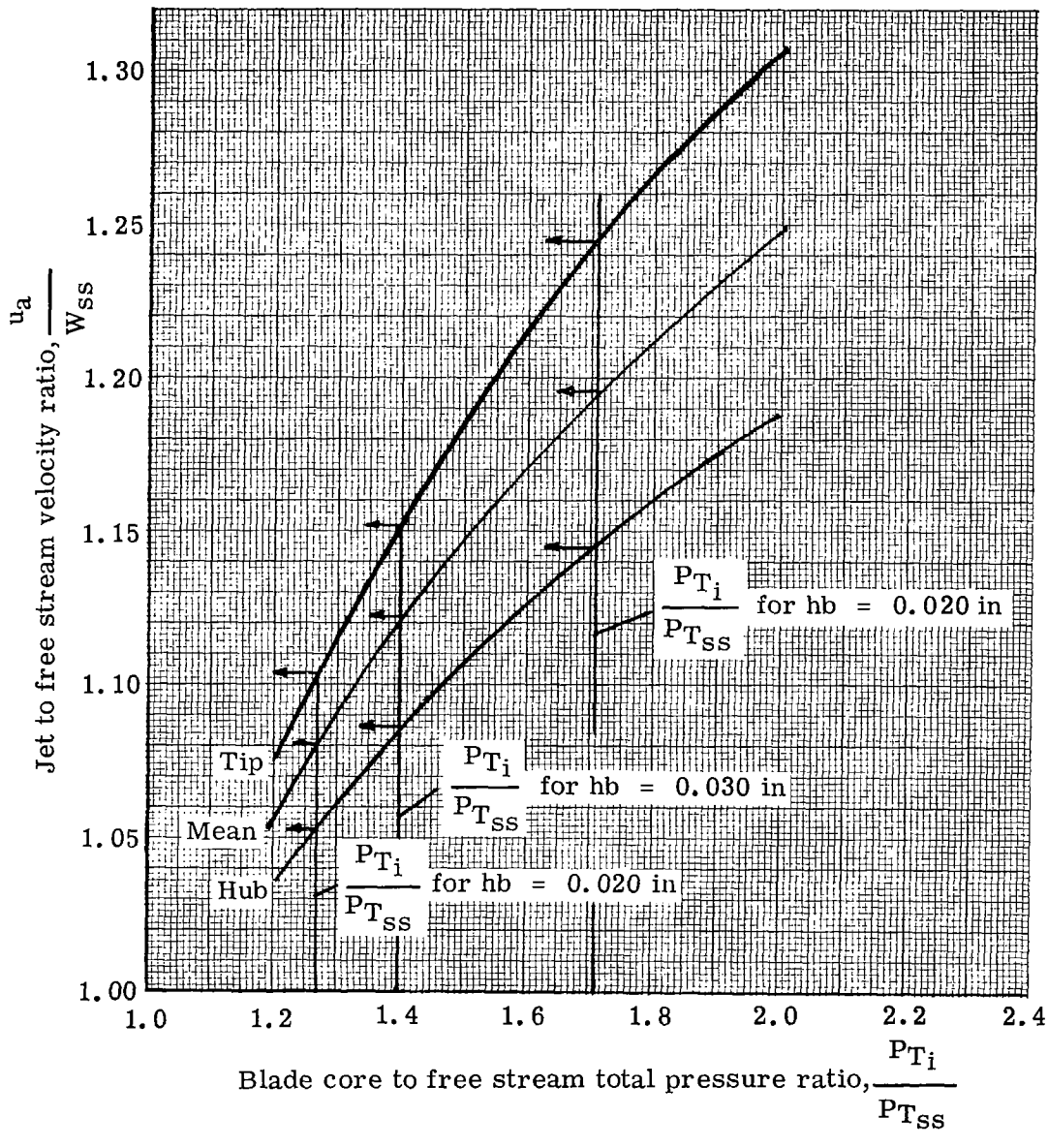

Figure 21. Jet to mainstream velocity ratio vs ($P_{T_i}/P_{T_{ss}}$) for tangential jet slot No. 1.

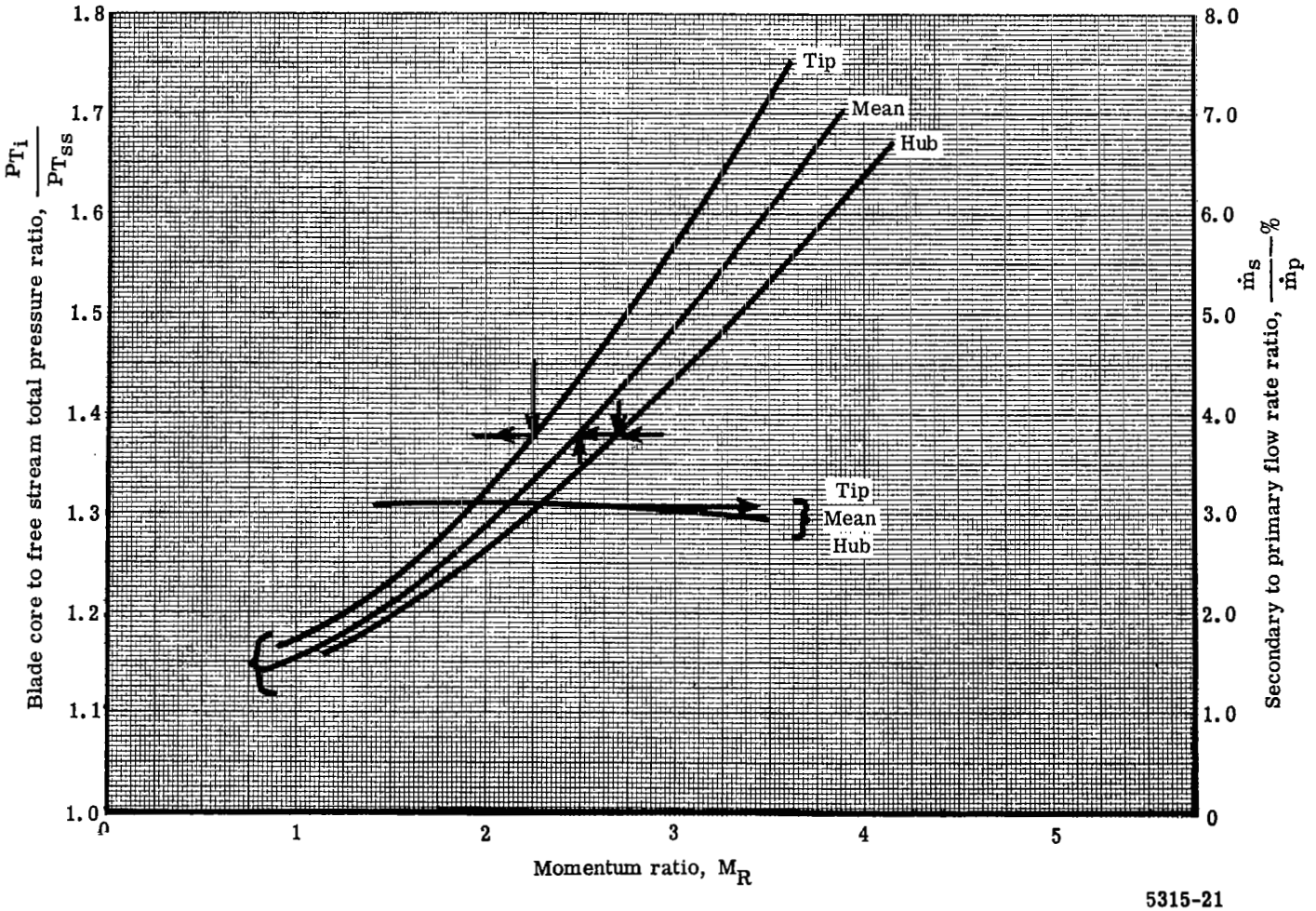

Figure 22. Tangential jet slot No. 2 parameters for hb = 0.020 in.

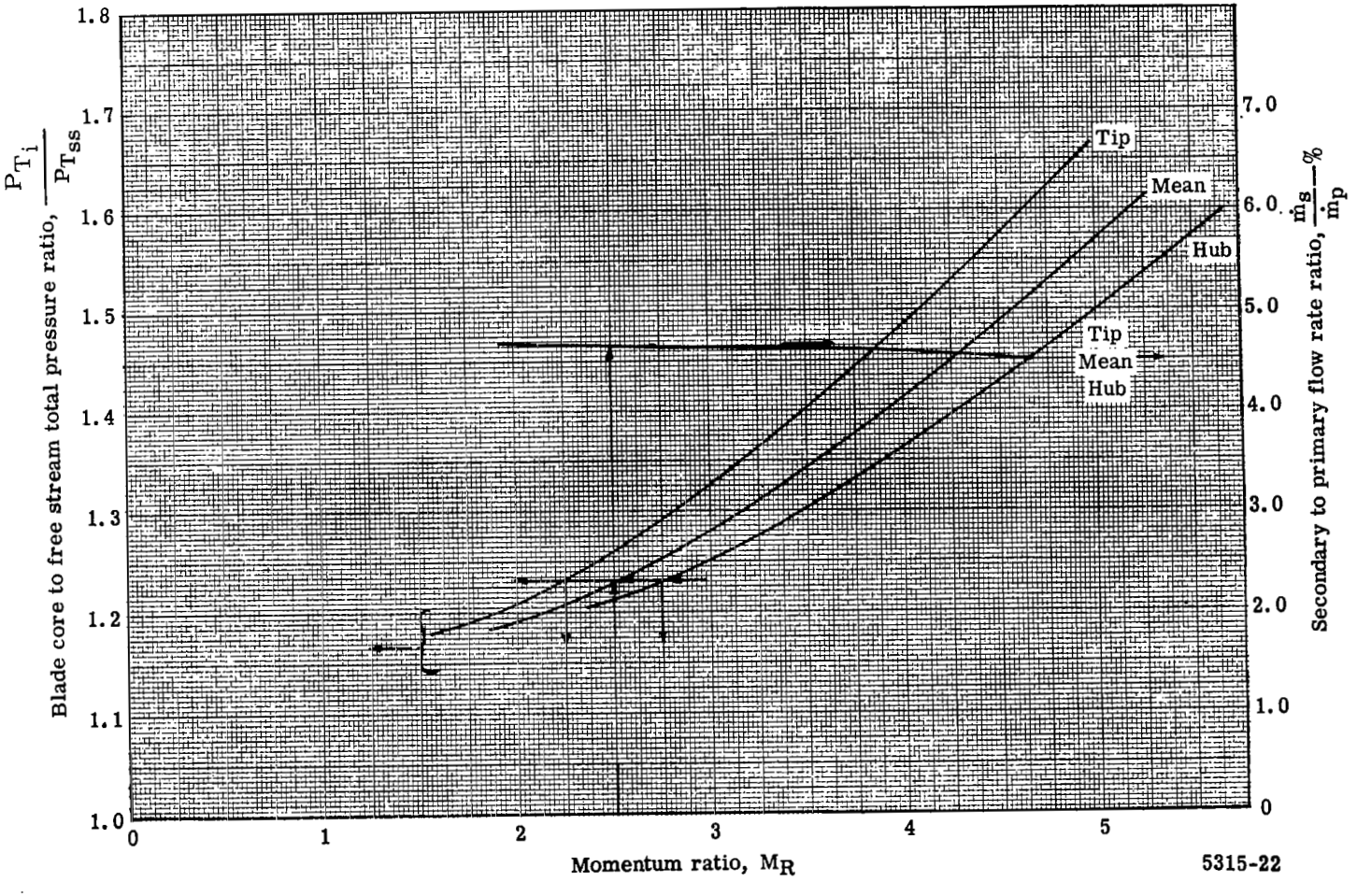

Figure 23. Tangential jet slot No. 2 parameters for hb = 0.030 in.

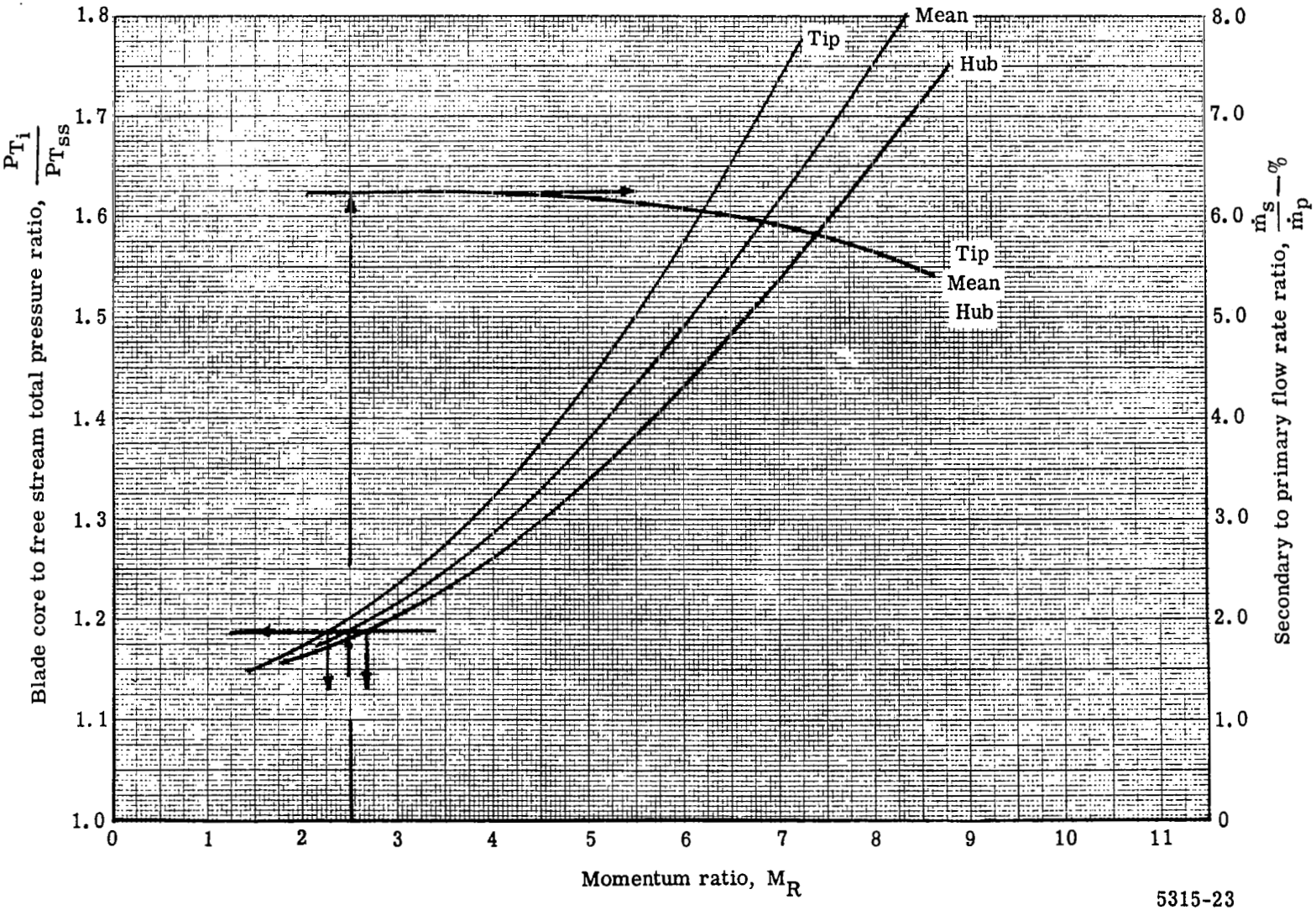

Figure 24. Tangential jet slot No. 2 parameters for hb = 0.040 in.

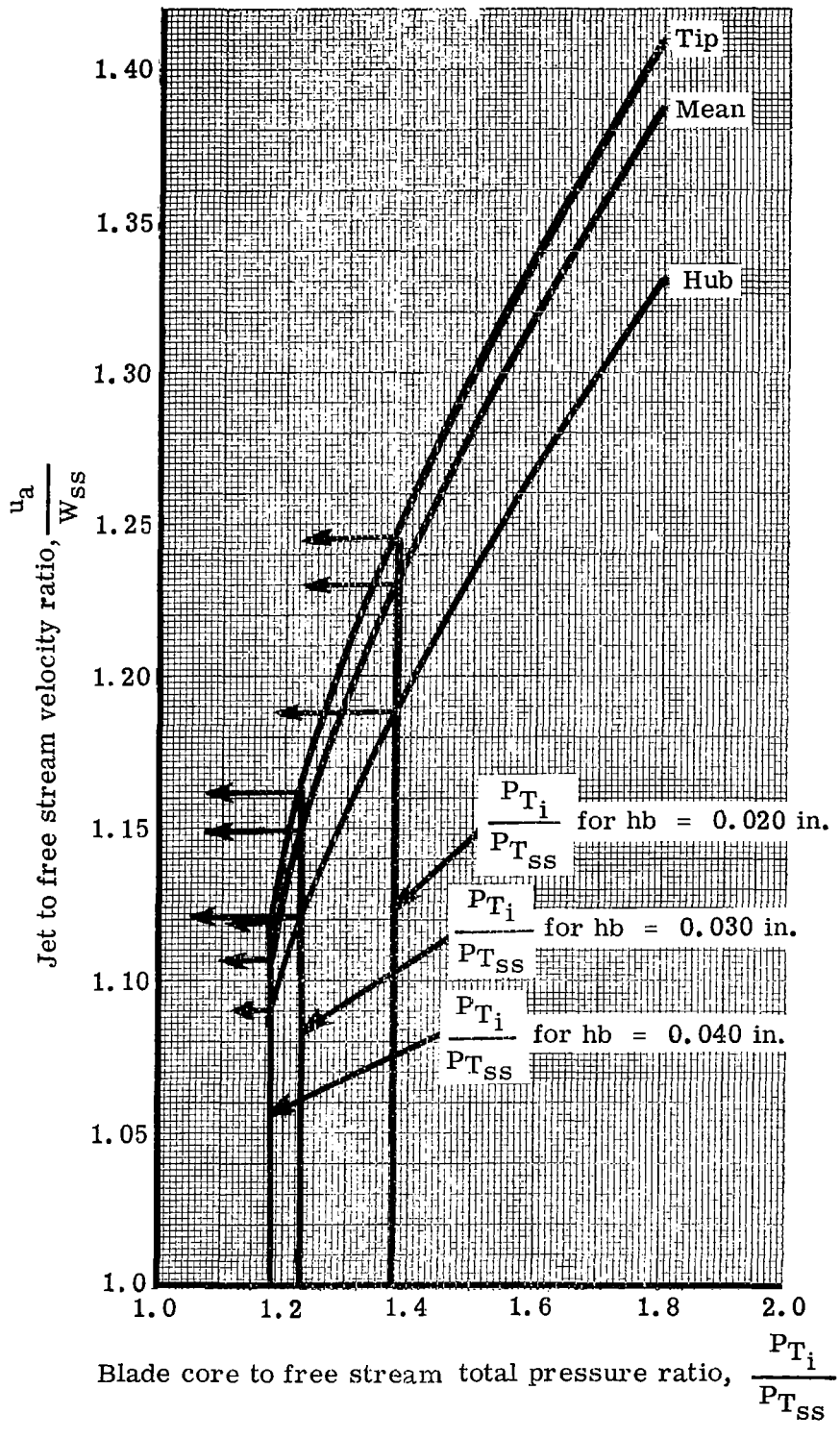

Figure 25. Jet to mainstream velocity ratio vs ($P_{T_i} / P_{T_{ss}}$) for tangential jet slot No. 2.

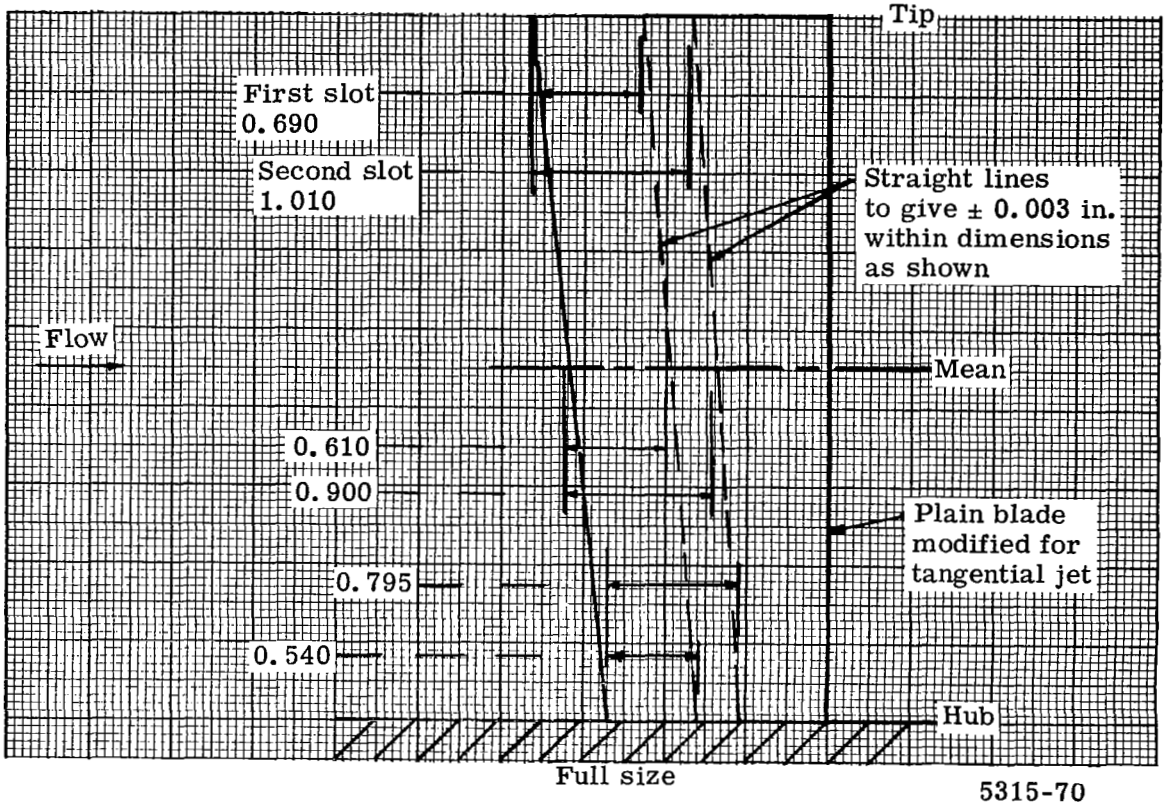

Figure 26. Slot location dimensions for tangential jet flowing blades.

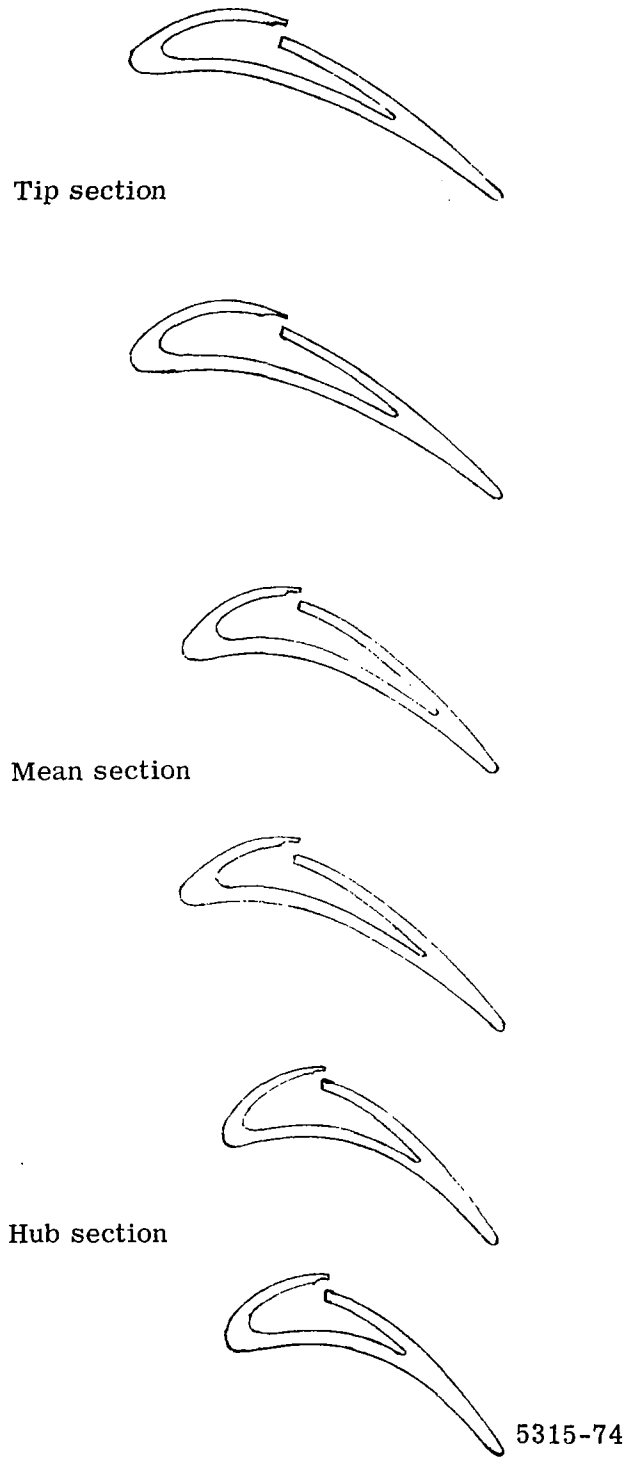

Figure 27. Tangential jet blowing slot location 1 blade profiles and passages. See Tables VII, VIII, XI, and XII.

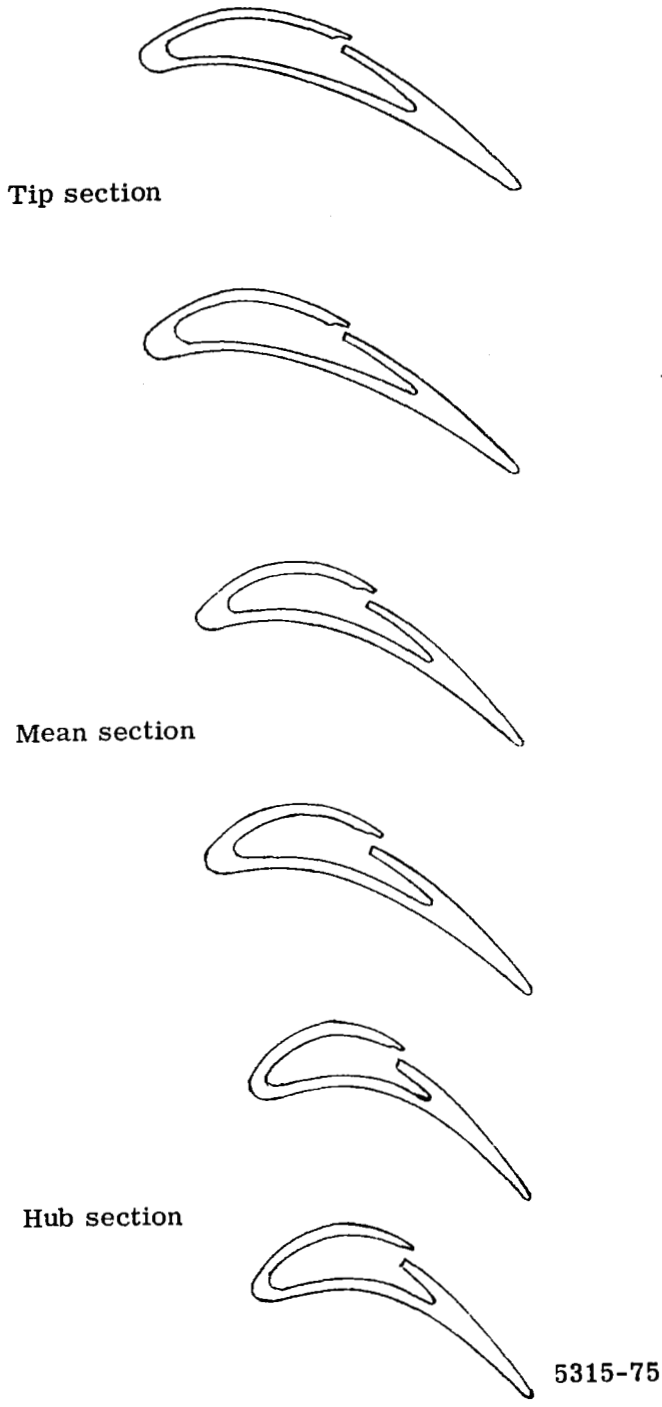

Figure 28. Tangential jet blowing slot location 2 blade profiles and passages. See Tables IX, X, XI, and XII.

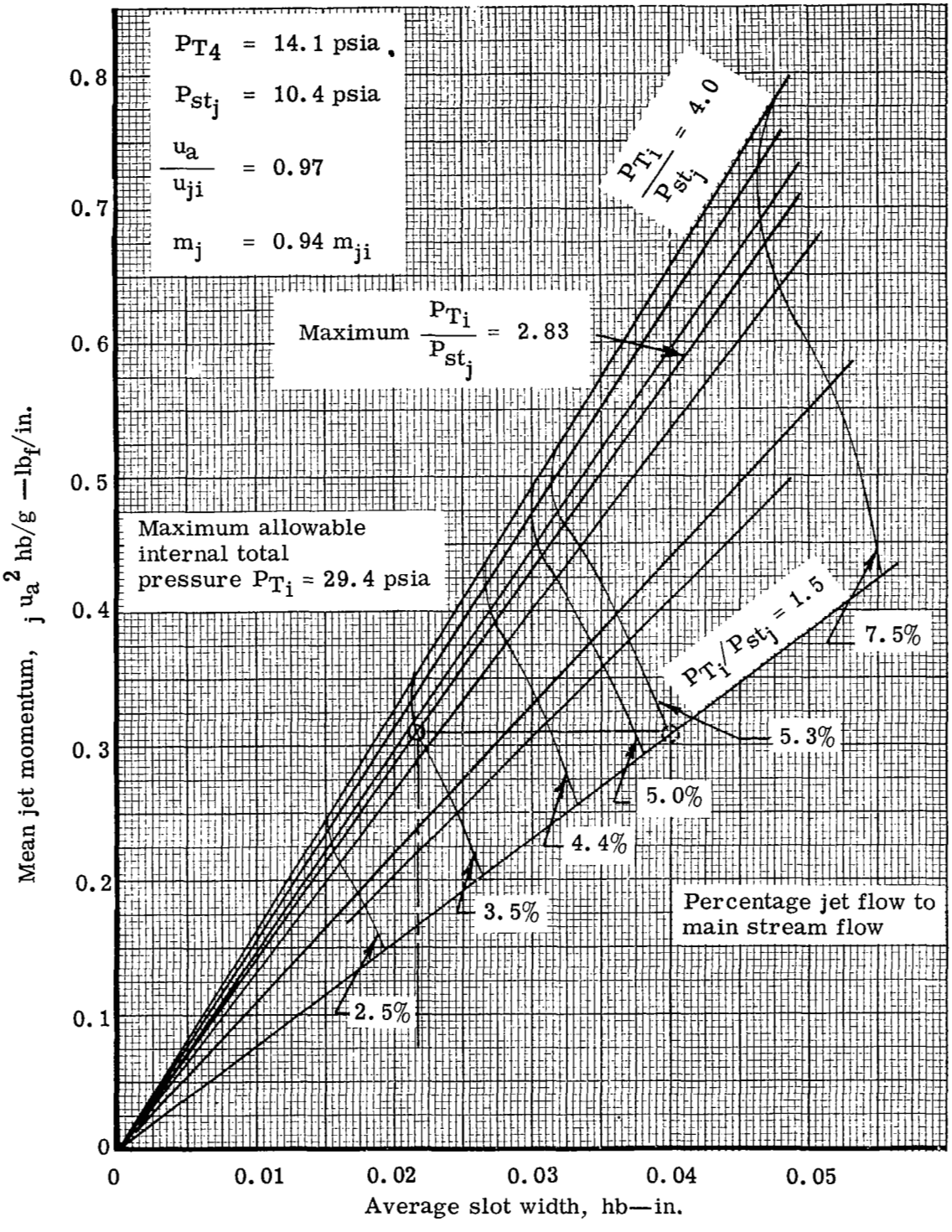

5315-28

Figure 29. Variation of average jet momentum with average slot width and secondary air pressure.

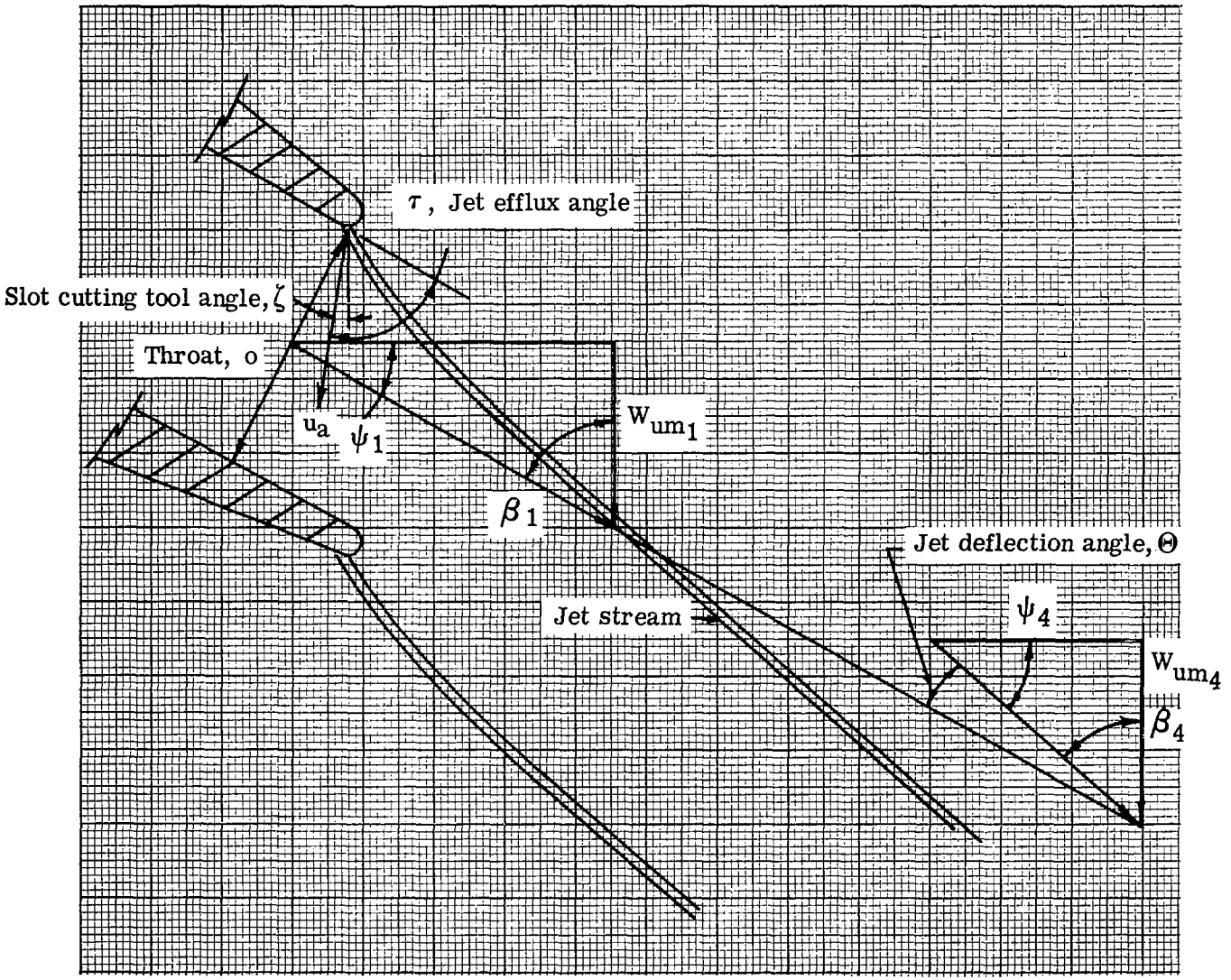

Figure 30. Jet-flapped blade nomenclature.

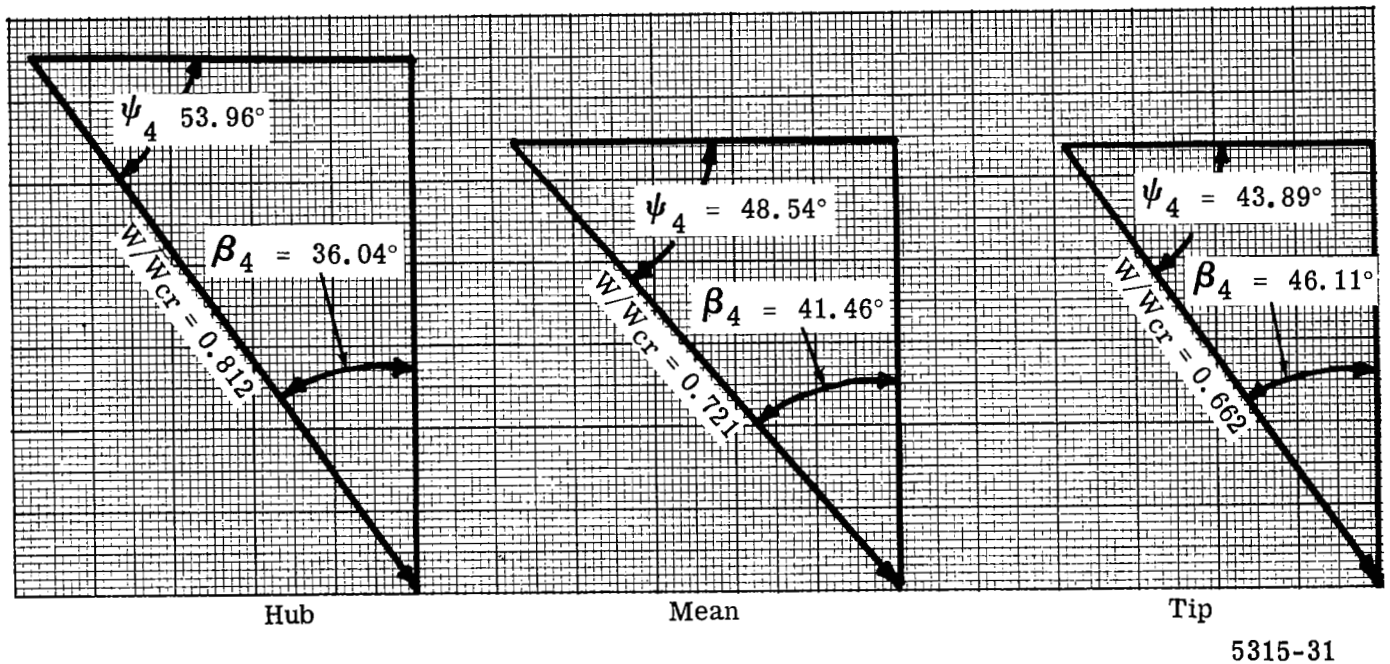

Figure 31. Jet-flapped blade downstream velocity triangles with 4.4% jet flow.

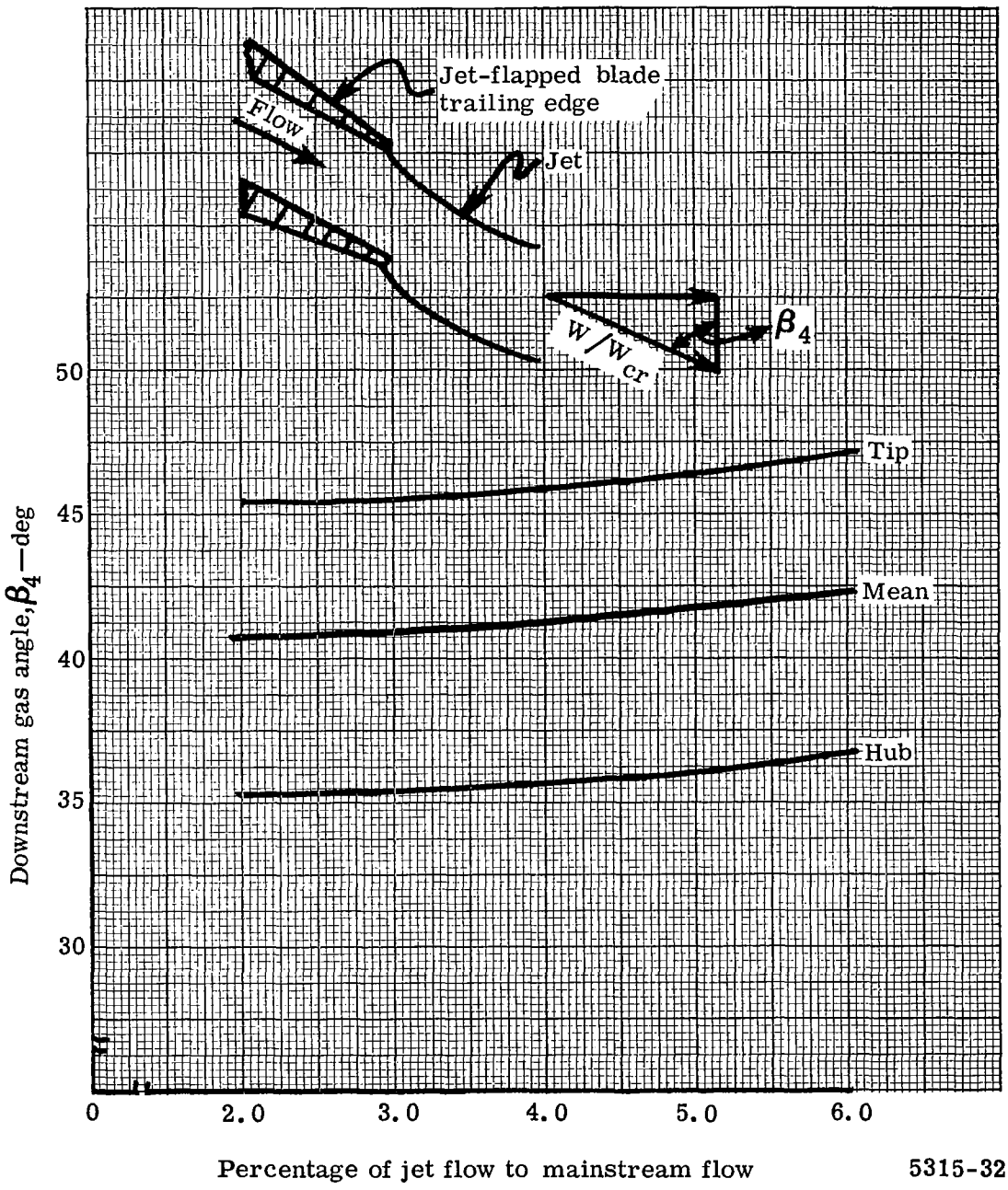

Figure 32. Variation of downstream gas angle as a function of percentage of jet to mainstream flow.

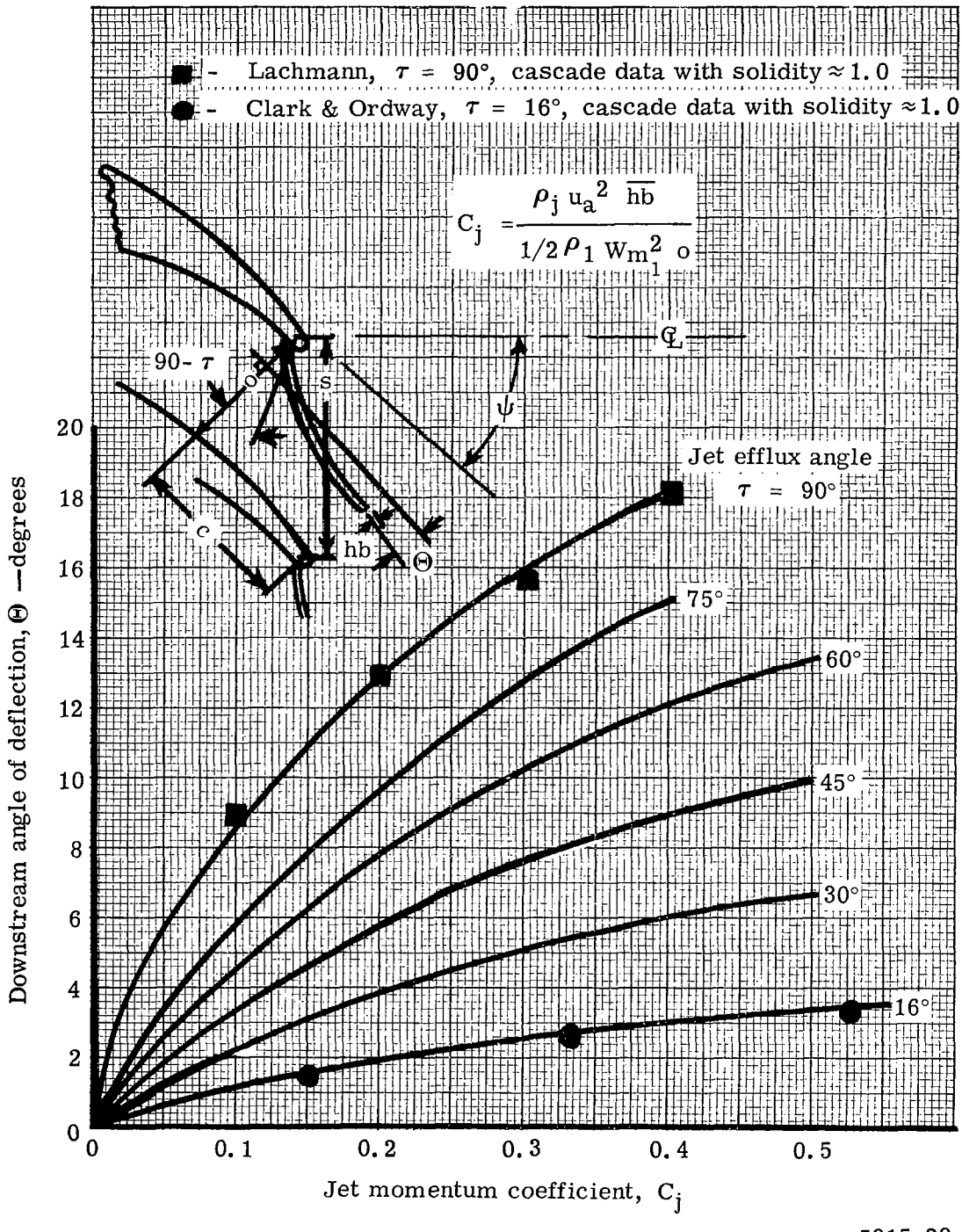

5315-29

Figure 33. Variation of primary stream deflection with jet momentum coefficient and jet efflux angle.

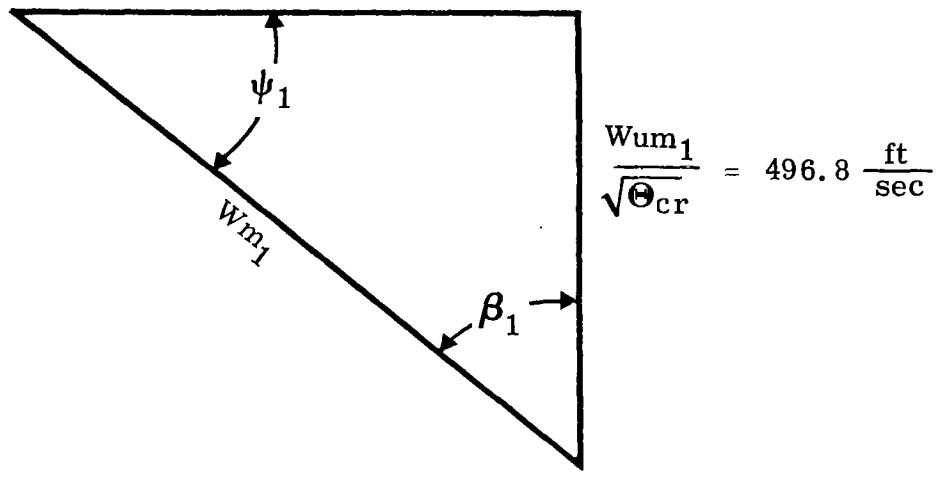

Figure 34. Jet-flapped blade midchannel mean section throat velocity triangle.

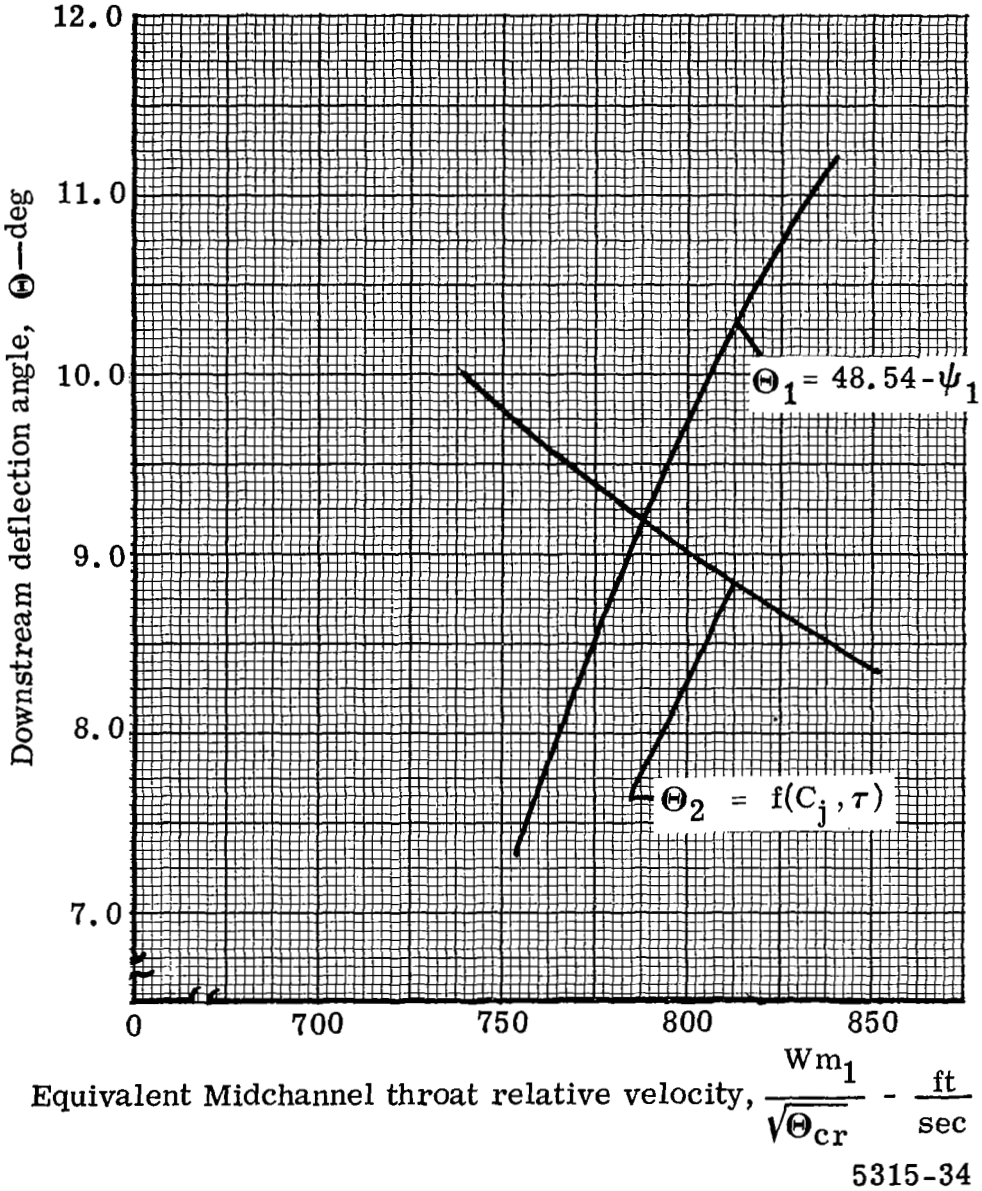

Figure 35. Jet-flapped blade graphical solution of jet deflection angle at the mean section.

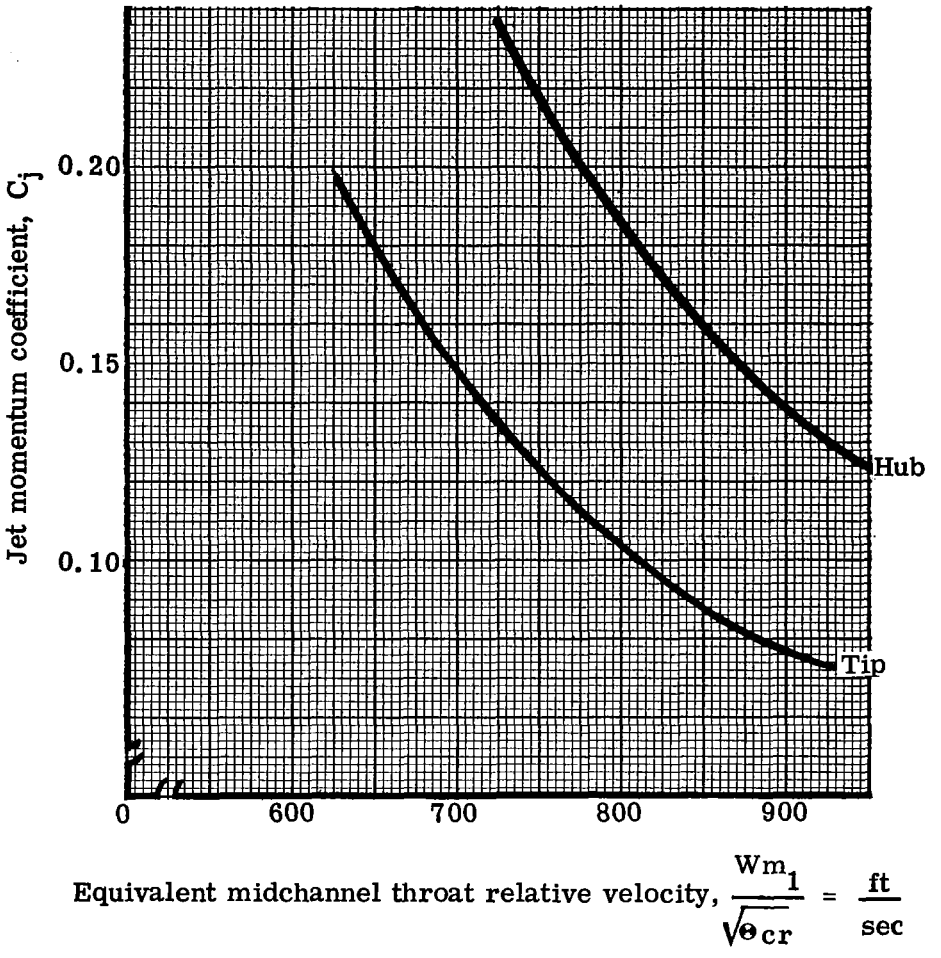

Figure 36. Jet-flapped blade variation of hub and tip midchannel throat relative velocities as a function of jet momentum coefficient.

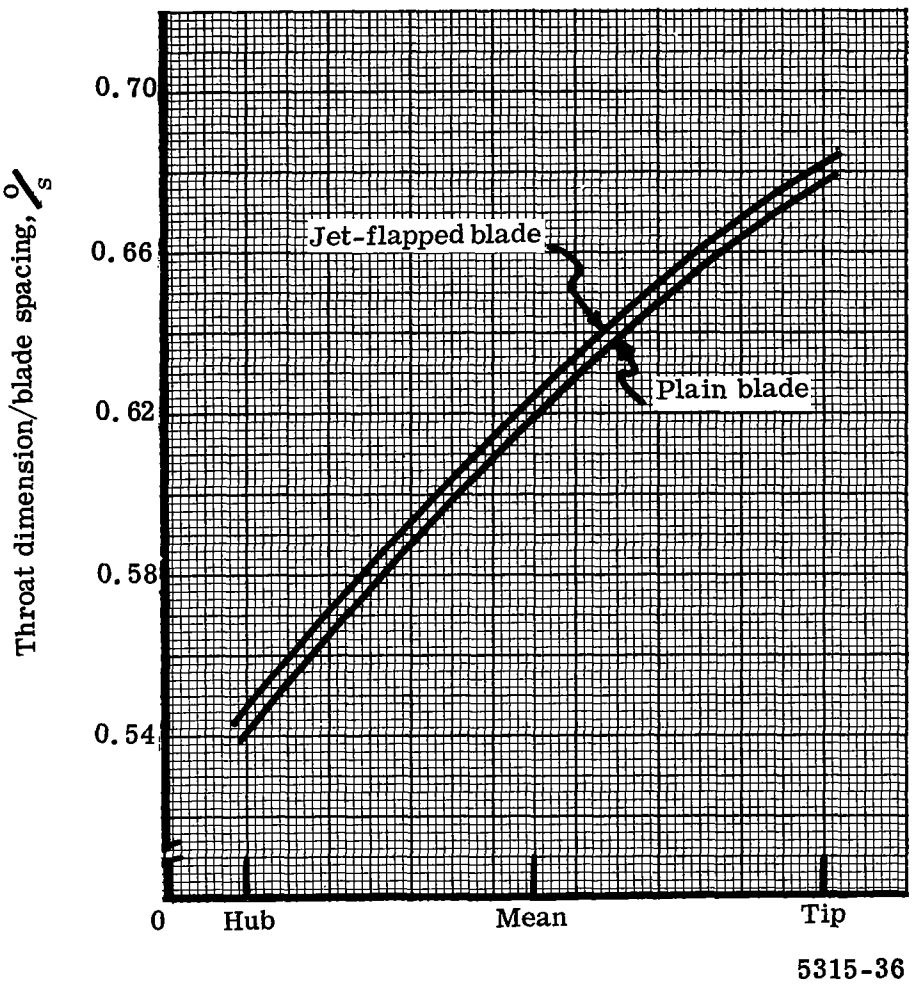

Figure 37. Jet-flapped blade radial variation of throat dimension to blade spacing ratio.

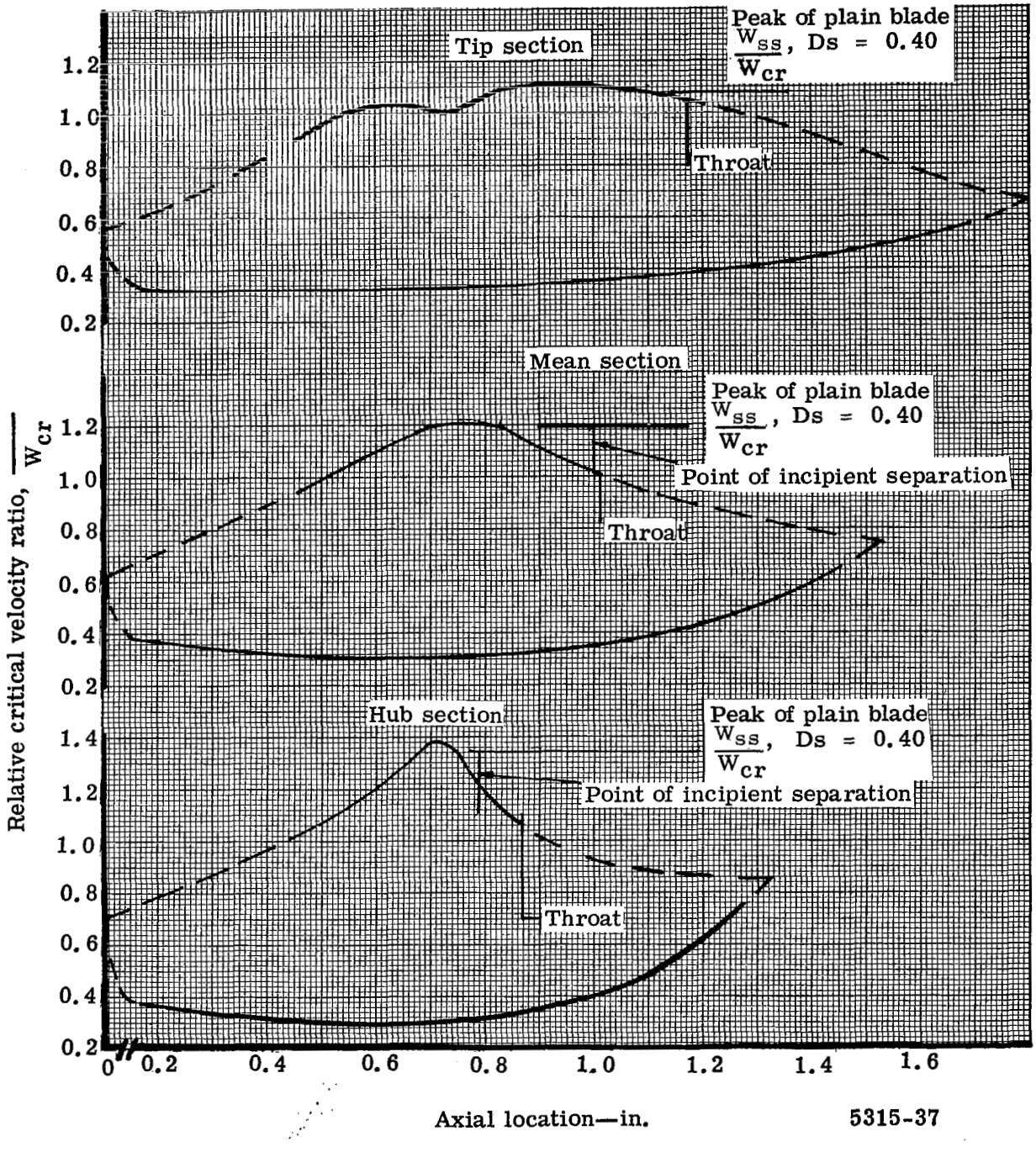

Figure 38. Jet-flapped blade critical velocity distribution without jet flap.

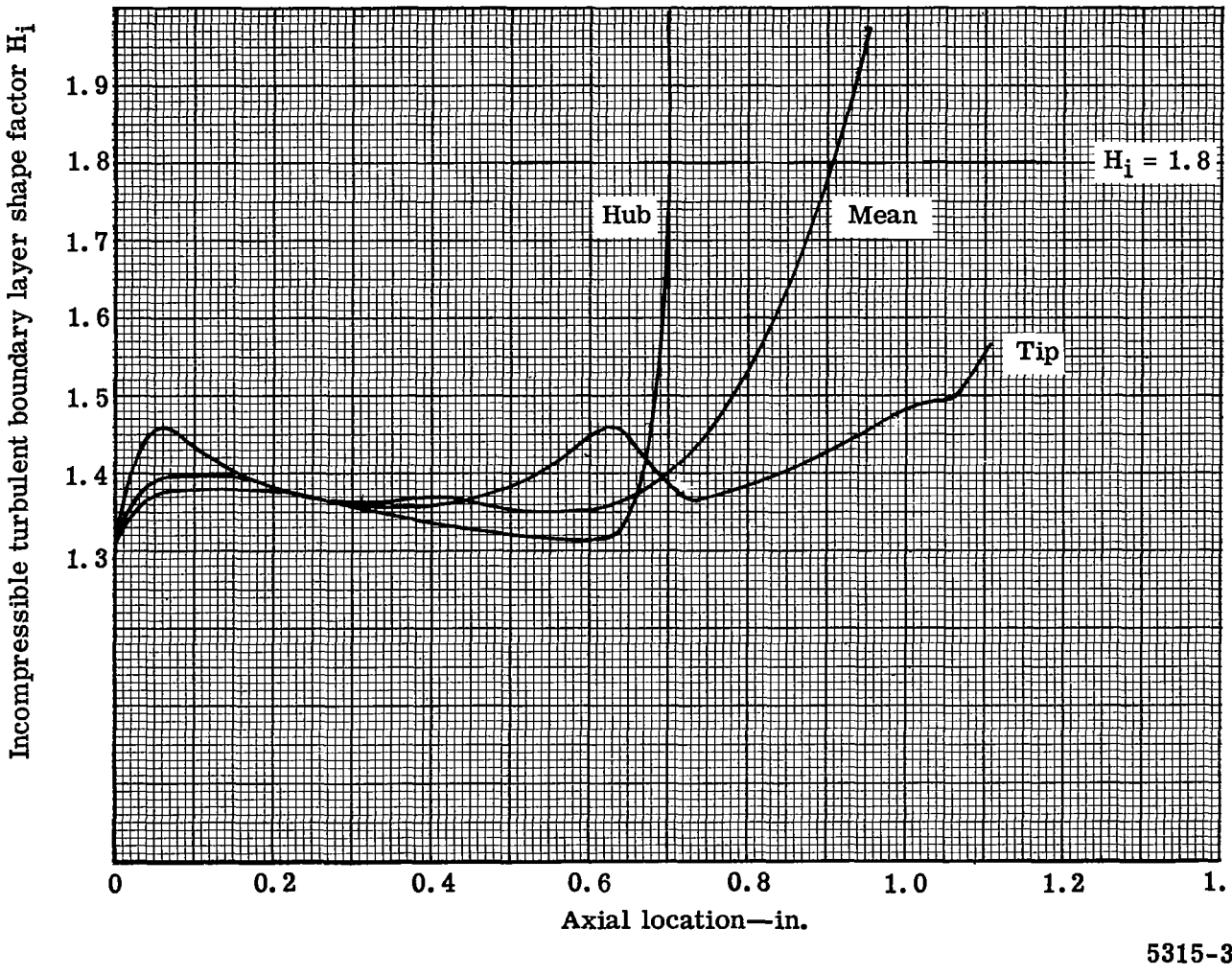

Figure 39. Jet-flapped blade suction surface incompressible boundary layer shape factor without jet flap.

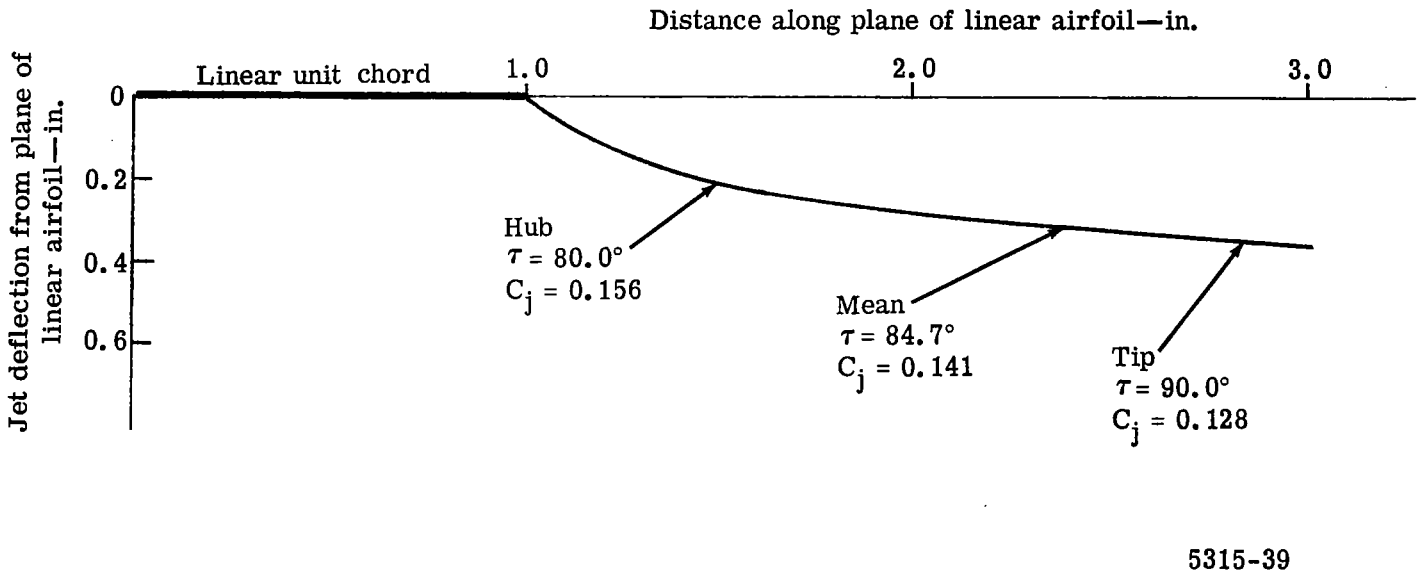

Figure 40. Jet flap contours for various jet momentum coefficients and jet efflux angles.

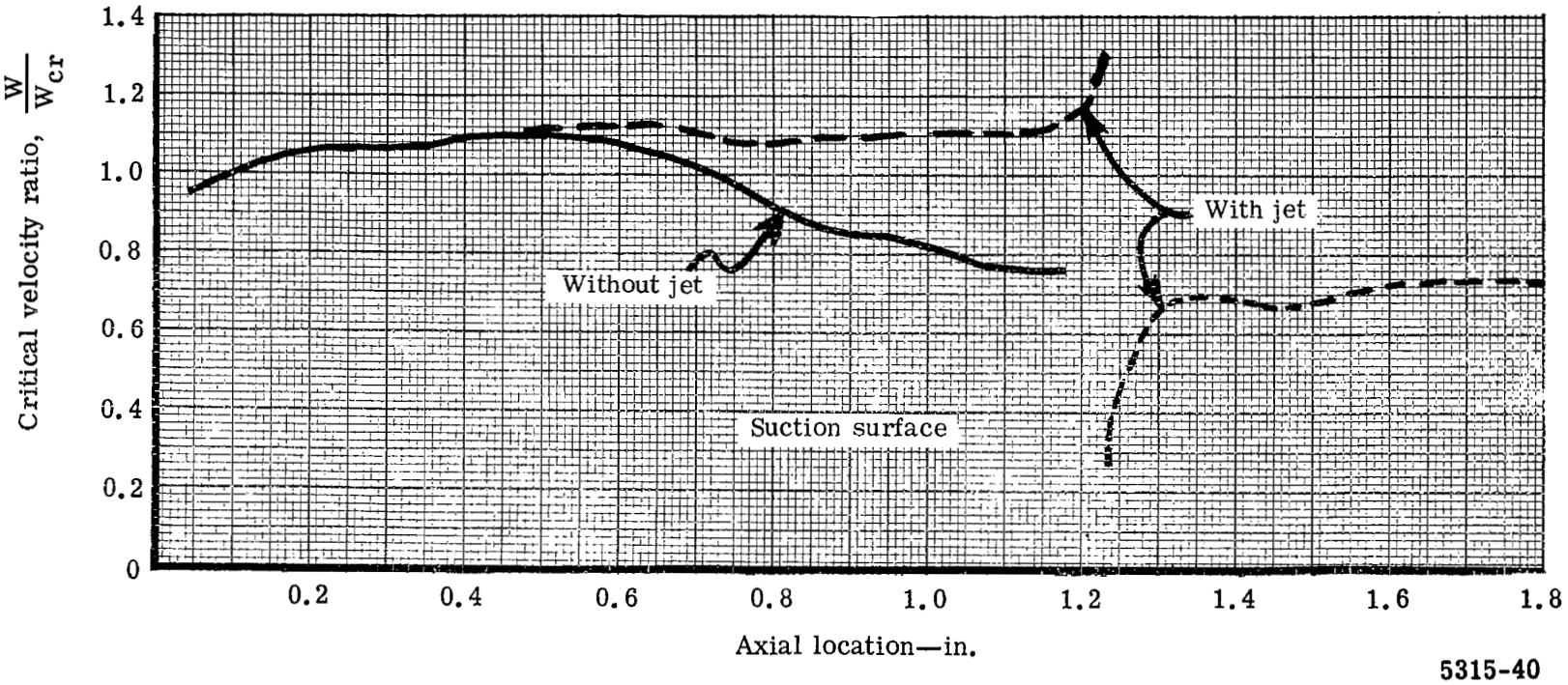

Figure 41. Jet-flapped blade hub section suction surface velocity distribution with and without jet flap based on two-dimensional incompressible solution.

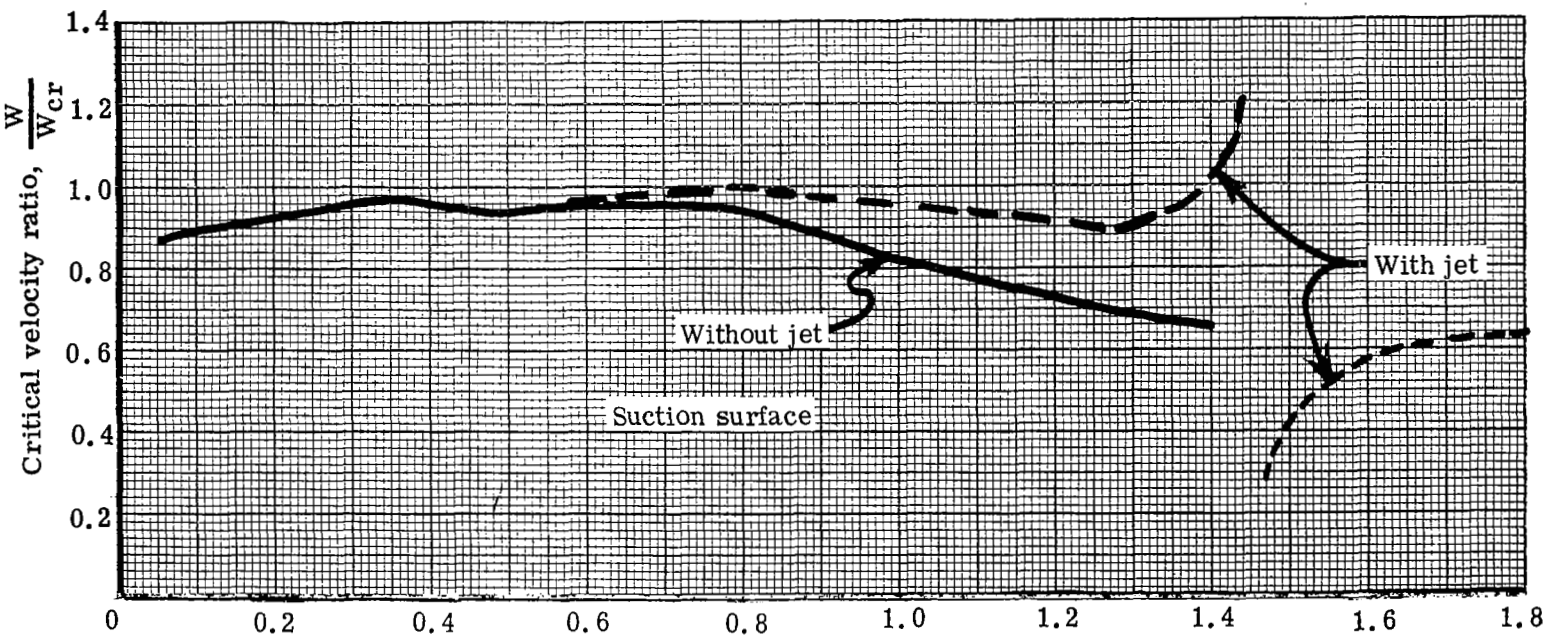

Figure 42. Jet-flapped blade mean section suction surface velocity distribution with and without jet flap based on two-dimensional incompressible solution.

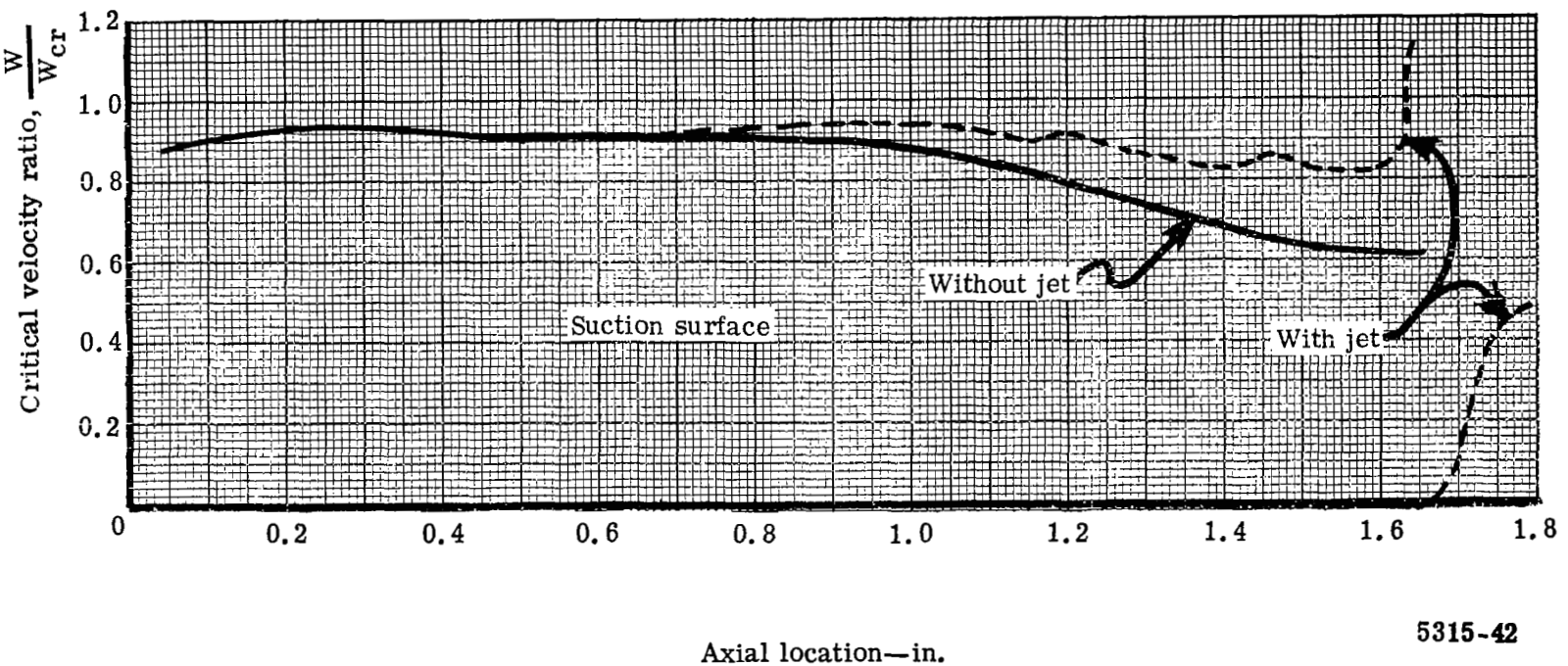

Figure 43. Jet-flapped blade tip section suction surface velocity distribution with and without jet flap based on two-dimensional incompressible solution.

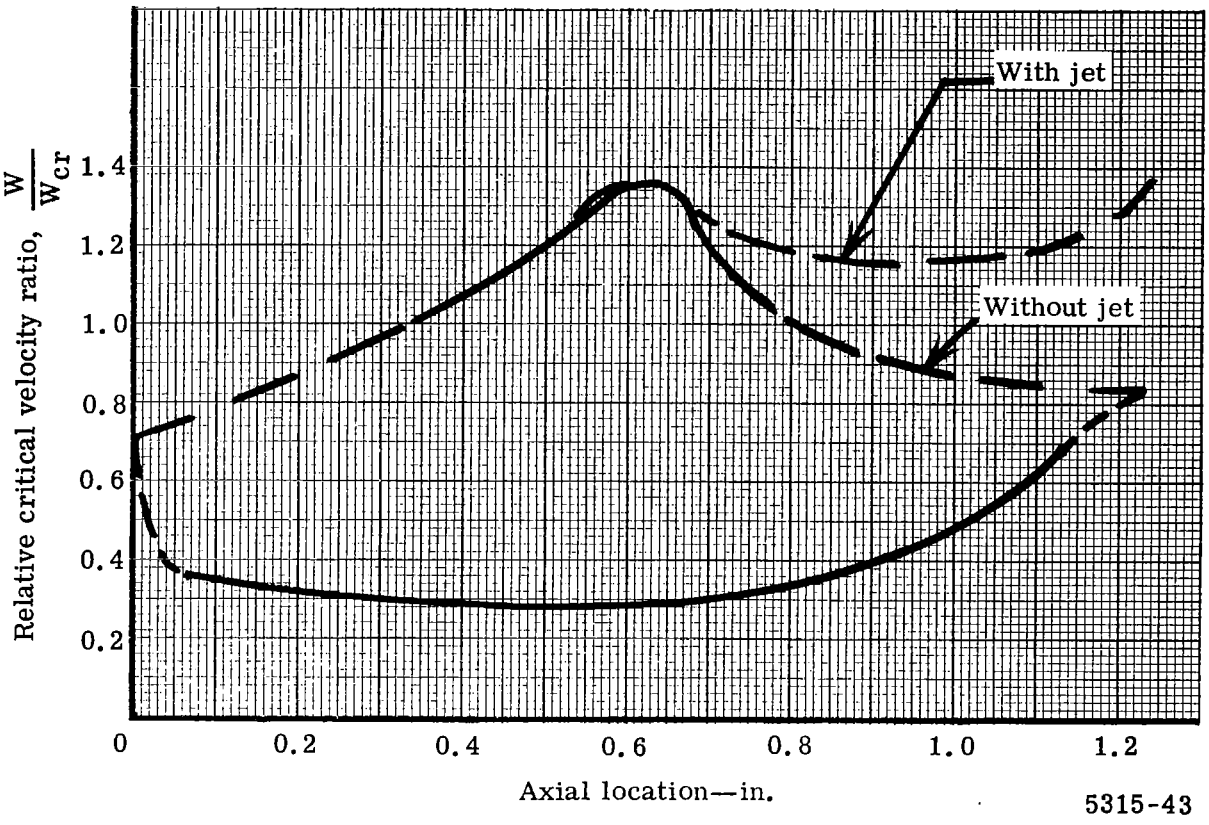

Figure 44. Jet-flapped blade hub section surface velocity distribution with and without jet flap based on quasi three-dimensional compressible solution.

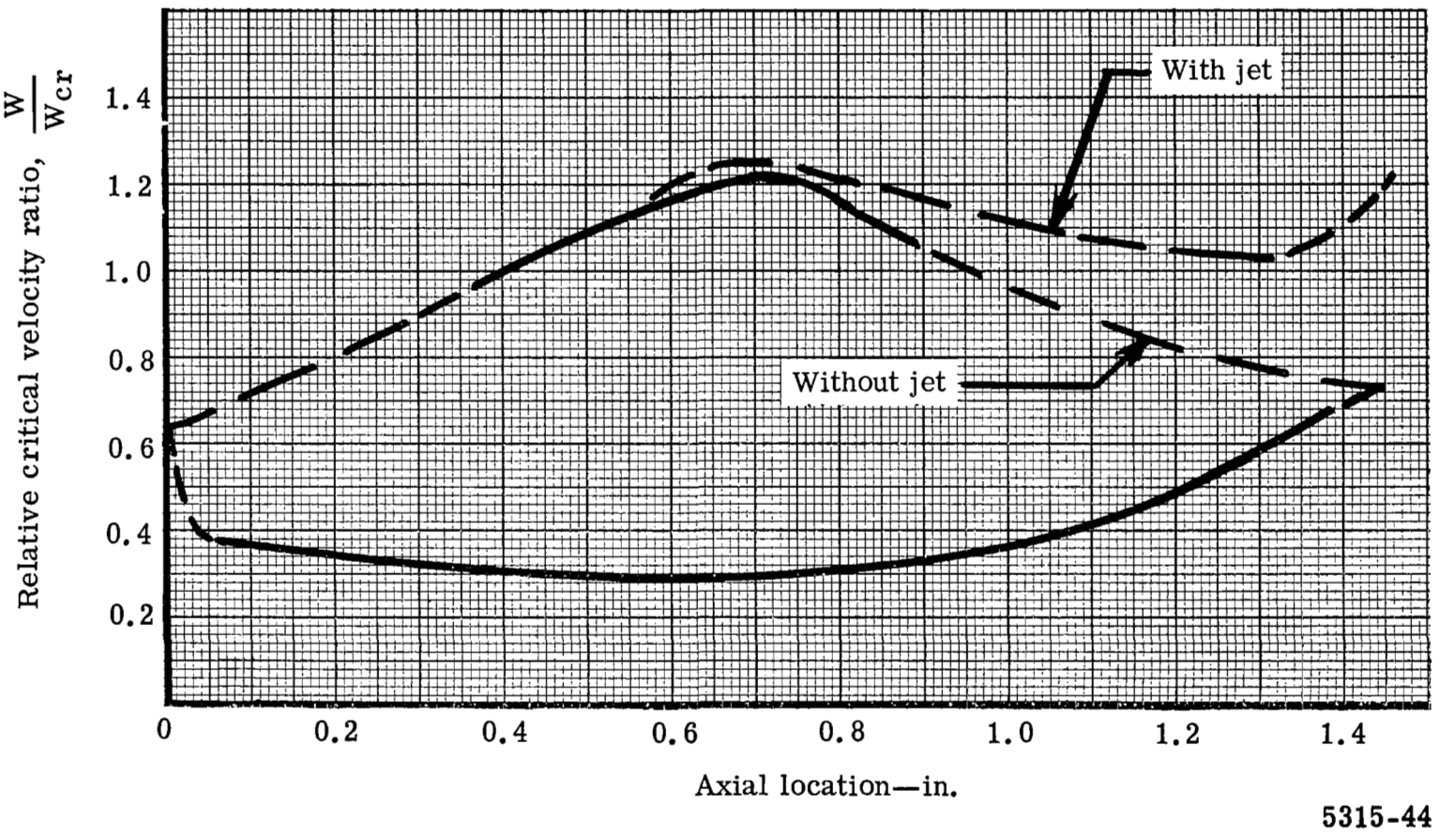

Figure 45. Jet-flapped blade mean section surface velocity distribution with and without jet flap based on quasi three-dimensional compressible solution.

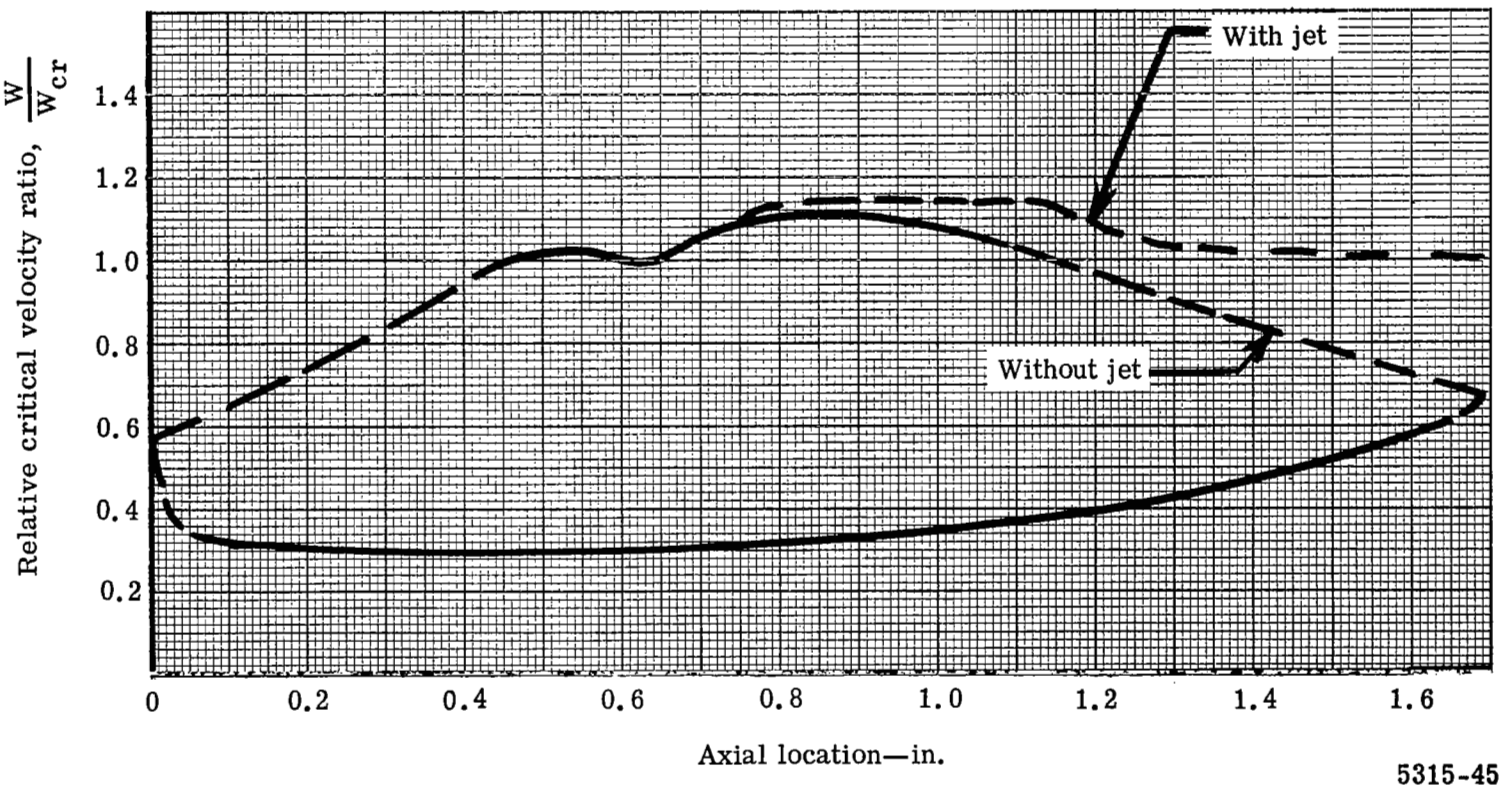

Figure 46. Jet-flapped blade tip section surface velocity distribution with and without jet flap based on quasi three-dimensional compressible solution.

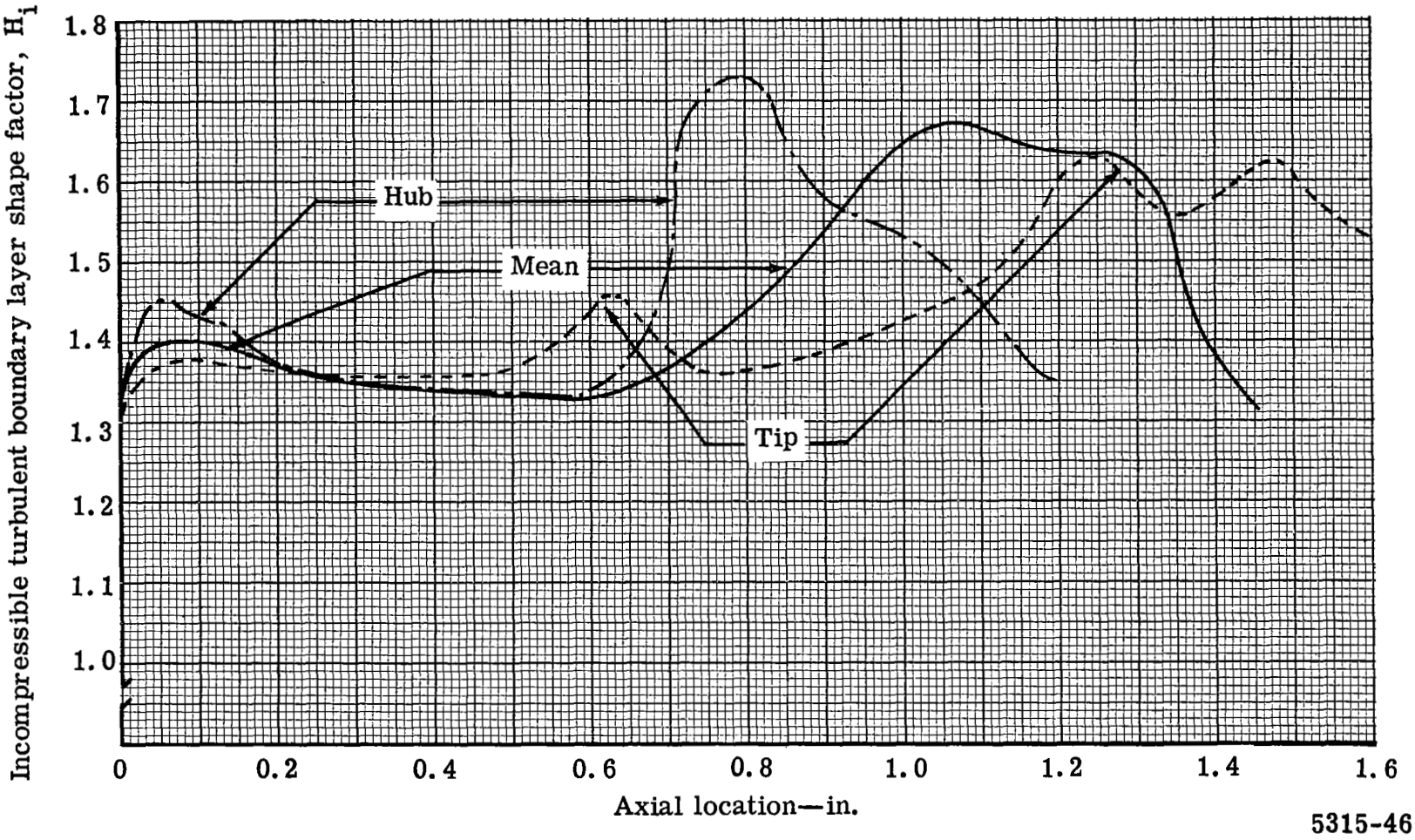

Figure 47. Jet-flapped blade incompressible boundary layer shape factor with jet flap.

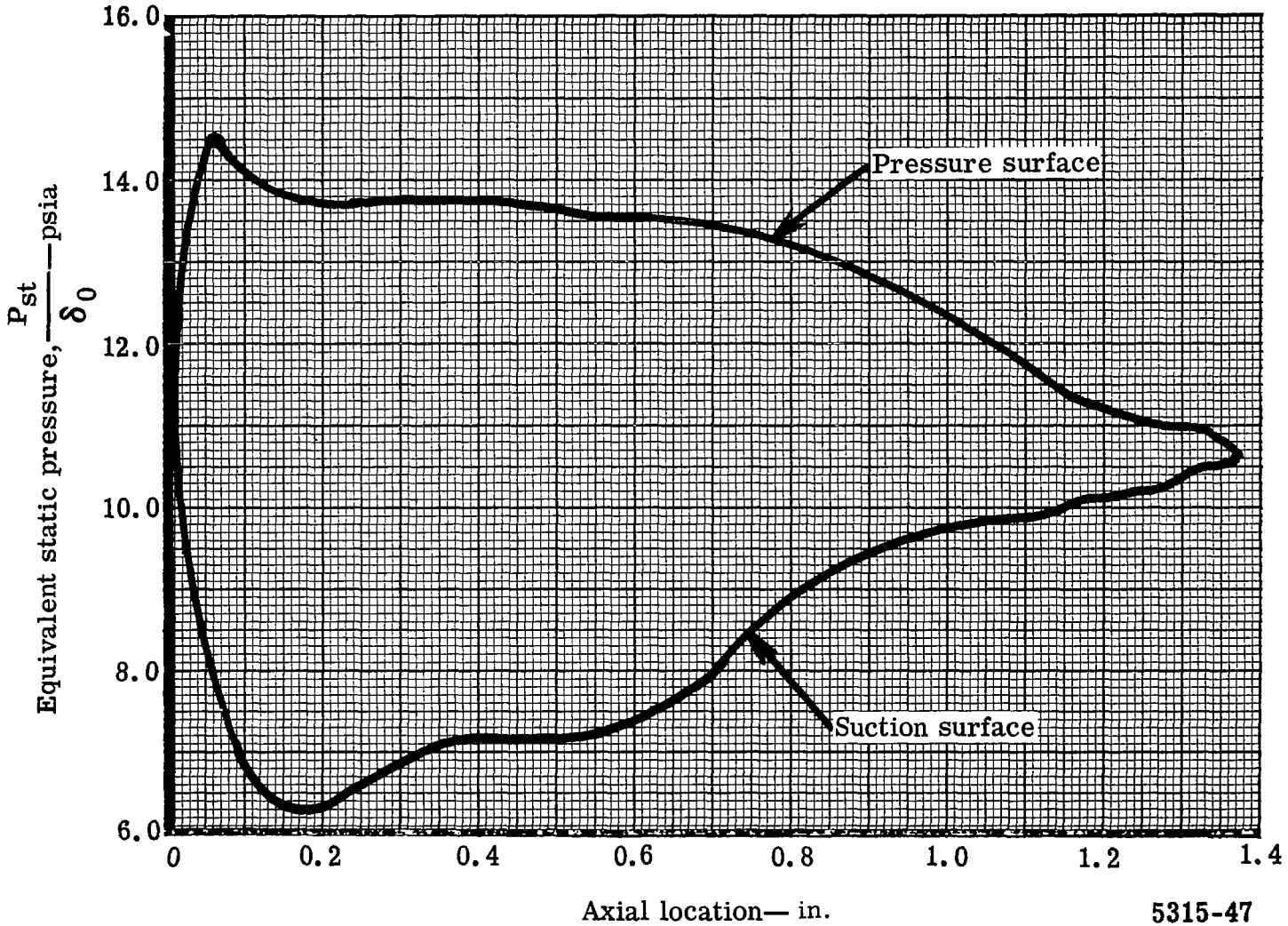

Figure 48. Plain blade hub section surface static pressure distribution based on two-dimensional incompressible solution.

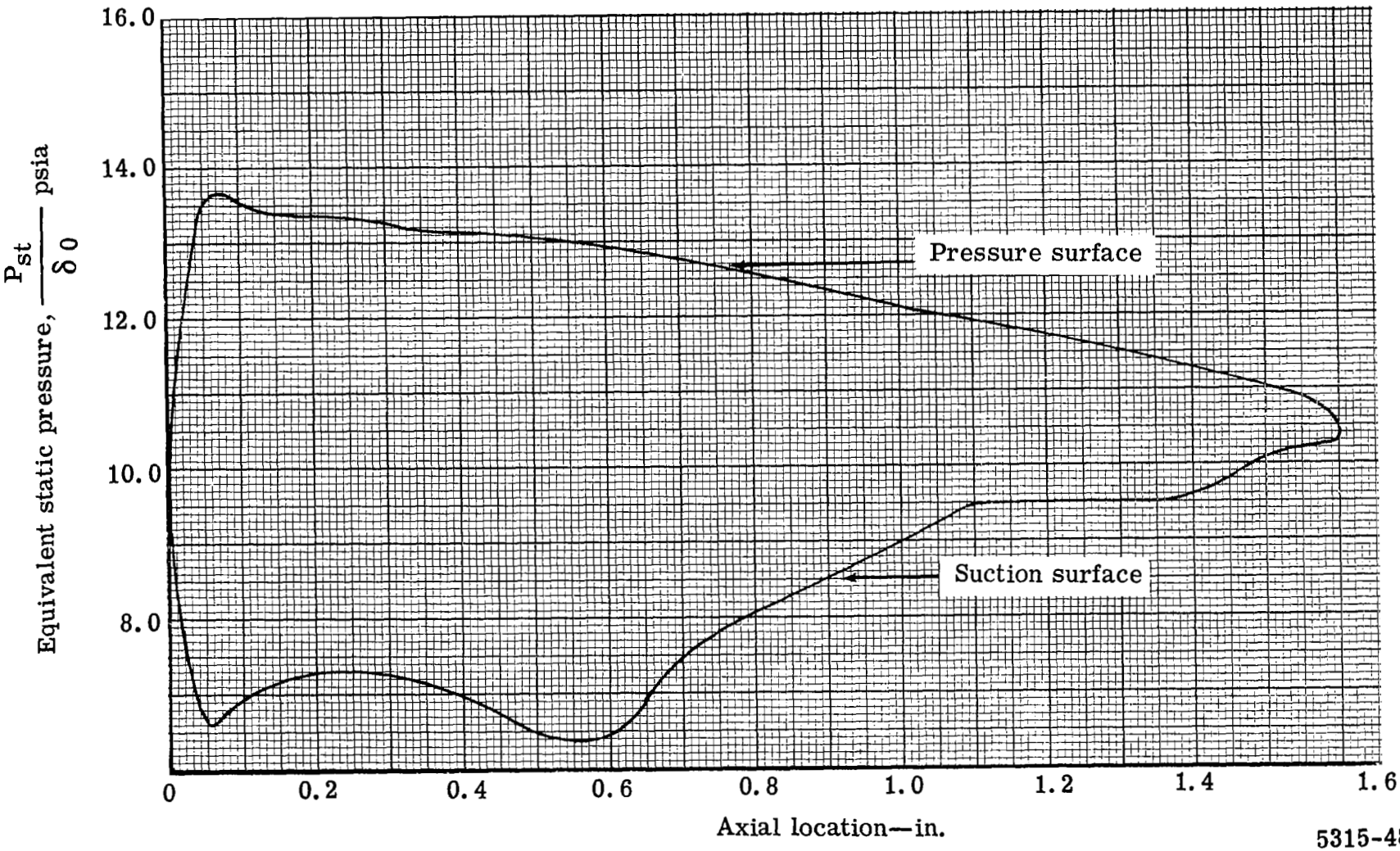

Figure 49. Plain blade mean section surface static pressure distribution based on two-dimensional incompressible solution.

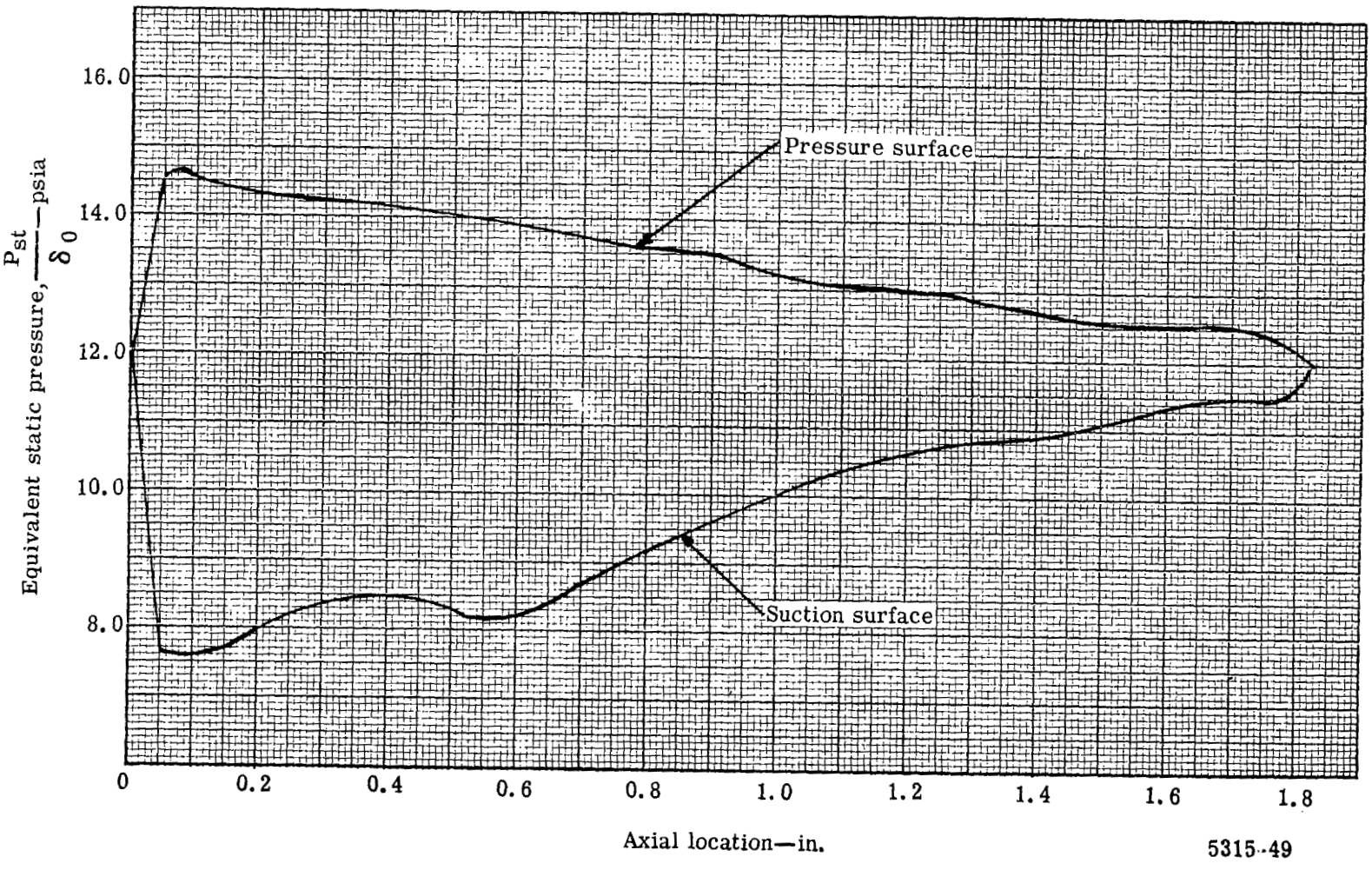

Figure 50. Plain blade tip section surface static pressure distribution based on two-dimensional incompressible solution.

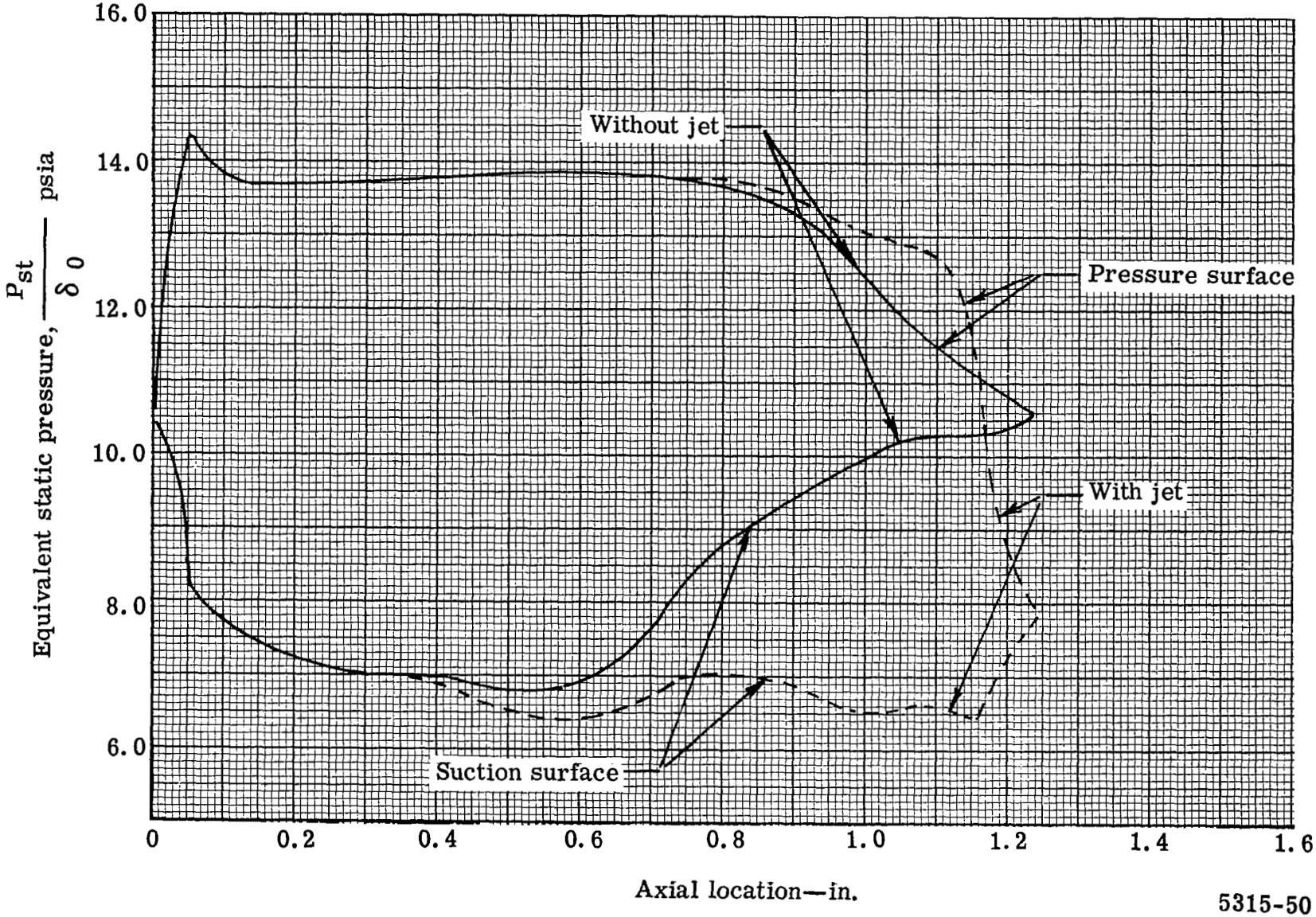

Figure 51. Jet-flapped blade hub section surface static pressure distribution with and without jet flap based on two-dimensional incompressible solution.

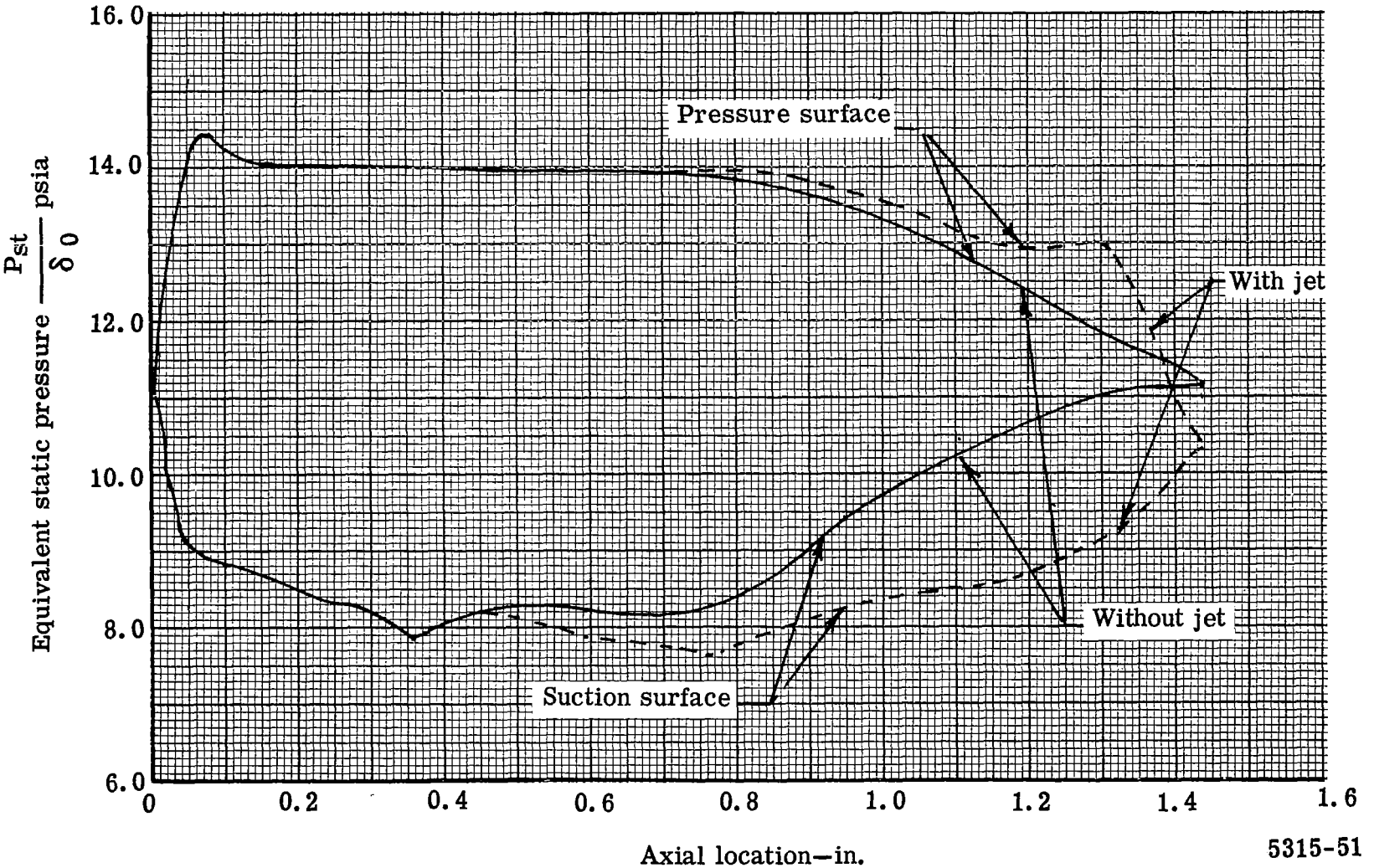

Figure 52. Jet-flapped blade mean section surface static pressure distribution with and without jet flap based on two-dimensional incompressible solution.

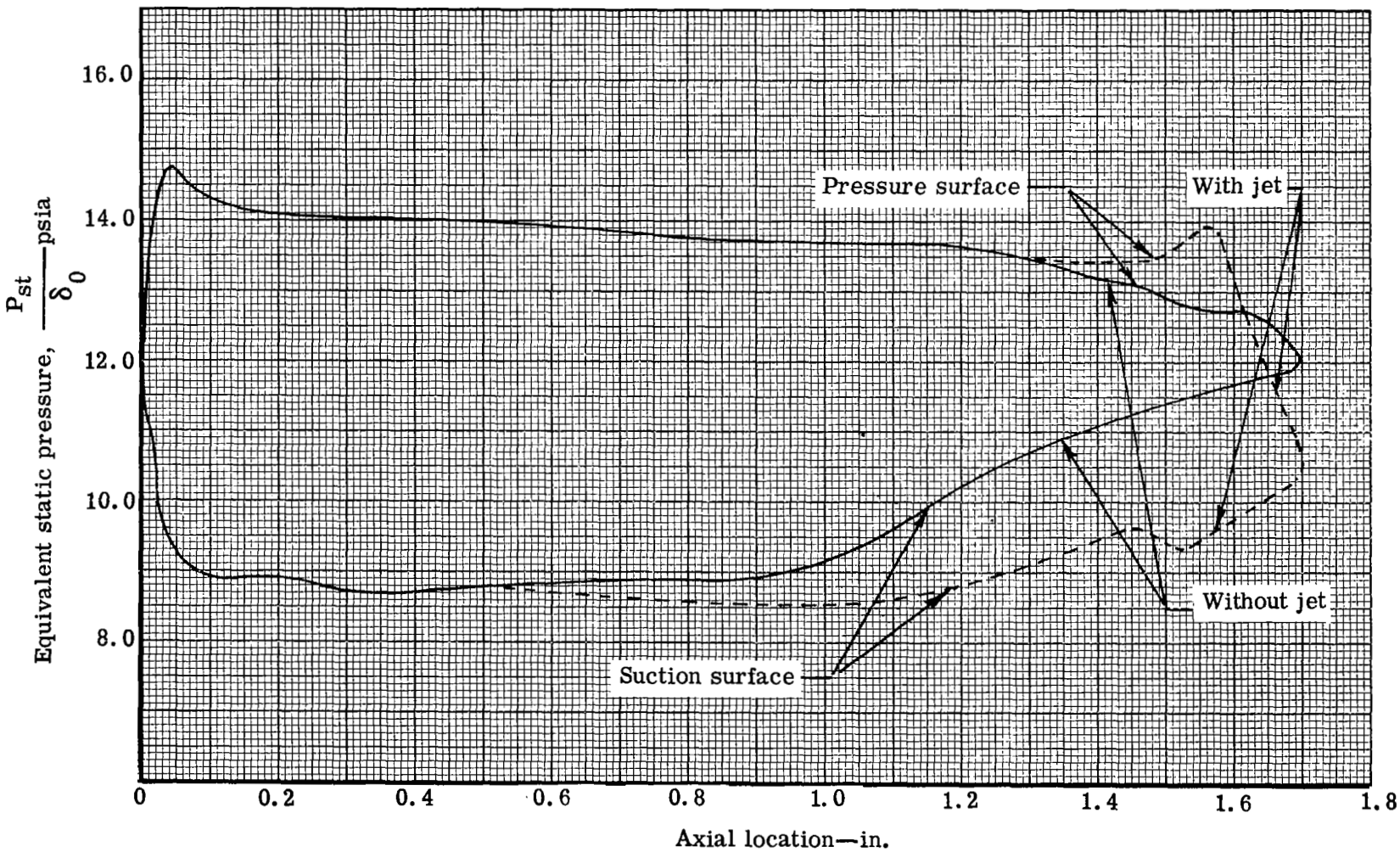

Figure 53. Jet-flapped blade tip section surface static pressure distribution with and without jet flap based on two-dimensional incompressible solution.

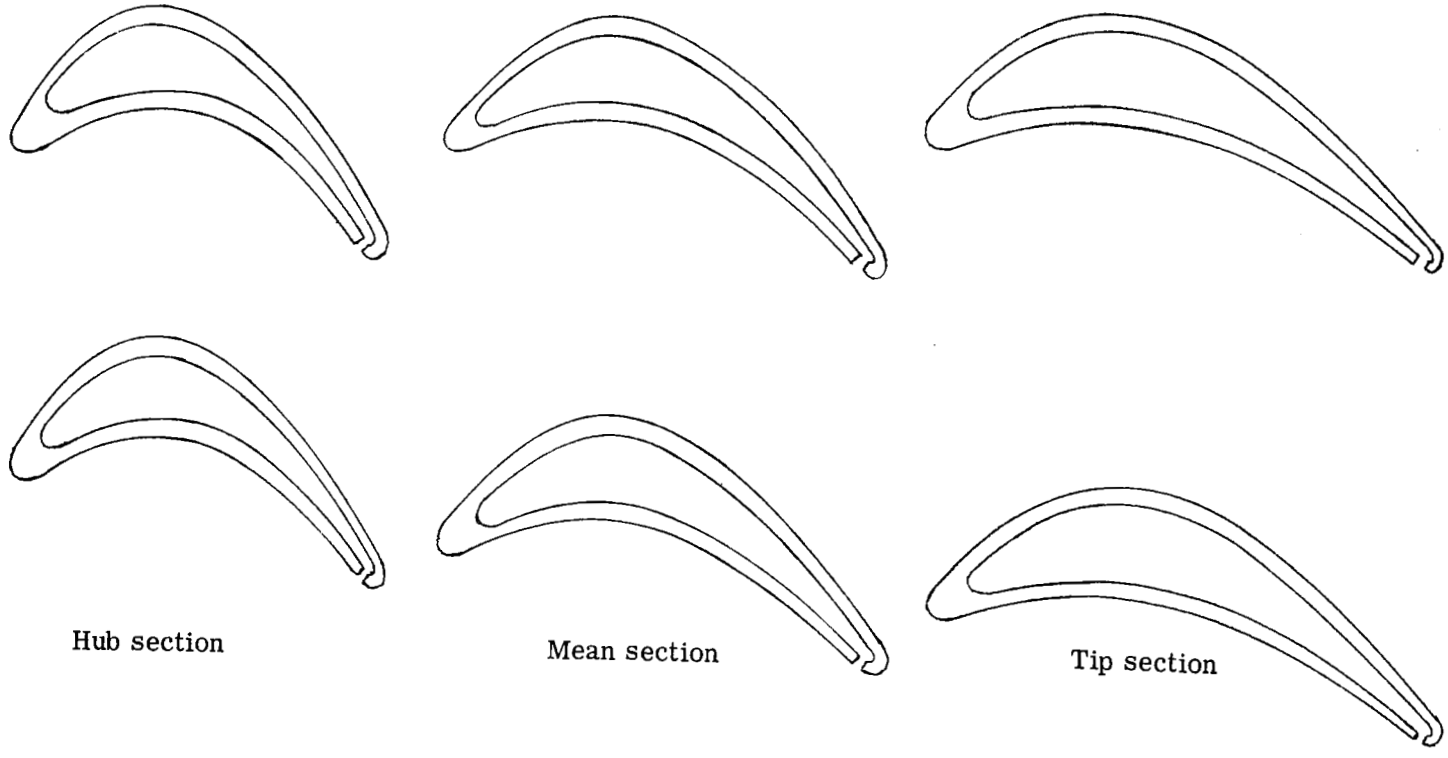

Figure 54. Jet-flapped blade profiles and passages.
See Tables XIII through XXIII.

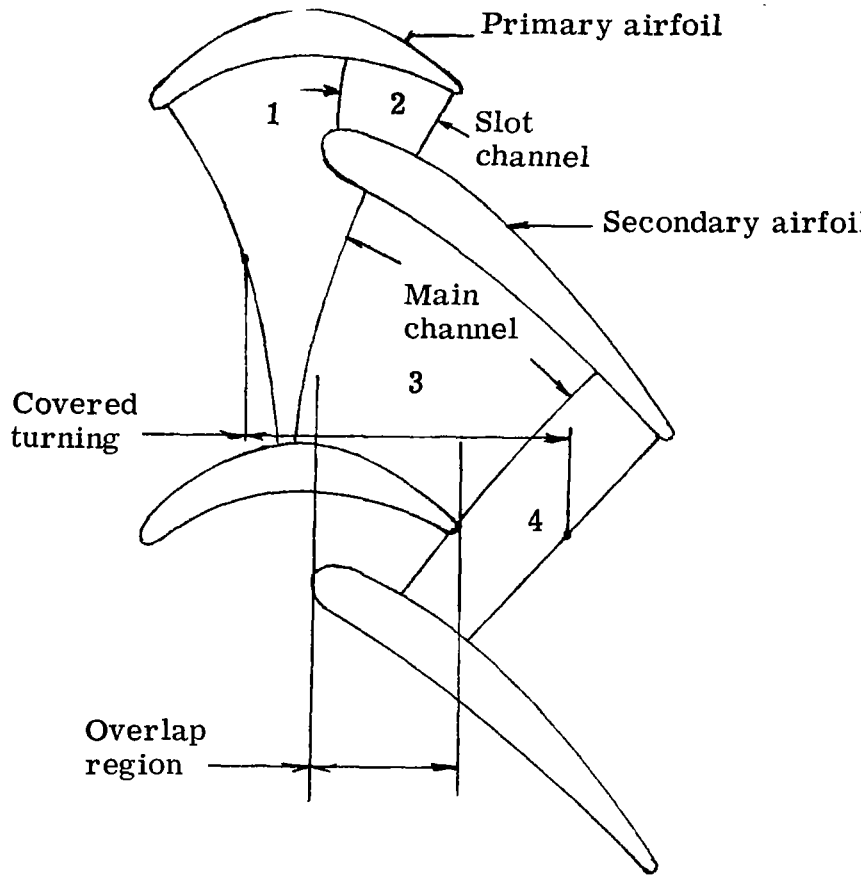

5315-54

Figure 55. Tandem blade notation.

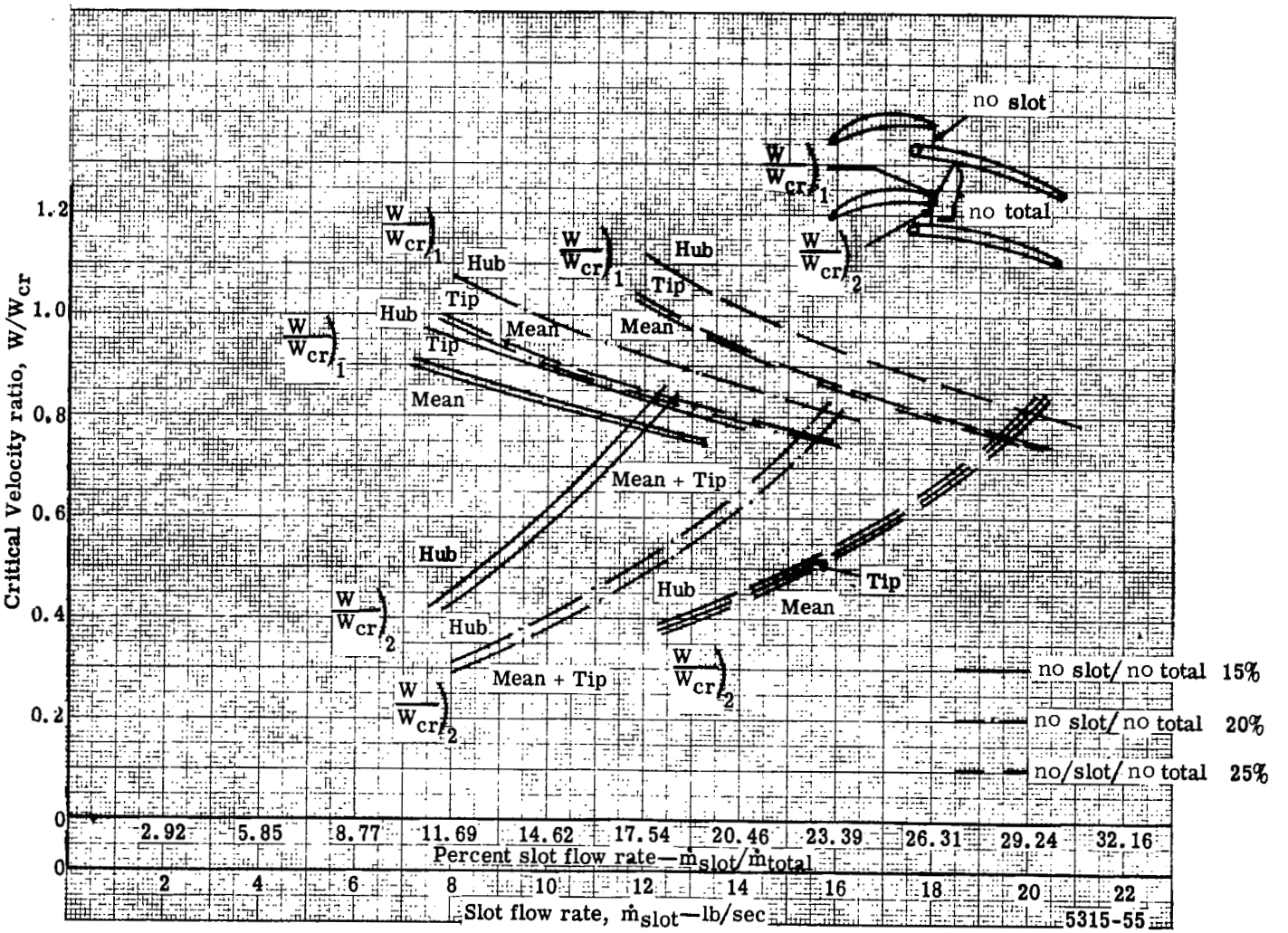

Figure 56. Effect of flow distribution and primary airfoil trailing edge location on critical velocity ratio level for tandem blade.

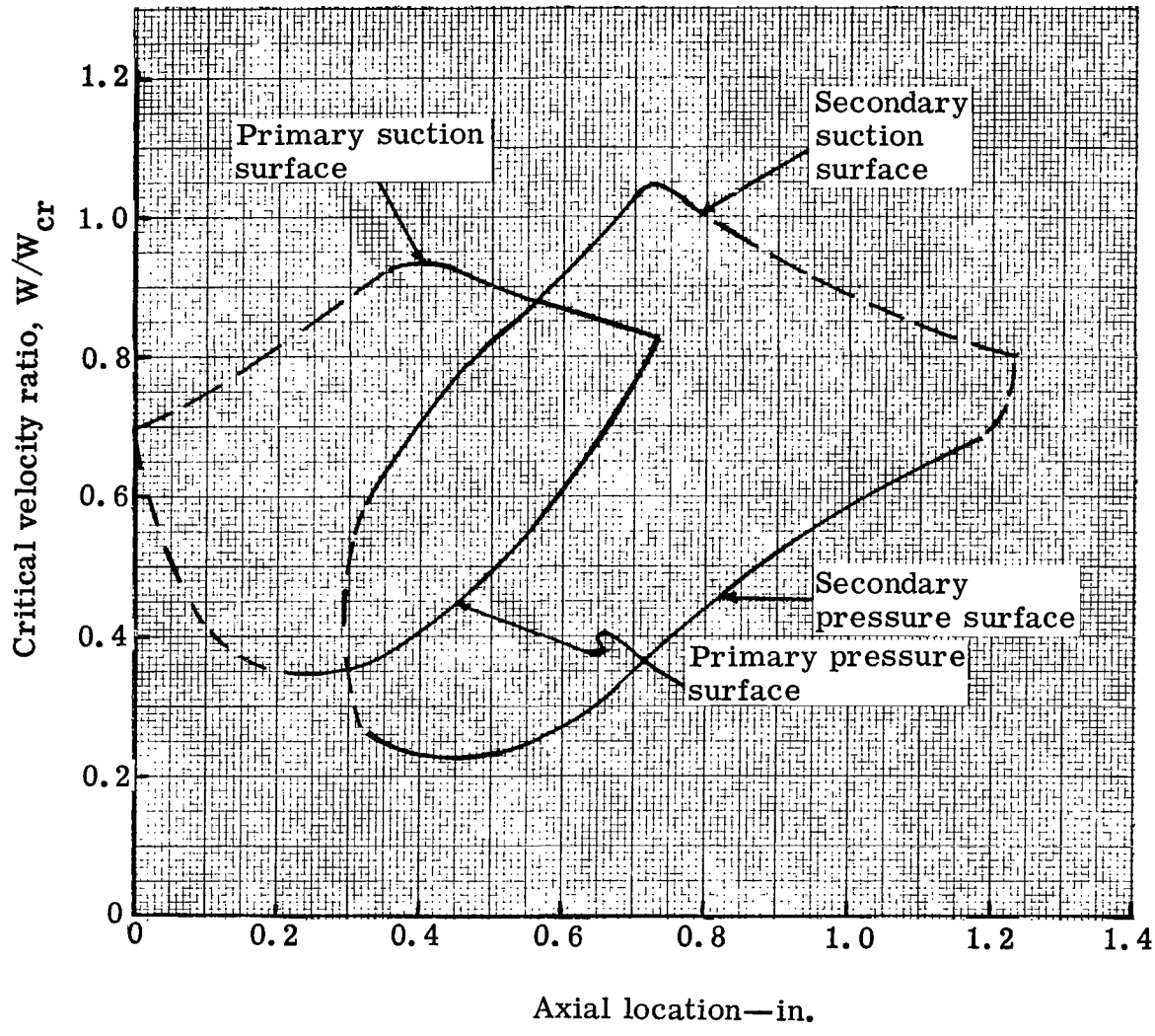

Figure 57. Tandem blade hub section surface velocity distribution.

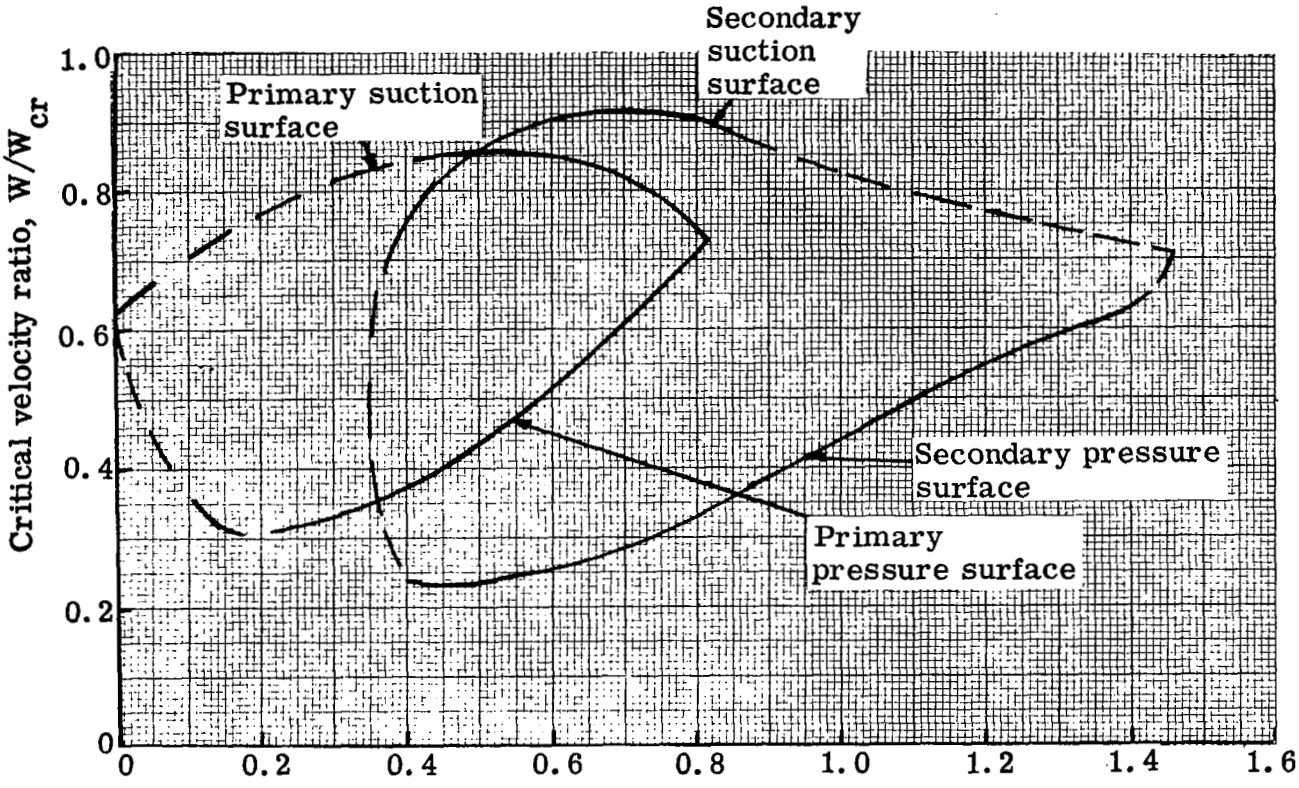

Figure 58. Tandem blade mean section surface velocity distribution.

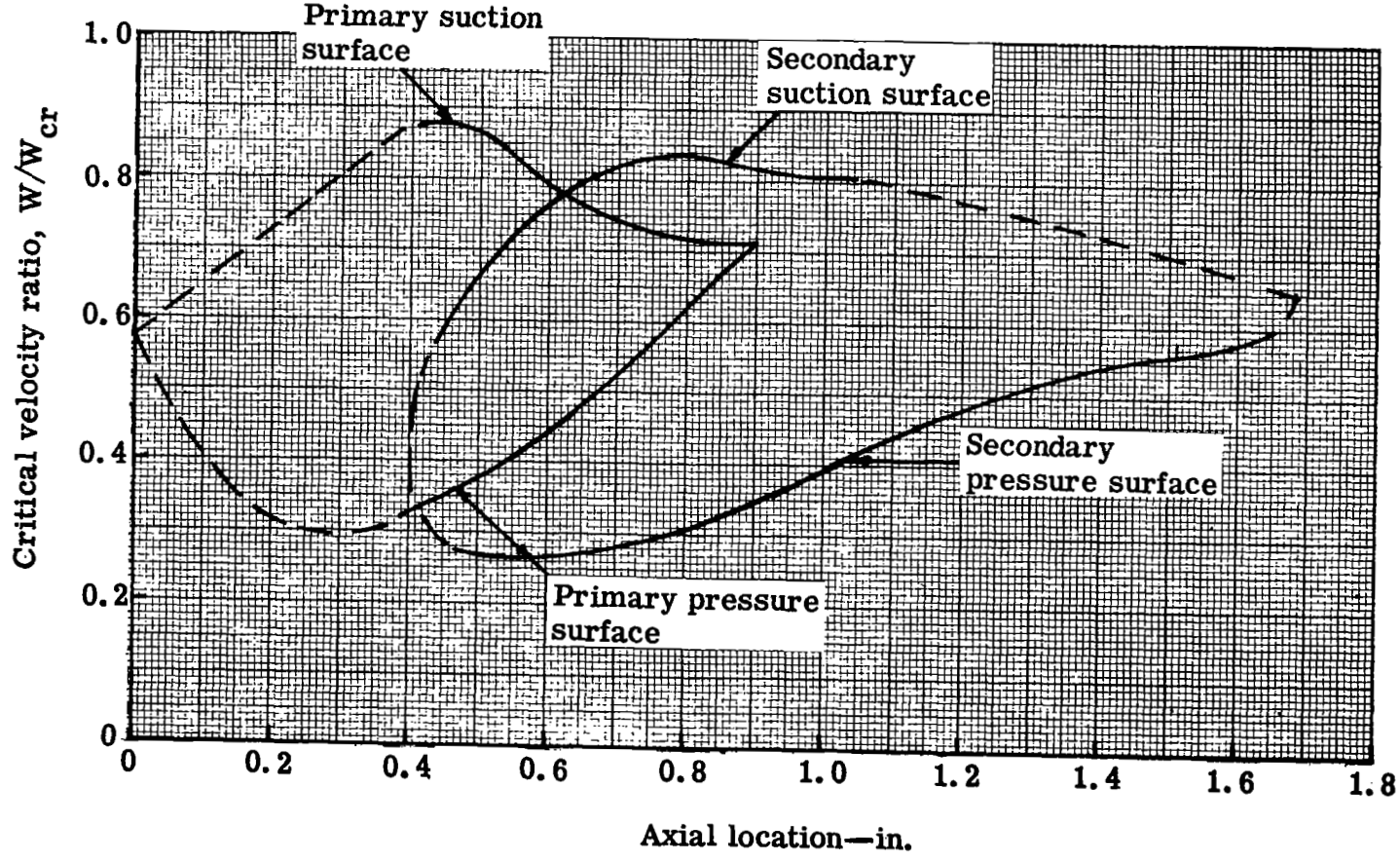

Figure 59. Tandem blade tip section surface velocity distribution.

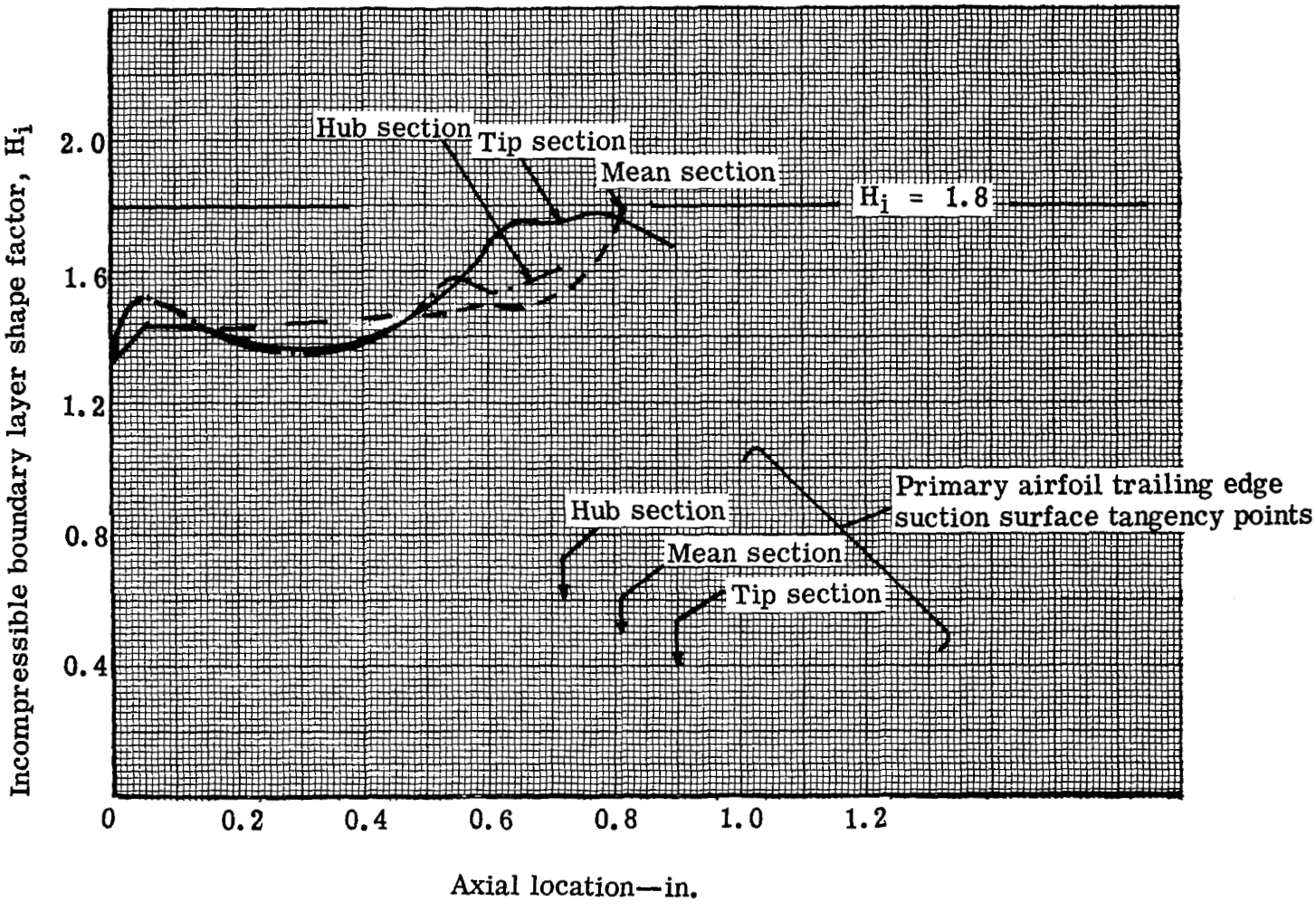

Figure 60. Tandem blade primary airfoil suction surface incompressible boundary layer shape factor.

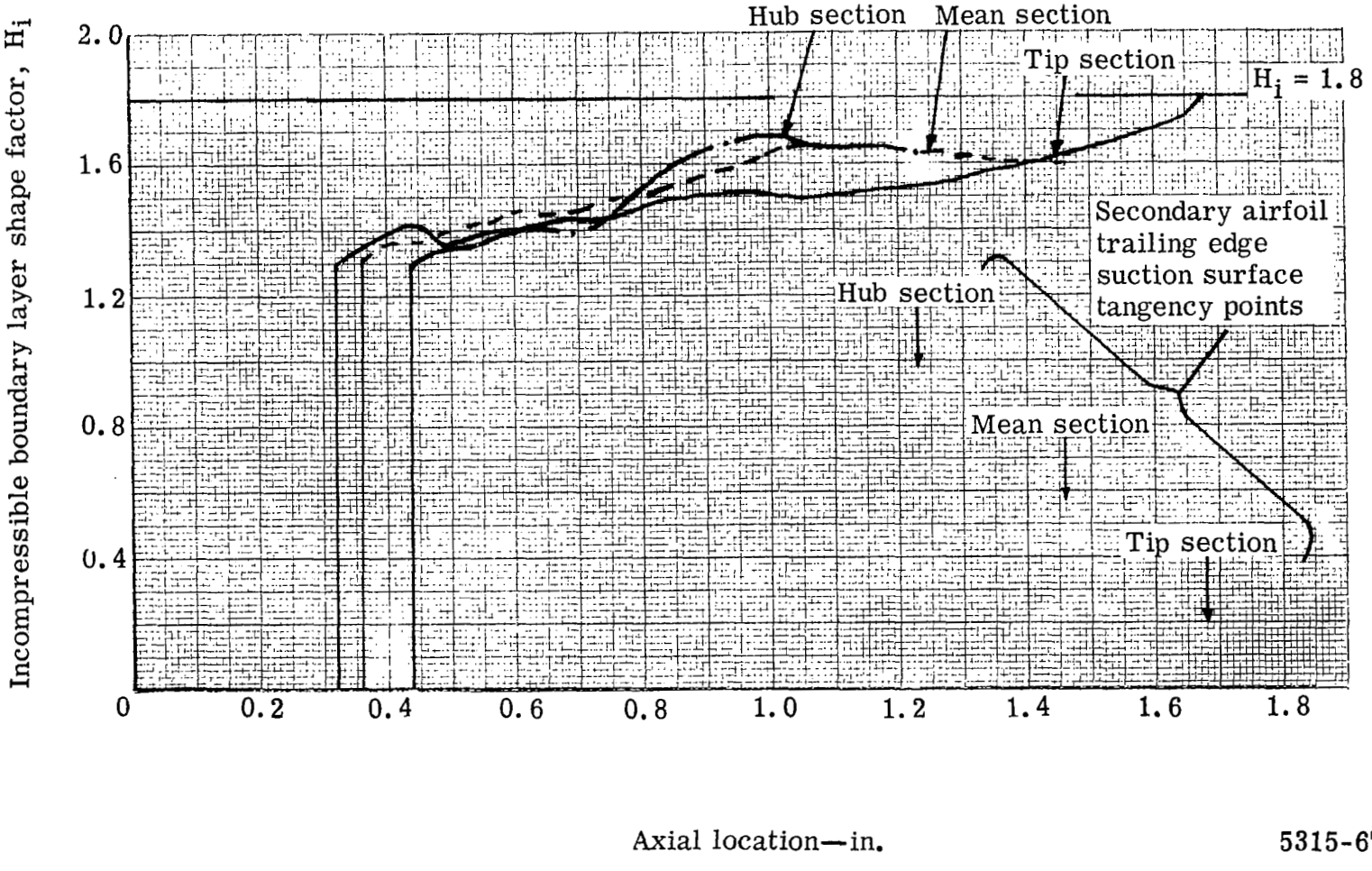

Figure 61. Tandem blade secondary airfoil suction surface incompressible boundary layer shape factor.

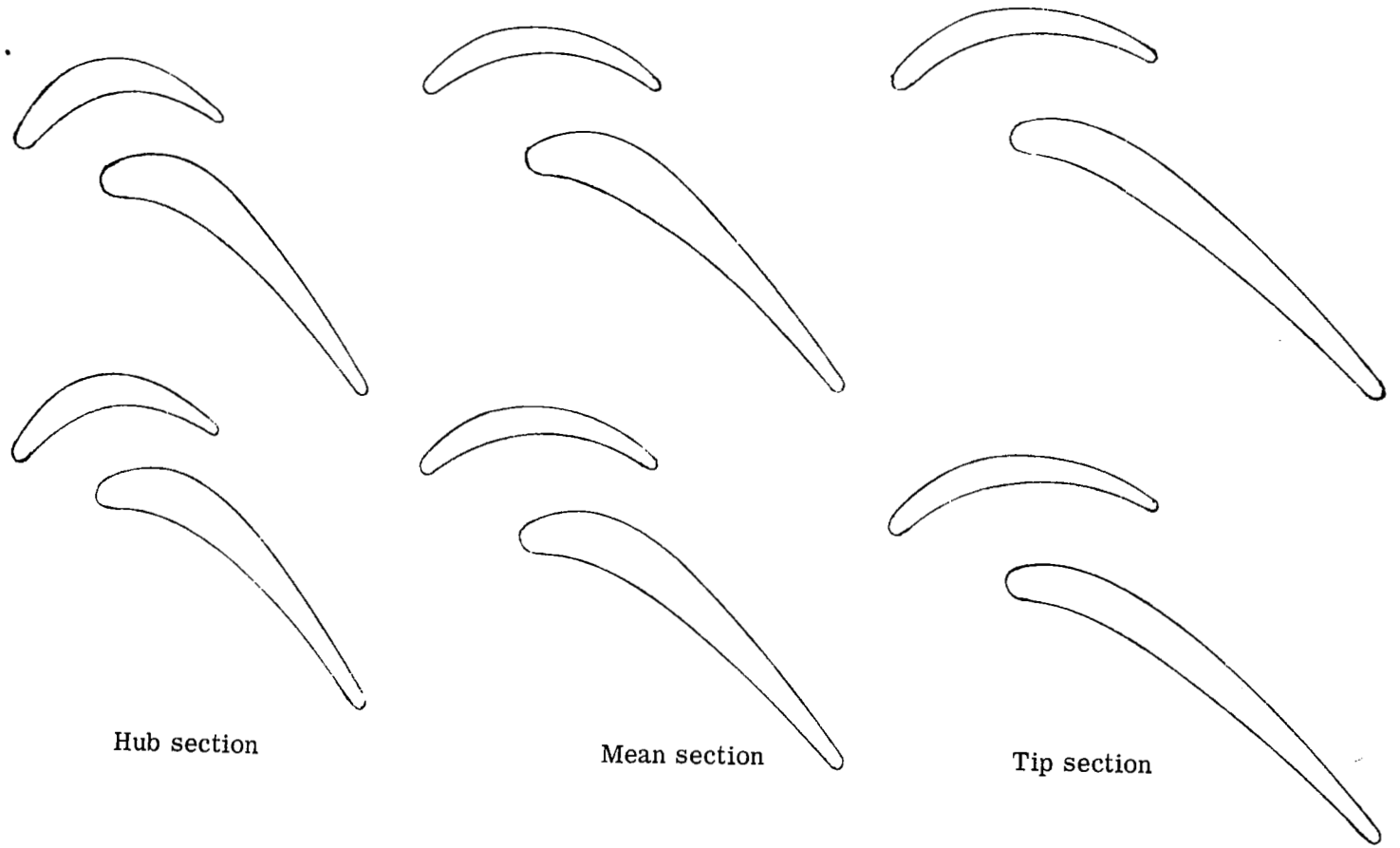

Figure 62. Tandem blade profiles and passages.

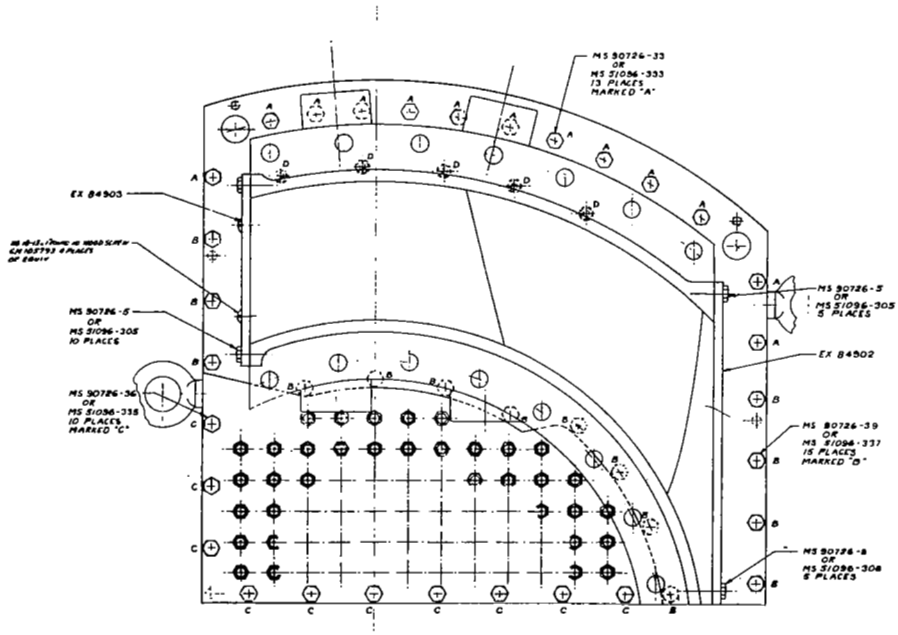
MS 90726-33
OR
MS 21086-333
13 PLACES
MARKED "A"
EX 84503
MS 90726-5
OR
MS 21086-305
10 PLACES
MS 90726-36
OR
MS 21086-338
10 PLACES
MARKED "C"
MS 90726-5
OR
MS 21086-305
5 PLACES
EX 84502
MS 90726-39
OR
MS 21086-337
15 PLACES
MARKED "B"
MS 90726-8
OR
MS 21086-308
8 PLACES

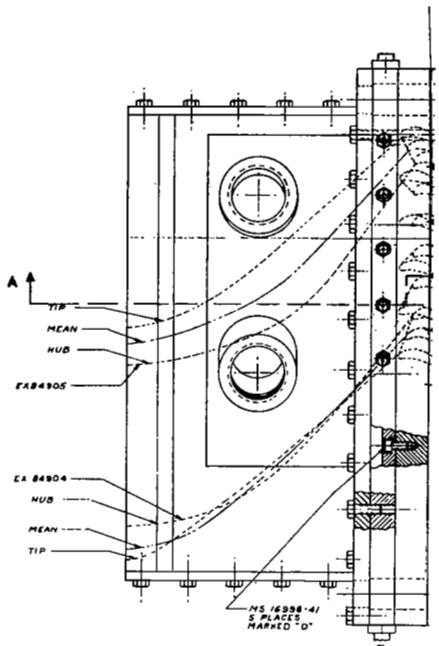
A
TIP
MEAN
HUB
EX84505
EX 84504
HUB
MEAN
TIP
MS 16998-41
5 PLACES
MARKED "D"

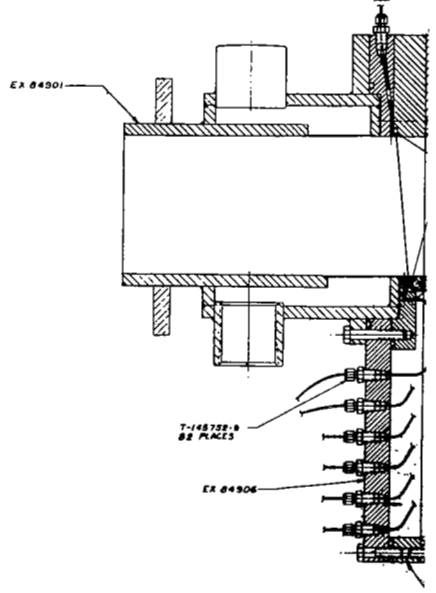
EX 84501
T-148758-9
82 PLACES
EX 84506

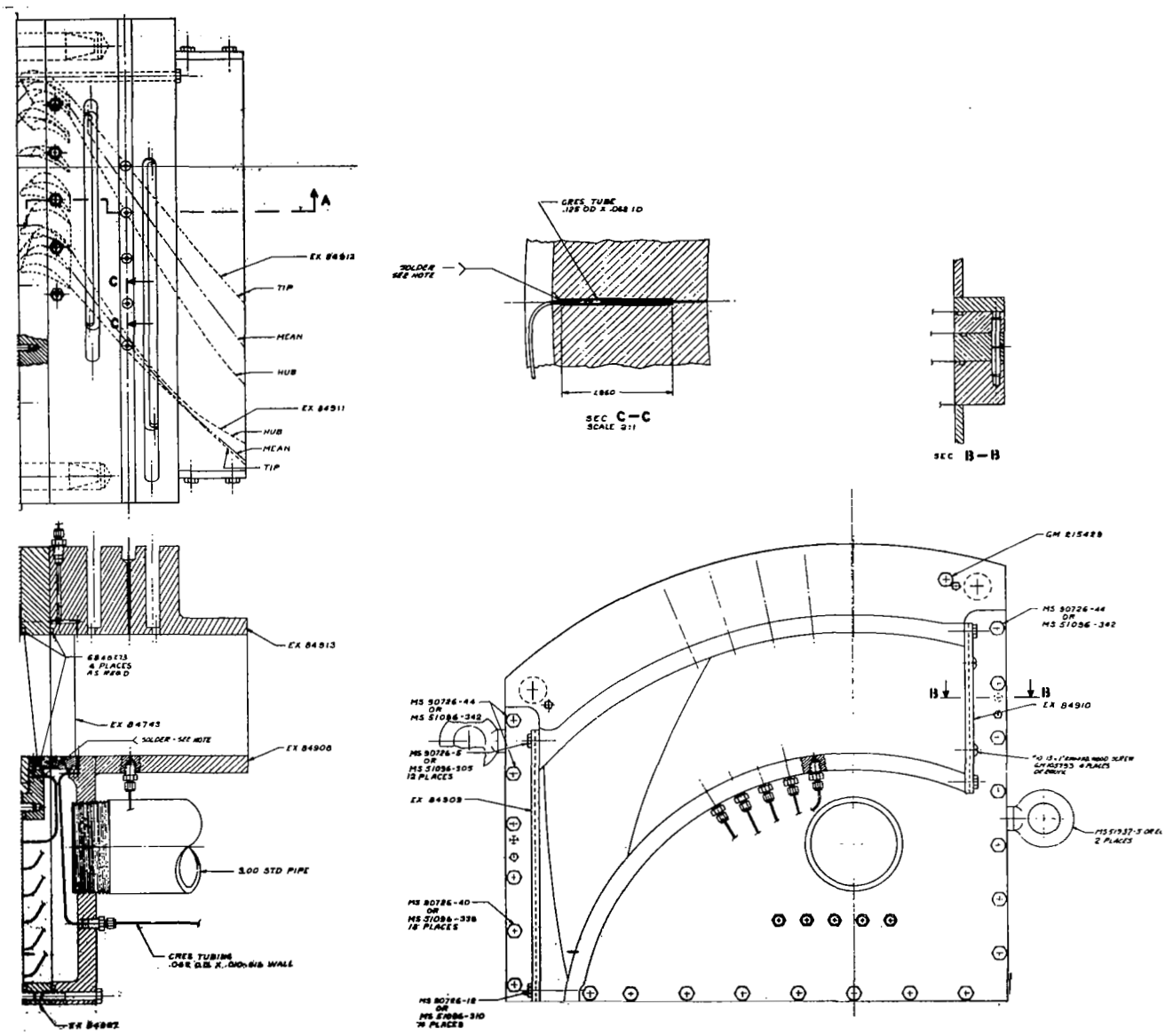

Figure 63. NASA turbine cascade assembly.

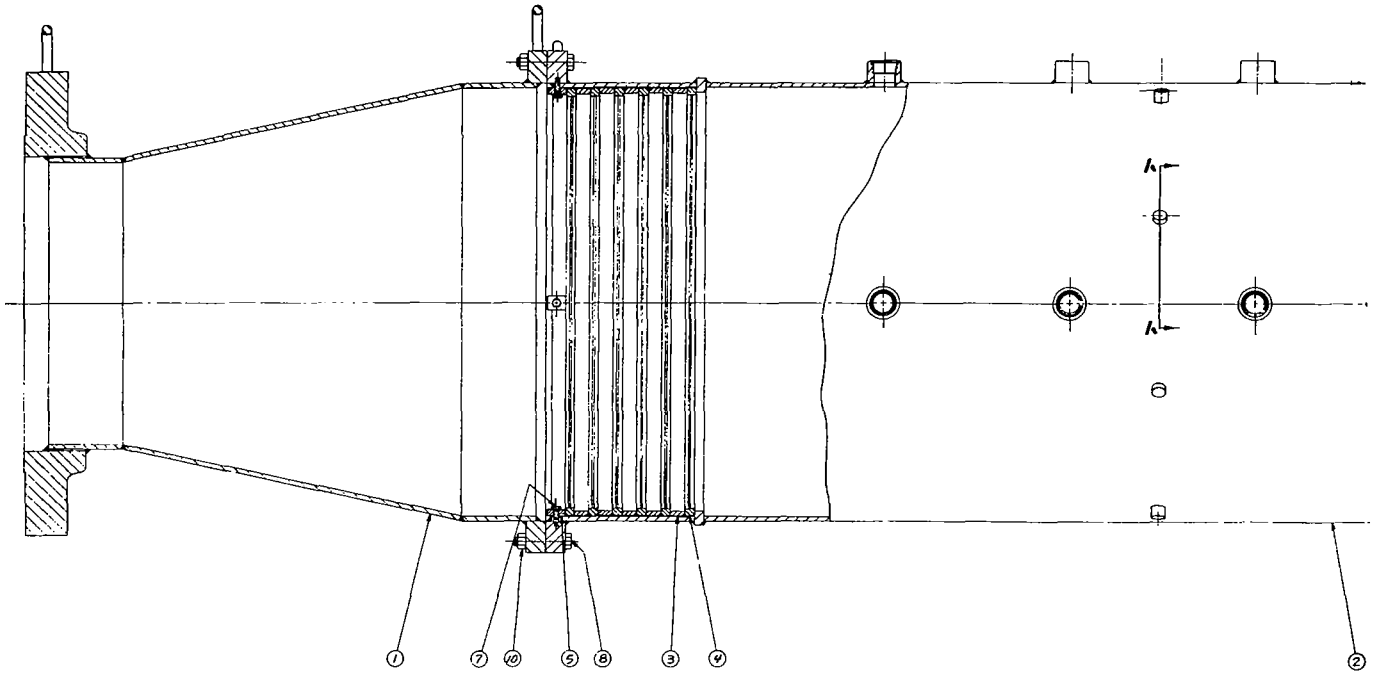
h
h
1
7
10
5
8
3
4
2

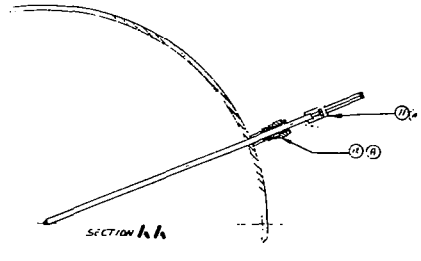
SECTION h-h

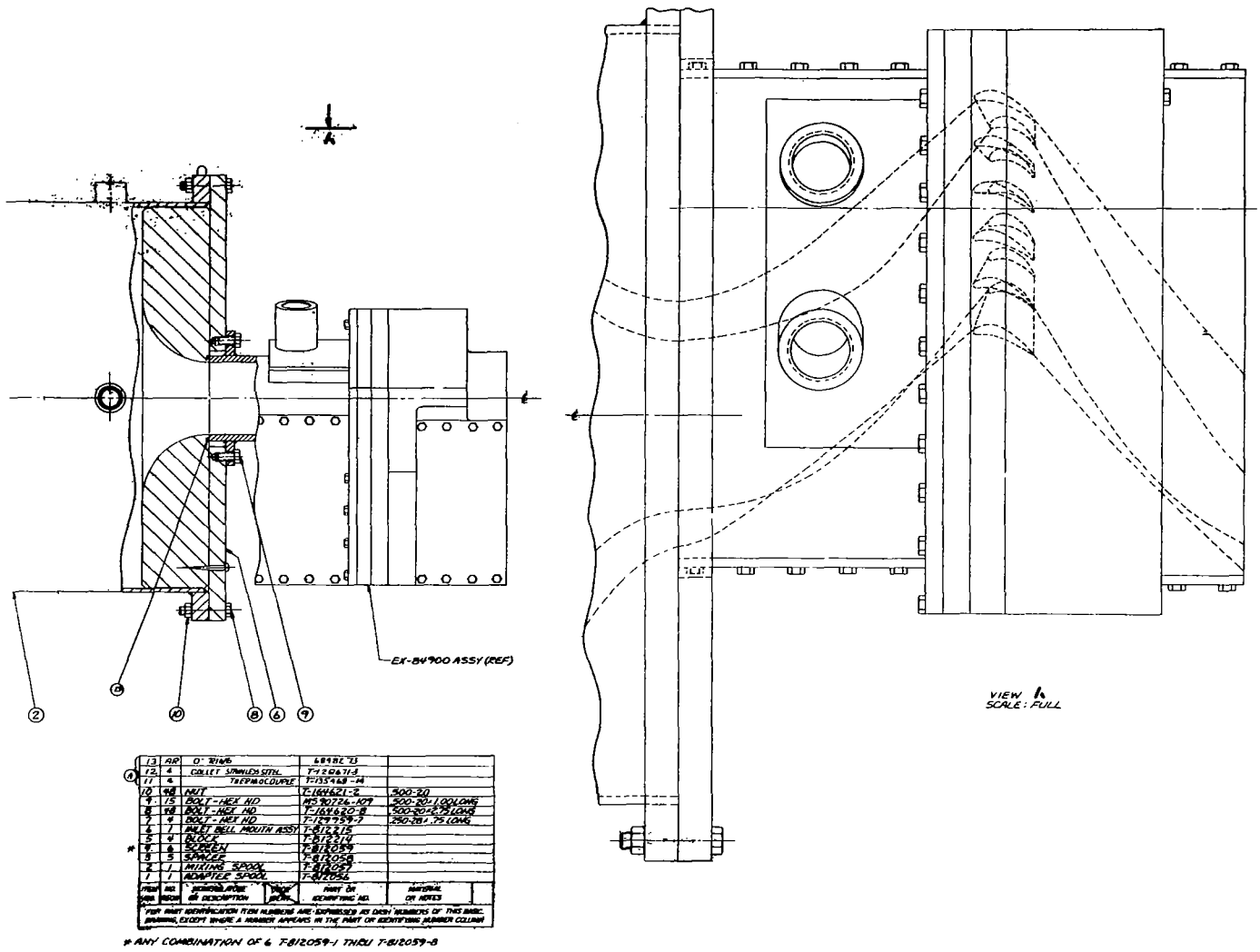

ITEM	NO.	DESCRIPTION	PART OR IDENTIFYING NO.	MATERIAL OR NOTES
13	AR	O' RING	6898Z-13	
12	4	COLLET STAINLESS STEEL	T-1206713	
11	4	THERMOCOUPLE	T-155468-4	
10	48	RIVET	T-1614Z1-2	302-20
9	15	BOLT - HEX HD	MS90726-40P	302-20-1.00 LONG
8	98	BOLT - HEX HD	T-164620-8	302-20-2.75 LONG
7	4	BOLT - HEX HD	T-164959-7	250-28-1.75 LONG
6	1	INLET BELL MOUTH ASSY	T-812375	
5	4	BLOCK	T-812511	
* 4	6	SCREEN	T-812059	
3	5	SPACER	T-812058	
2	1	MIXING SPOOL	T-812057	
1	1	ADAPTER SPOOL	T-812056	

FOR PART IDENTIFICATION ITEM NUMBERS ARE EXPRESSED AS DASH NUMBERS OF THIS BASIC DRAWING, EXCEPT WHERE A NUMBER APPEARS IN THE PART OR IDENTIFYING NUMBER COLUMN

* ANY COMBINATION OF 6 T-812059-1 THRU T-812059-8

Figure 64. Inlet assembly straightener for annular cascade rig.

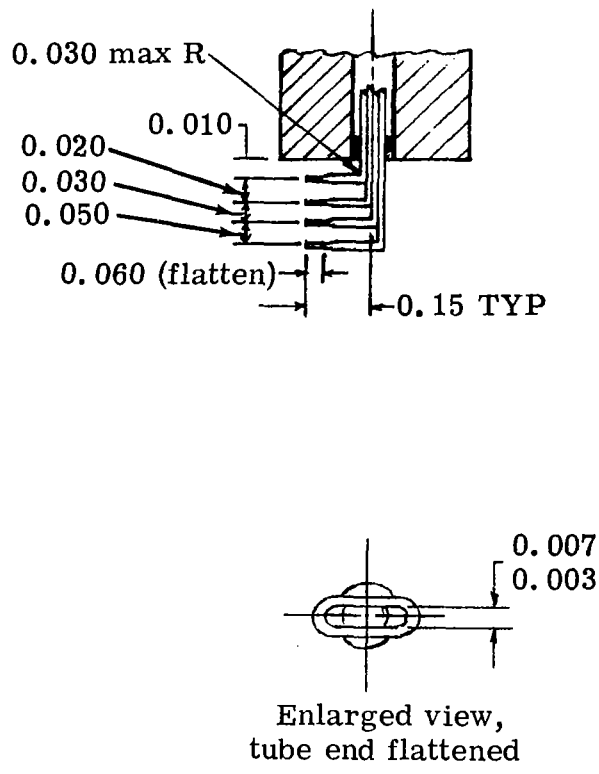

Figure 65. Boundary layer bleed total pressure rake design details.

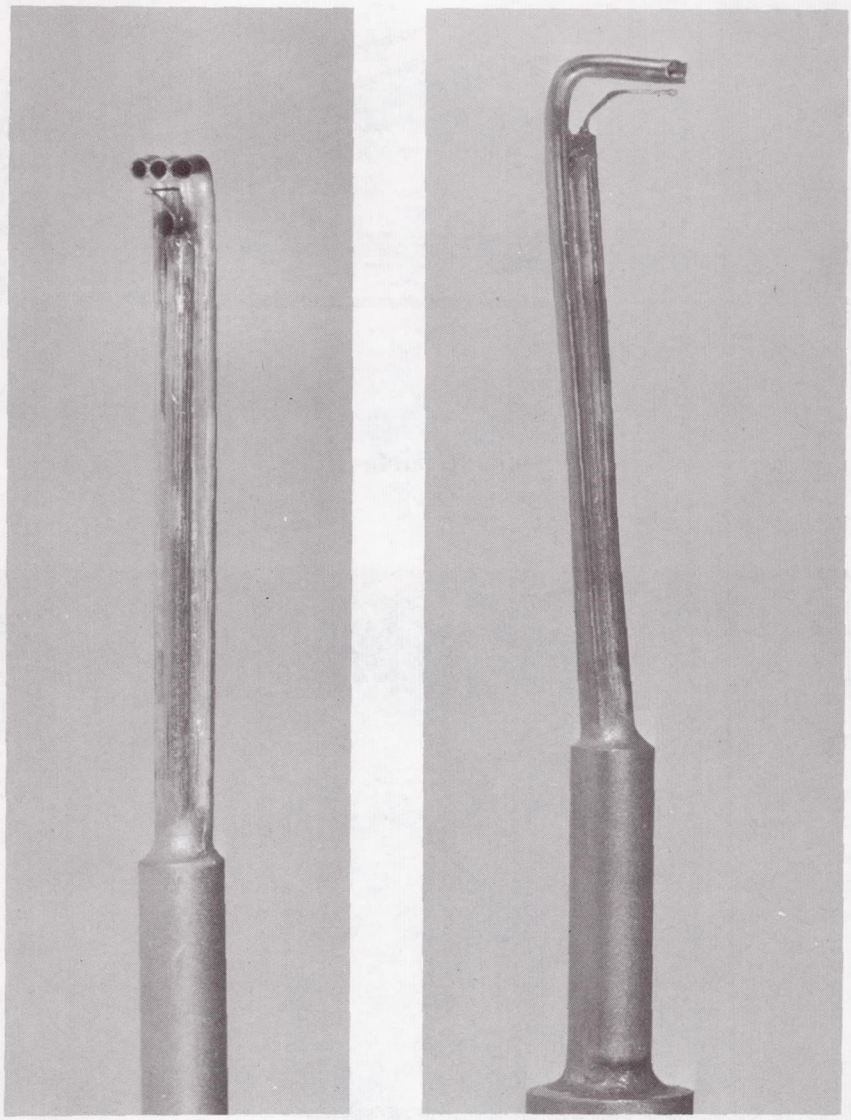

Figure 66. Inlet total pressure probe.

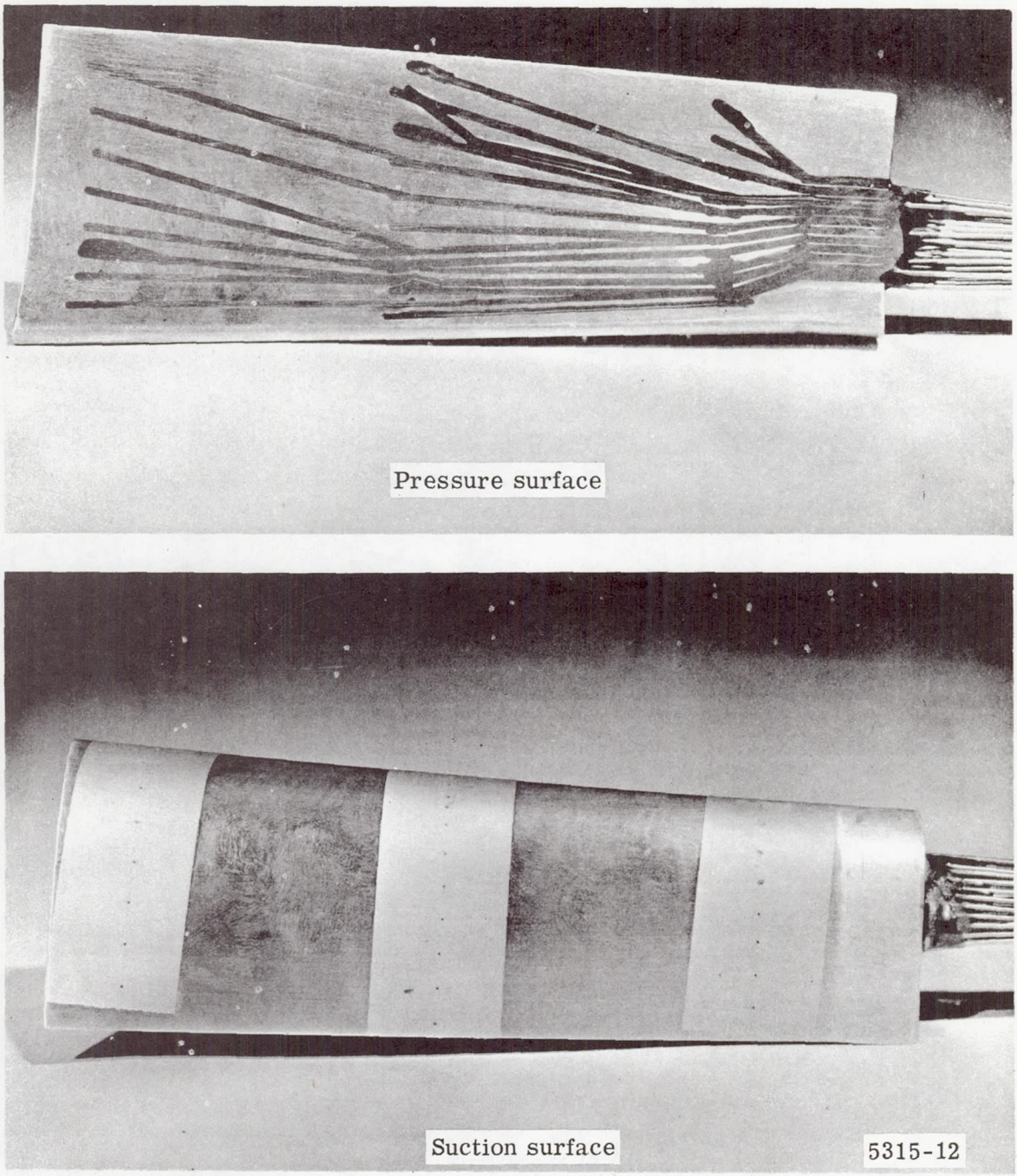

Figure 67. Instrumented plain blade.

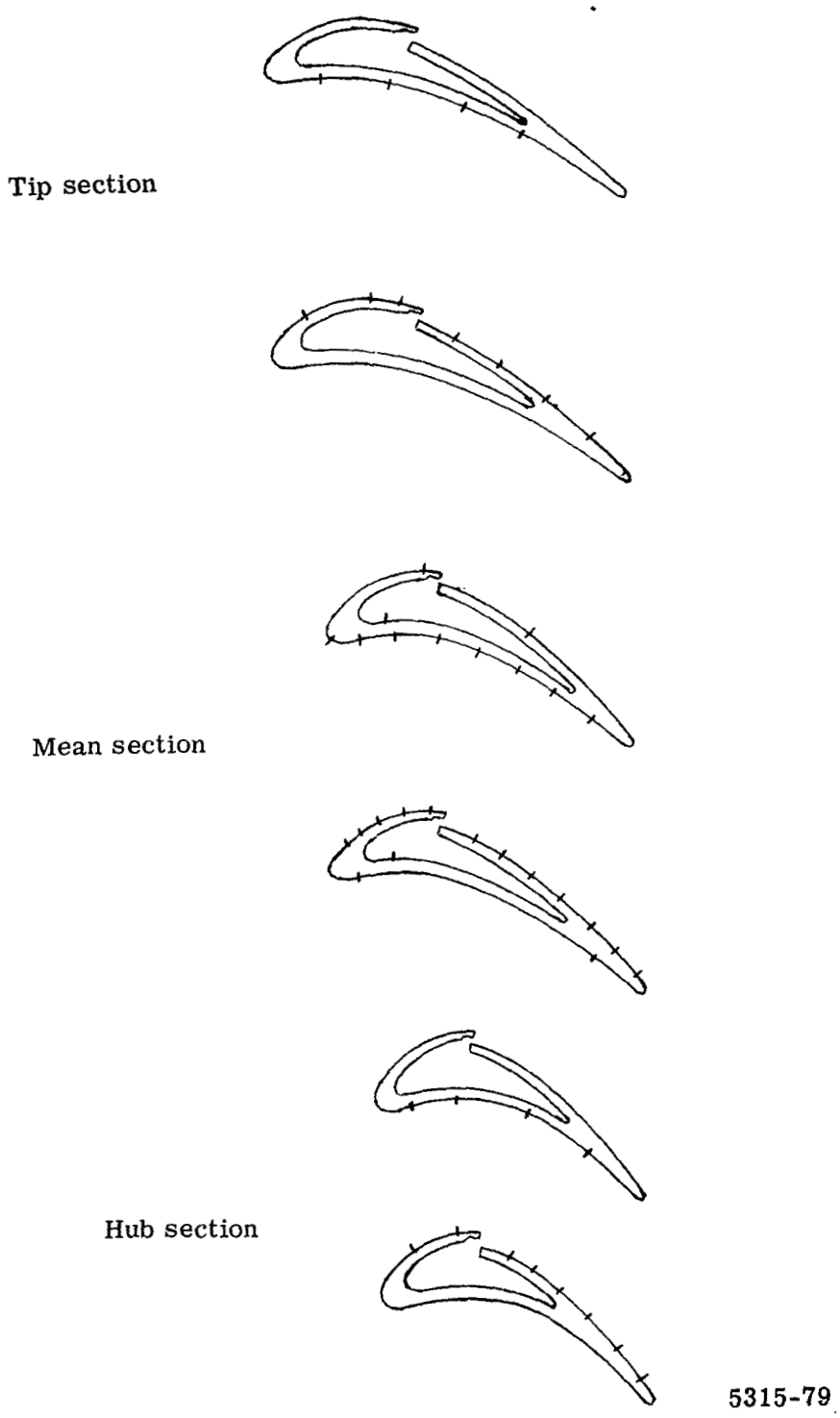

Figure 69. Tangential jet blowing slot location 1 blade static pressure tap distribution. See Table XXVI.

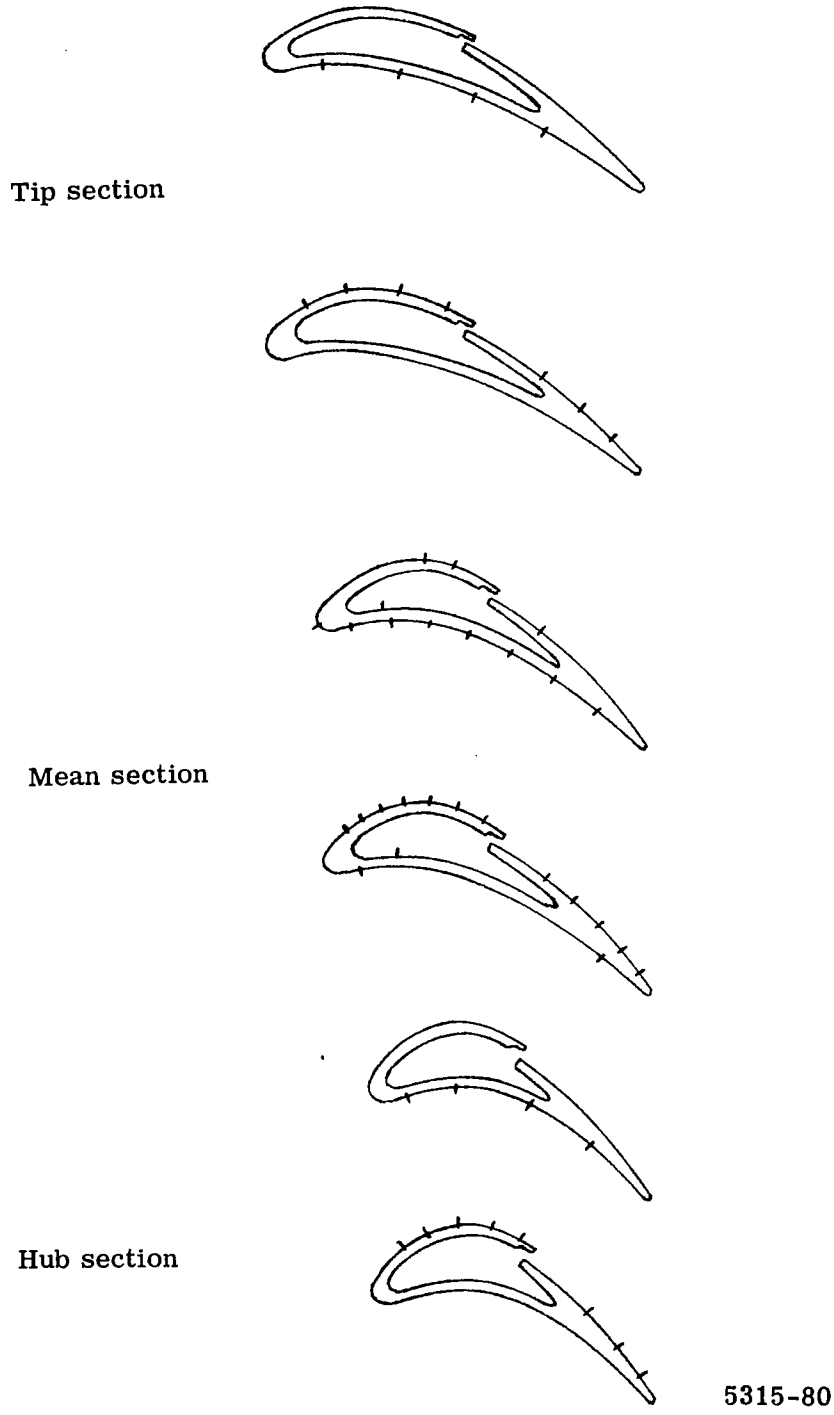

Figure 70. Tangential jet blowing slot location 2 blade static pressure tap distribution. See Table XXVII.

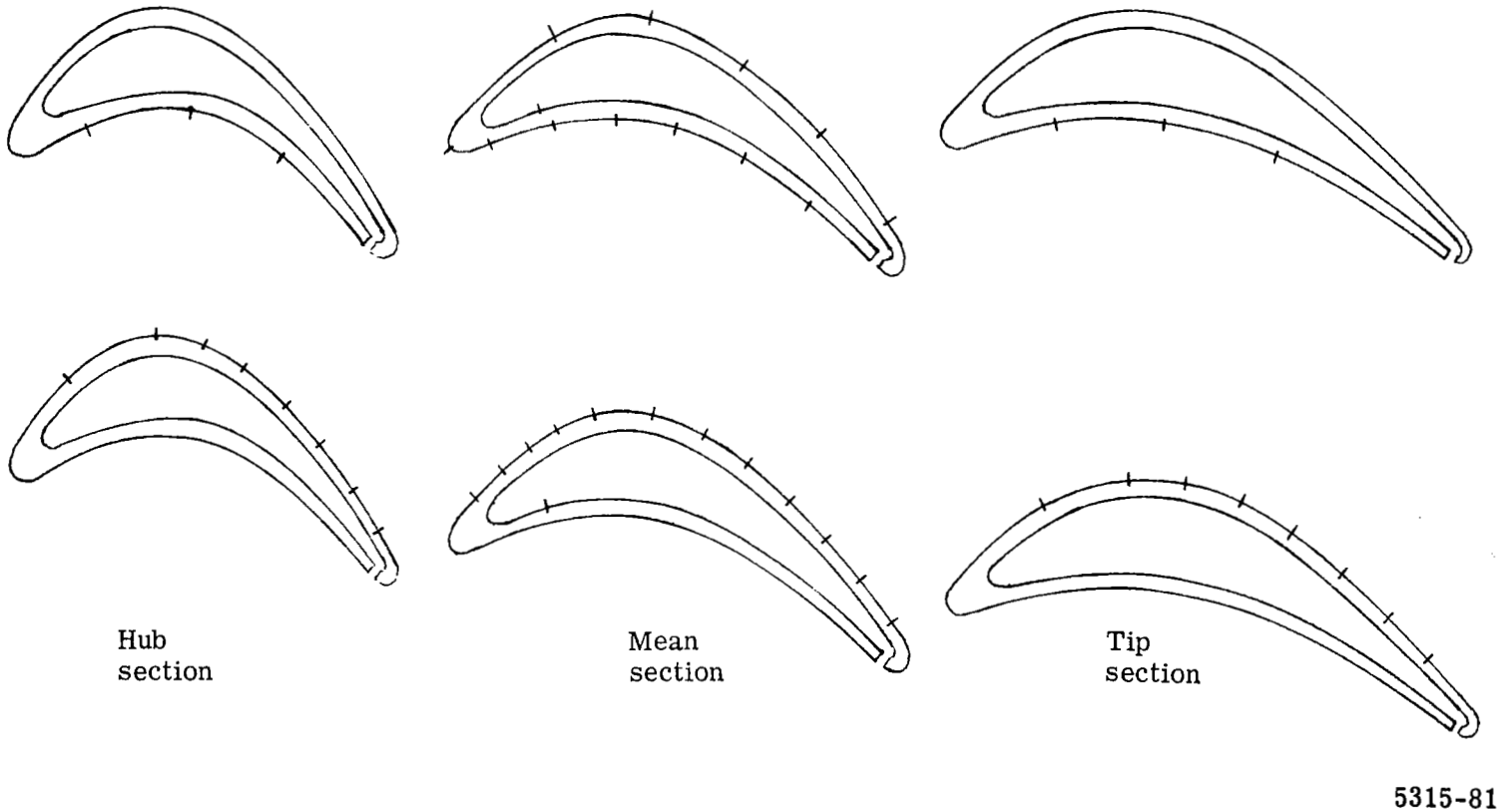

Figure 71. Jet-flapped blade static pressure tap distribution.
See Table XXVIII.

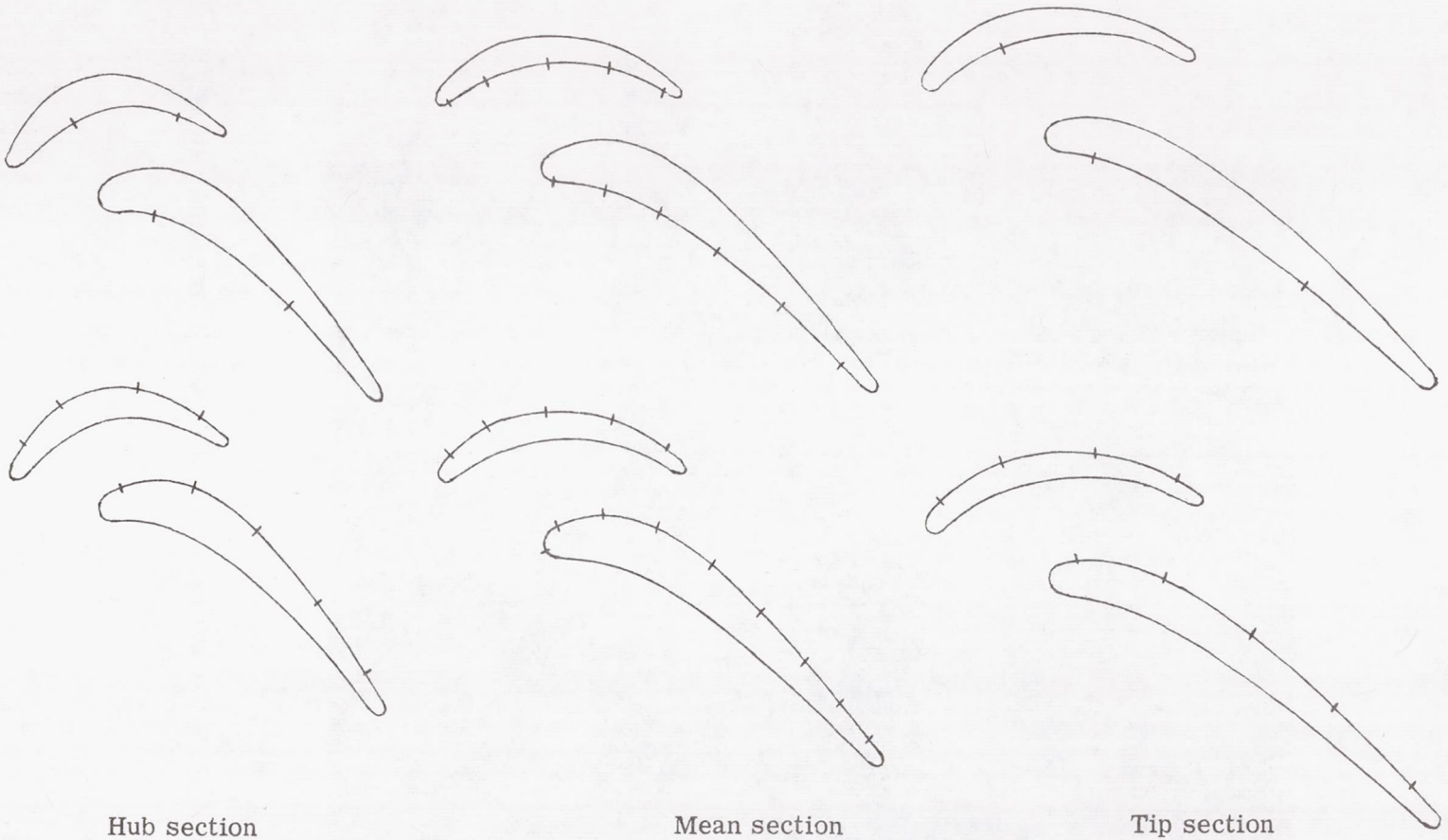

Figure 72. Tandem blade static pressure tap distribution.
See Table XXIX.

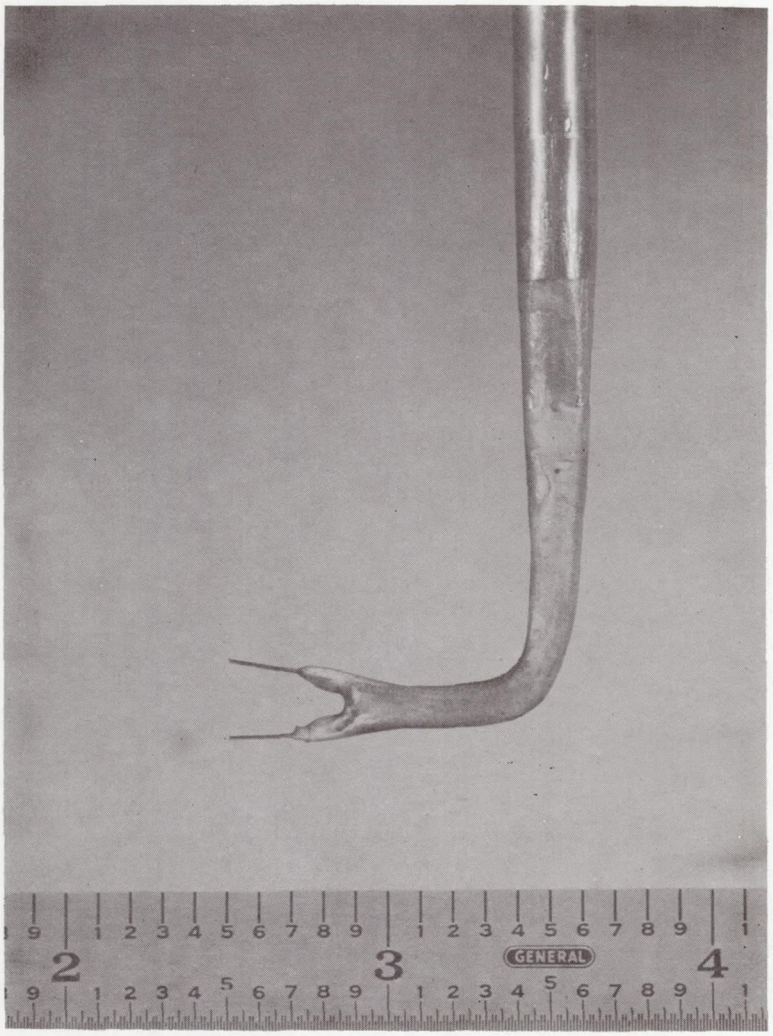

Figure 73. Exit wake survey bifurcated total pressure probe.

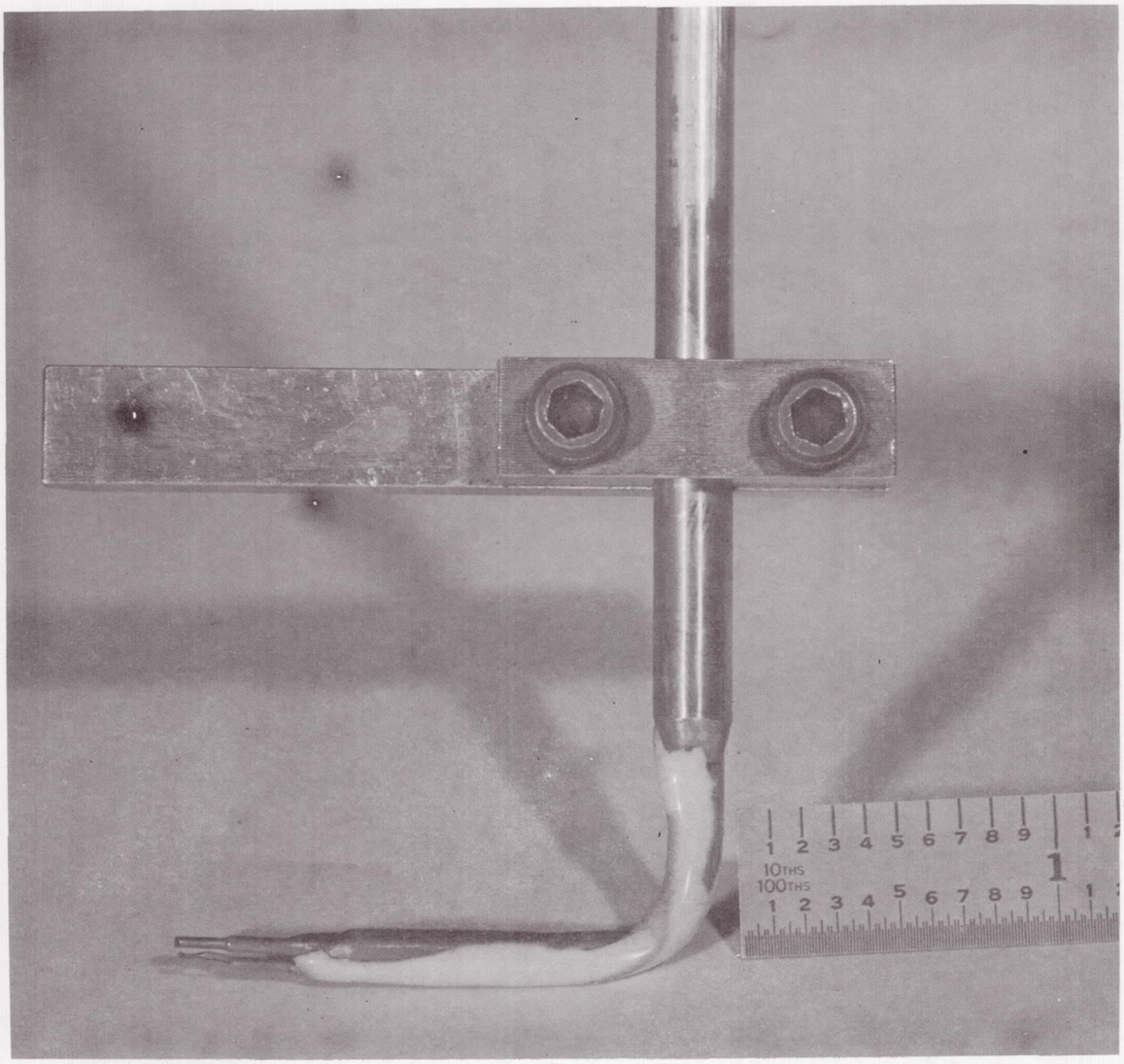

Figure 74. Downstream wake survey total temperature, total pressure, and gas flow angle prism probe.

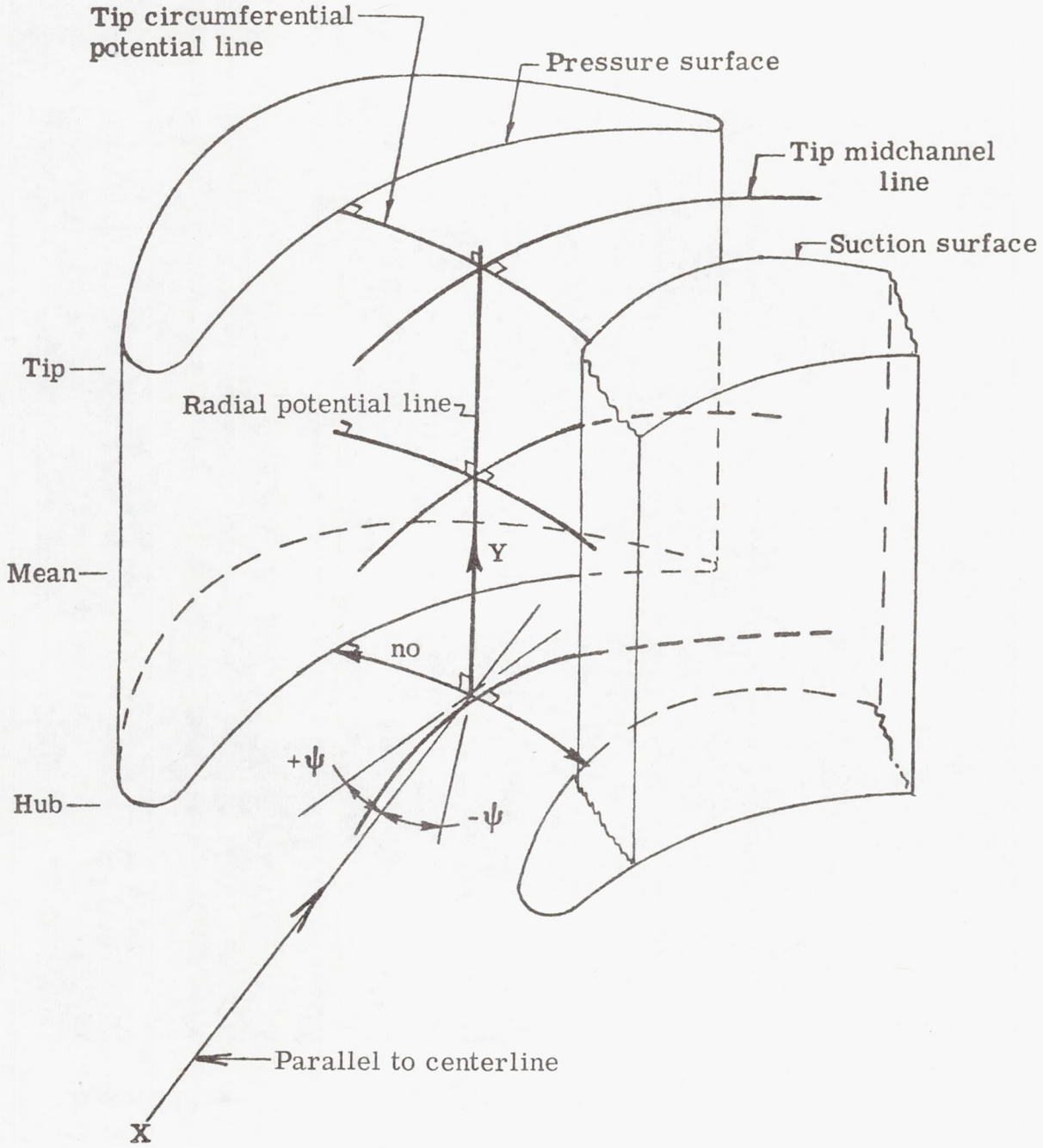

Figure 75. Schematic of flow analysis model.

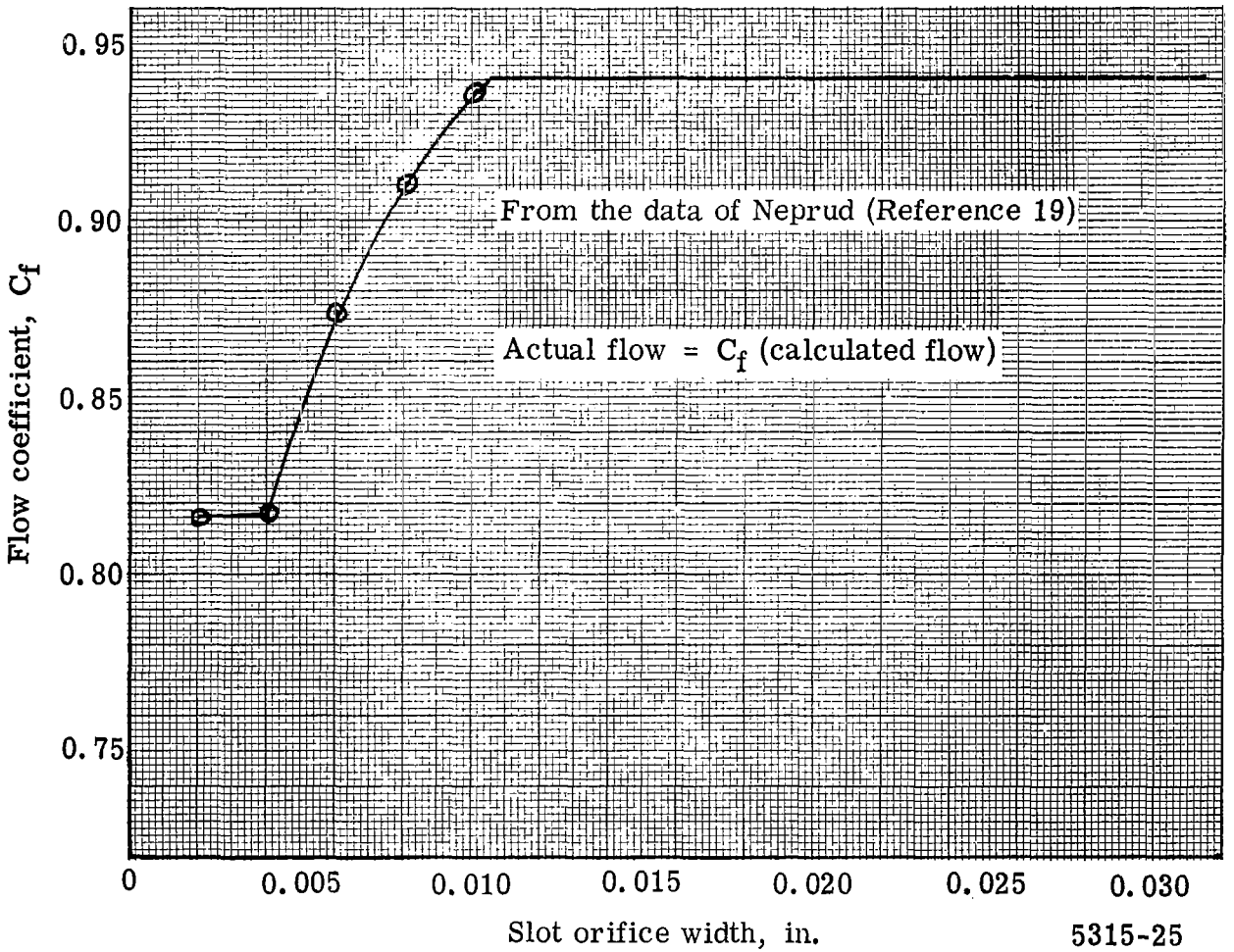

Figure 76. Flow coefficient versus slot width.

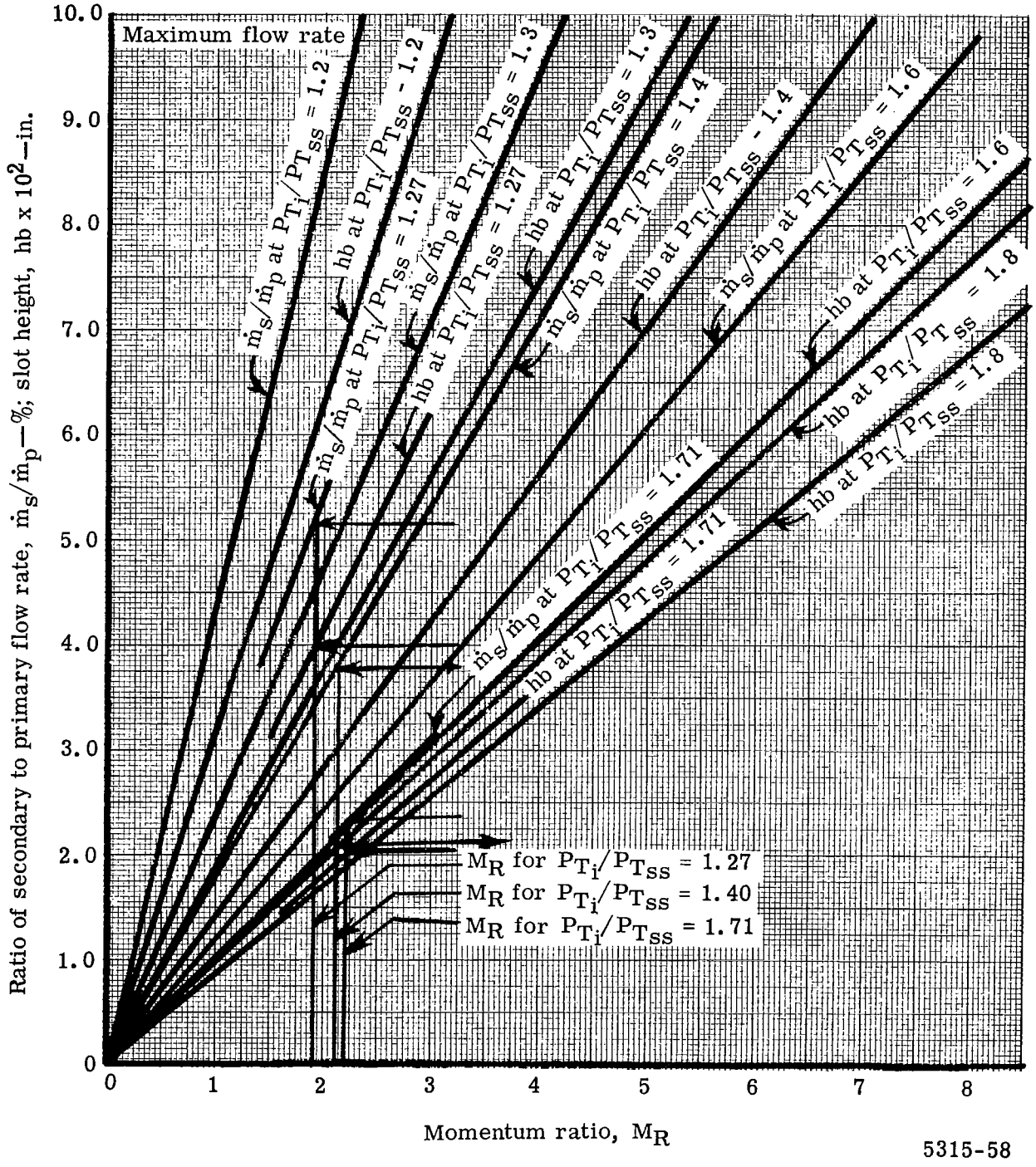

Figure 77. Working curves for tangential jet blade slot location 1 — hub section.

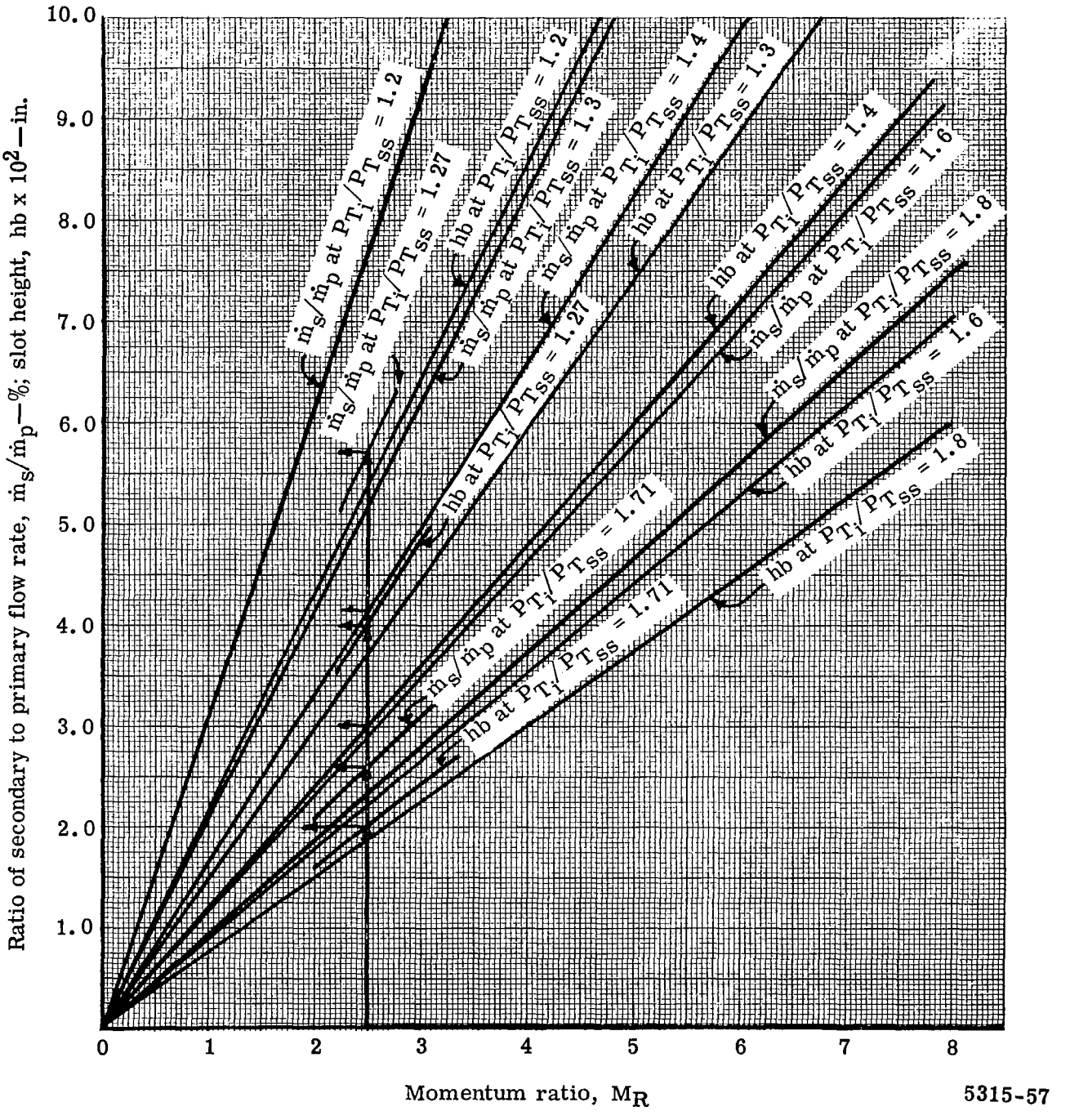

Figure 78. Working curves for tangential jet blade slot location 1 — mean section.

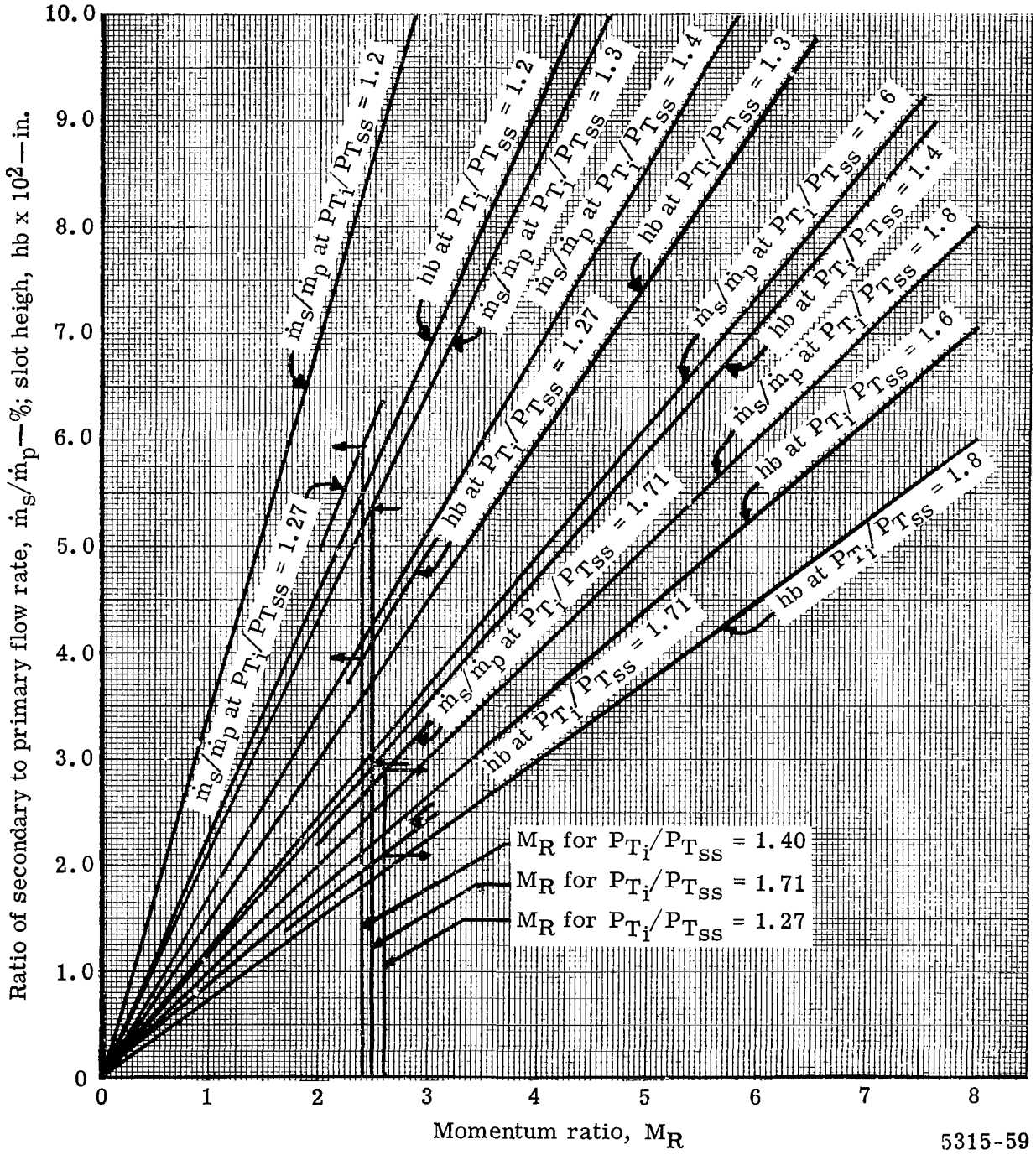

Figure 79. Working curves for tangential jet blade slot location 1 – tip section.

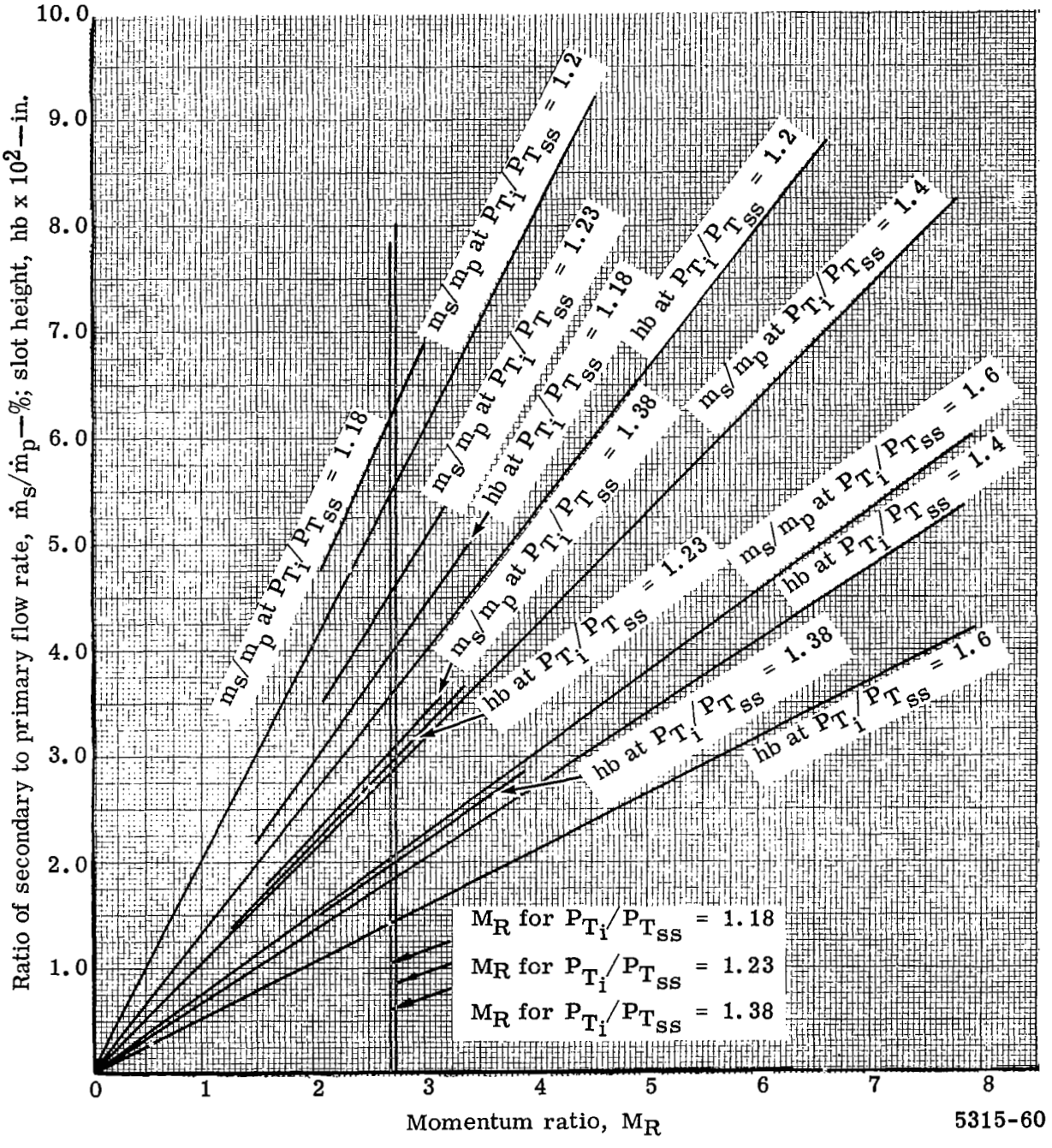

Figure 80. Working curves for tangential jet blade slot location 2 — hub section.

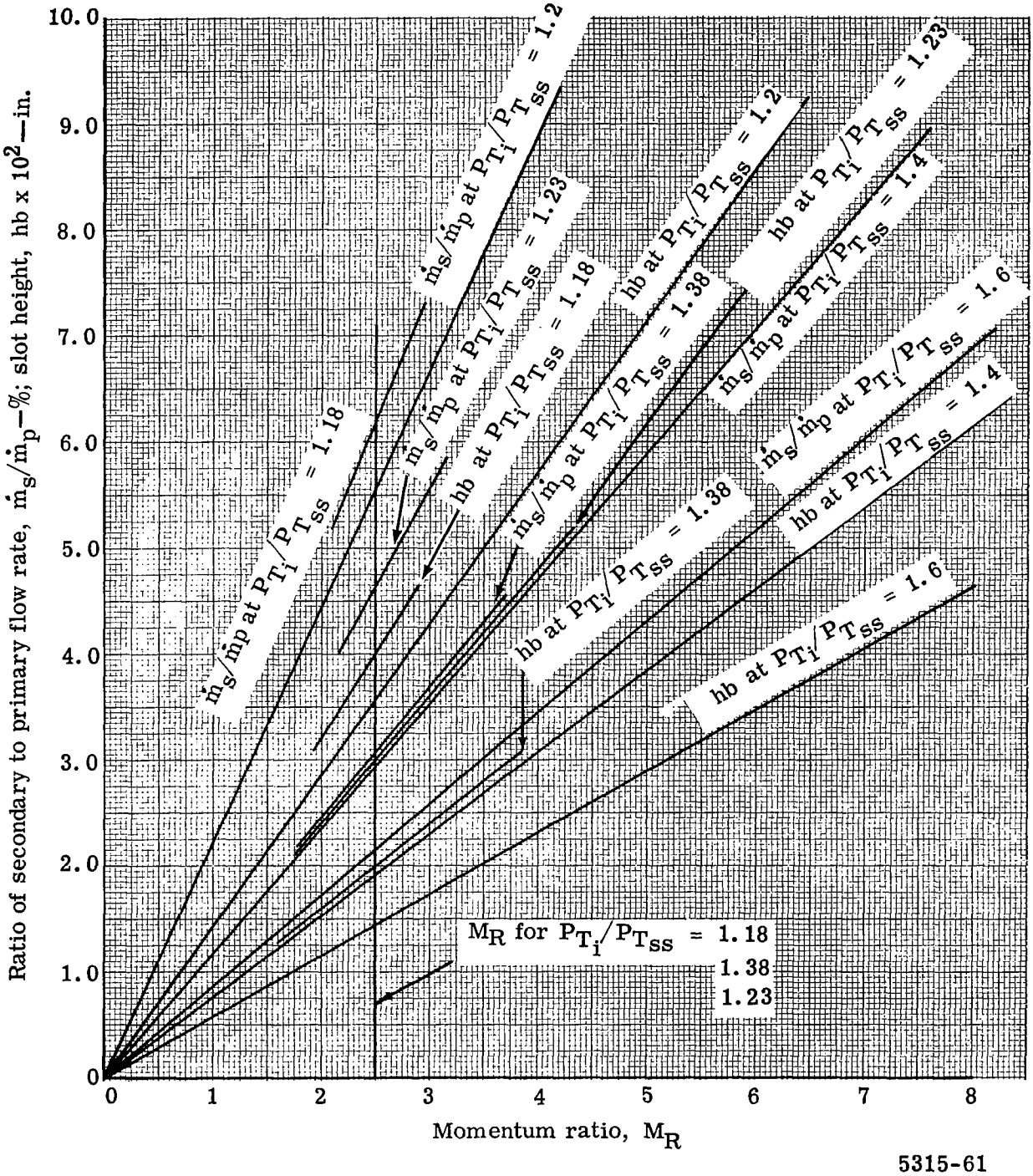

Figure 81. Working curves for tangential jet blade slot location 2 – mean section.

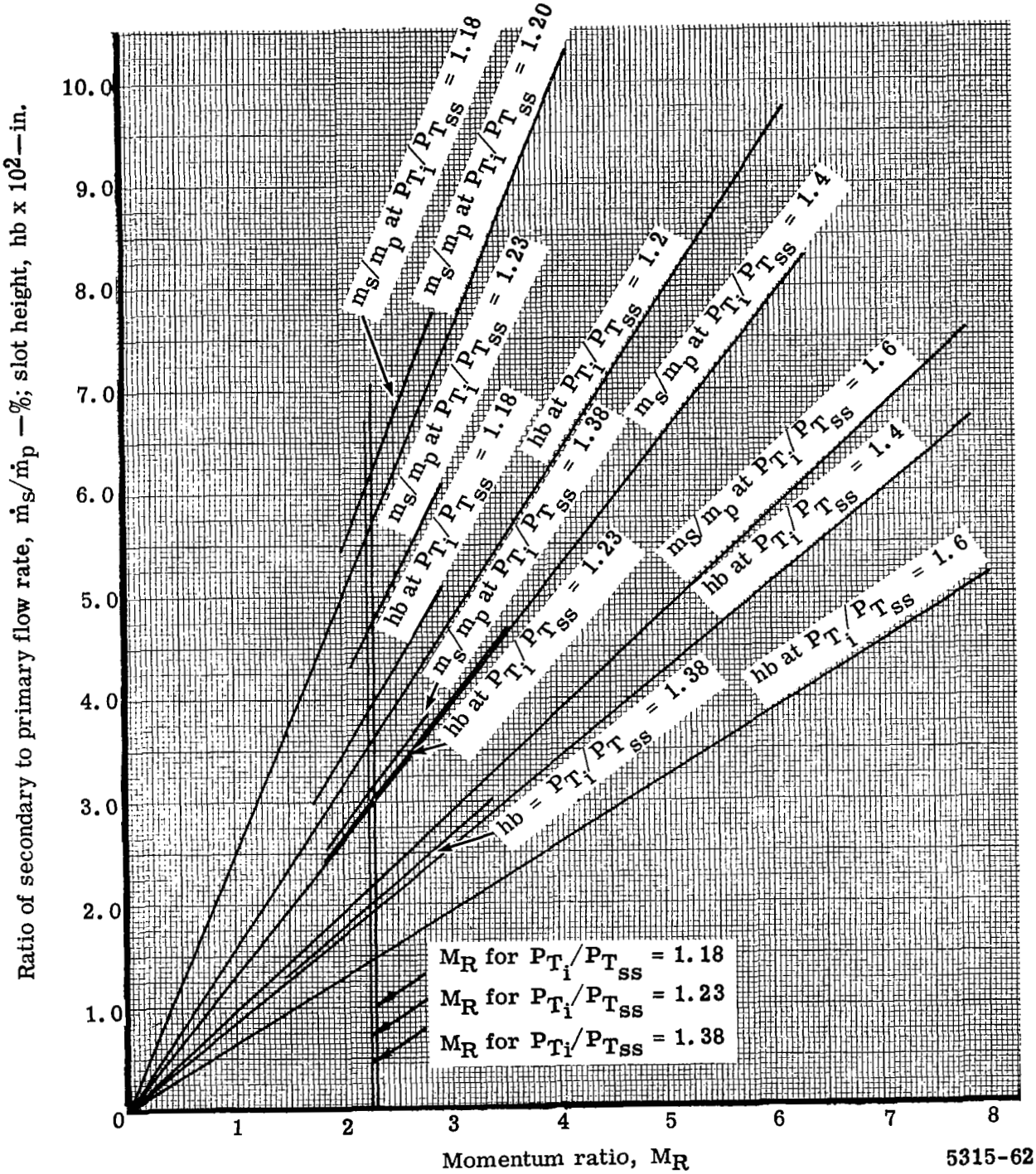

Figure 82. Working curves for tangential jet blade slot location 2 – tip section.

"The aeronautical and space activities of the United States shall be conducted so as to contribute . . . to the expansion of human knowledge of phenomena in the atmosphere and space. The Administration shall provide for the widest practicable and appropriate dissemination of information concerning its activities and the results thereof."

—NATIONAL AERONAUTICS AND SPACE ACT OF 1958

NASA SCIENTIFIC AND TECHNICAL PUBLICATIONS

TECHNICAL REPORTS: Scientific and technical information considered important, complete, and a lasting contribution to existing knowledge.

TECHNICAL NOTES: Information less broad in scope but nevertheless of importance as a contribution to existing knowledge.

TECHNICAL MEMORANDUMS: Information receiving limited distribution because of preliminary data, security classification, or other reasons.

CONTRACTOR REPORTS: Scientific and technical information generated under a NASA contract or grant and considered an important contribution to existing knowledge.

TECHNICAL TRANSLATIONS: Information published in a foreign language considered to merit NASA distribution in English.

SPECIAL PUBLICATIONS: Information derived from or of value to NASA activities. Publications include conference proceedings, monographs, data compilations, handbooks, sourcebooks, and special bibliographies.

TECHNOLOGY UTILIZATION PUBLICATIONS: Information on technology used by NASA that may be of particular interest in commercial and other non-aerospace applications. Publications include Tech Briefs, Technology Utilization Reports and Notes, and Technology Surveys.

Details on the availability of these publications may be obtained from:

SCIENTIFIC AND TECHNICAL INFORMATION DIVISION

NATIONAL AERONAUTICS AND SPACE ADMINISTRATION

Washington, D.C. 20546